

ISSN 1451 - 9372(Print)
ISSN 2217 - 7434(Online)
APRIL-JUNE 2022
Vol.28, Number 2, 95-167

Chemical Industry & Chemical Engineering Quarterly



The AChE Journal for Chemical Engineering,
Biochemical Engineering, Chemical Technology,
New Materials, Renewable Energy and Chemistry
www.ache.org.rs/ciceq



Journal of the
Association of Chemical Engineers of
Serbia, Belgrade, Serbia

**Chemical Industry &
Chemical Engineering
CI&CE Quarterly**

EDITOR-IN-CHIEF

Vlada B. Veljković

*Faculty of Technology, University of Niš, Leskovac, Serbia
E-mail: veljkovicvb@yahoo.com*

ASSOCIATE EDITORS

Jonjaua Ranogajec

*Faculty of Technology, University of
Novi Sad, Novi Sad, Serbia*

Srdan Pejanović

*Department of Chemical Engineering,
Faculty of Technology and Metallurgy,
University of Belgrade, Belgrade, Serbia*

Milan Jakšić

*ICEHT/FORTH, University of Patras,
Patras, Greece*

EDITORIAL BOARD (Serbia)

Dorđe Janačković, Sanja Podunavac-Kuzmanović, Viktor Nedović, Sandra Konstantinović, Ivanka Popović, Siniša Dodić, Zoran Todorović, Olivera Stamenković, Marija Tasić, Jelena Avramović, Goran Nikolić, Dunja Sokolović

ADVISORY BOARD (International)

Dragomir Bukur

Texas A&M University,

College Station, TX, USA

Milorad Dudukovic

*Washington University,
St. Luis, MO, USA*

Jiri Hanika

*Institute of Chemical Process Fundamentals, Academy of Sciences
of the Czech Republic, Prague, Czech Republic*

Maria Jose Cocero

*University of Valladolid,
Valladolid, Spain*

Tajalli Keshavarz

*University of Westminster,
London, UK*

Zeljko Knez

*University of Maribor,
Maribor, Slovenia*

Igor Lacik

*Polymer Institute of the Slovak Academy of Sciences,
Bratislava, Slovakia*

Denis Poncelet

ENITIAA, Nantes, France

Ljubisa Radovic

Pen State University,

PA, USA

Peter Raspor

*University of Ljubljana,
Ljubljana, Slovenia*

Constantinos Vayenas

*University of Patras,
Patras, Greece*

Xenophon Verykios

*University of Patras,
Patras, Greece*

Ronnie Willaert

*Vrije Universiteit,
Brussel, Belgium*

Gordana Vunjak Novakovic

*Columbia University,
New York, USA*

Dimitrios P. Tassios

*National Technical University of Athens,
Athens, Greece*

Hui Liu

China University of Geosciences, Wuhan, China

FORMER EDITOR (2005-2007)

Professor Dejan Skala

University of Belgrade, Faculty of Technology and Metallurgy, Belgrade, Serbia



Journal of the
Association of Chemical Engineers of
Serbia, Belgrade, Serbia

**Chemical Industry &
Chemical Engineering
CI&CE Quarterly**

Vol. 28

Belgrade, April-June 2022

No. 2

Chemical Industry & Chemical Engineering
Quarterly (ISSN 1451-9372) is published
quarterly by the Association of Chemical
Engineers of Serbia, Kneza Miloša 9/I,
11000 Belgrade, Serbia

Editor:
Vlada B. Veljković
veljkovic@yahoo.com

Editorial Office:
Kneza Miloša 9/I, 11000 Belgrade, Serbia
Phone/Fax: +381 (0)11 3240 018
E-mail: shi@yubc.net
www.ache.org.rs

For publisher:
Ivana T. Drvenica

Secretary of the Editorial Office:
Slavica Desnica

Marketing and advertising:
AChE Marketing Office
Kneza Miloša 9/I, 11000 Belgrade, Serbia
Phone/Fax: +381 (0)11 3240 018

Publication of this Journal is supported by the
Ministry of Education, Science and
Technological Development of the Republic of
Serbia

Subscription and advertisements make payable
to the account of the Association of Chemical
Engineers of Serbia, Belgrade, No. 205-2172-
71, Komercijalna banka a.d., Beograd

Computer typeface and paging:
Marija Tasić

Printed by:
Faculty of Technology and Metallurgy,
Research and Development Centre of Printing
Technology, Karnegijeva 4, P.O. Box 3503,
11120 Belgrade, Serbia

Abstracting/Indexing:
Articles published in this Journal are indexed in
Thompson Reuters products: *Science Citation
Index - Expanded™* - access via *Web of
Science®*, part of *ISI Web of Knowledge™*

CONTENTS

- Srinivasan Periasamy Manikandan, Nesakumar Dharmakkan,
Nagamani Sumana, **Heat transfer studies of Al₂O₃/water-
ethylene glycol nanofluid using factorial design analysis ...** 95
- Murugesan Manikkampatti Palanisamy, Kannan Kandasamy,
Venkata Ratnam Myneni, **Two phase leaching for metal
recovery from waste printed circuit boards: statistical
optimization** 103
- Florin Enachea, Dan Danulescu, Ion Bolocan, Diana Cursaru, **The
reduction of FCCU afterburning through process optimization
and regenerator revamping.....** 115
- Sreepriya Sreekumar, Aparna Kallingal, Vinila Mundakkal
Lakshmanan, **pH control in sodium chlorate cell for energy
efficiency using PSO-FOPID controller.....** 127
- Naveen Prasad B.S., Selvaraju Sivamani, Azucena Cuento,
Senthilkumar Pachiyappan, **Chemical route for synthesis of
citric acid from orange and grape juices** 135
- A. Abdallah El Hadj, M. Laidi, S. Hanini, **New method based on
neuro-fuzzy system and pso algorithm for estimating phase
equilibria properties.....** 141
- Begüm Tepe, Tolga Kağan Tepe, Ayten Ekinci, **Impact of air
temperature on drying characteristics and some bioactive
properties of kiwi fruit slices** 151
- Petar D. Janjatović, Olivera A. Erić Cekić, Dragan M. Rajnović,
Sebastian S. Baloš, Vencislav K. Grabulov, Leposava P.
Šidjanin, **Microstructure and fracture mode of unalloyed dual
phase austempered ductile iron** 161

Activities of the Association of Chemical Engineers of Serbia are supported by:

- Ministry of Education, Science and Technological Development, Republic of Serbia
- Hemofarm Koncern AD, Vršac, Serbia
- Faculty of Technology and Metallurgy, University of Belgrade, Belgrade, Serbia
- Faculty of Technology, University of Novi Sad, Novi Sad, Serbia
- Faculty of Technology, University of Niš, Leskovac, Serbia
- Institute of Chemistry, Technology and Metallurgy, University of Belgrade, Belgrade, Serbia

SRINIVASAN P. MANIKANDAN
NESAKUMAR DHARMAKKAN
NAGAMANI SUMANA

Department of Chemical Engineering,
Kongu Engineering College,
Erode-638 060,
India

SCIENTIFIC PAPER

UDC 66.021.4:62

HEAT TRANSFER STUDIES OF Al_2O_3 /WATER-ETHYLENE GLYCOL NANOFUID USING FACTORIAL DESIGN ANALYSIS

Article Highlights

- Al_2O_3 /ethylene glycol/water mixed nanofluid were prepared
- Natural convection heat transfer experiments were conducted based on MINITAB design matrix
- Heat transfer coefficient was analyzed by different plots as provided in MINITAB
- Model equation for calculating heat transfer coefficient was proposed based on the ANOVA results

Abstract

The experimental study of the heat transfer coefficient of nanofluid plays a significant role in improving the heat transfer rate of the heat exchanger. A natural convection apparatus was used to study heat transfer in the suspension of Al_2O_3 nanoparticles in a water-ethylene glycol mixture base fluid. The effects of the heat input, the nanoparticle volume fraction, and the base fluid concentration on the heat transfer coefficient were studied using a 2^3 full factorial design matrix (16 experimental runs) and the MINITAB Design software. The levels for the heat input, nanoparticle volume fraction, and base fluid concentration were 10 and 100 W, 0.1 and 1 vol.%, and 30 and 50 vol.%, respectively. The residual, contour, 3D surface plots, and Pareto chart were drawn from the experimental results. The observed heat transfer coefficient showed the highest enhancement with the high level of the nanoparticle volume fraction and a moderate enhancement with the high level of heat input, and a slight enhancement with the base fluid concentration.

Keywords: Al_2O_3 nanofluid, full factorial design, heat transfer, natural convection.

“Nanofluid” attracted many researchers because of its significant application in enhancing heat transfer fluid properties such as thermal, electrical, magnetic, optical, and mechanical. Choi [1] was the first to utilize the nano-sized solid particles in conventional heat transfer fluids and showed a significant enhancement in the thermal conductivity of nanofluid. Hence the thermal performance of heat exchanger systems could be increased with the addition of nanoparticles which will save energy and the environment [2-5]. Over the years, several studies focusing on heat transfer en-

hancements using nanoparticles have been published. For instance, Das *et al.* [6] measured the thermal conductivity of Al_2O_3 and CuO nanoparticle suspension in the ethylene glycol and water (EG/W) mixture using a transient hot-wire method. They observed the thermal conductivity enhancement of 20% for the 4 vol.% concentration of the prepared nanoparticles.

Wen and Ding [7] have prepared the Al_2O_3 nanoparticle suspended water nanofluid and studied the heat transfer behavior of a prepared nanofluid in the laminar flow under constant wall heat flux. Their results showed that the heat transfer coefficient increases particularly at the entrance region with the increase in the Reynolds number and the nanoparticle concentration. Their result revealed that the Brownian motion of the nanoparticles resulting in the decreased thermal boundary layer is the reason for the enhancement of thermal conductivity. Cesare Biserni *et al.* [8] prepared the alumina/water nanofluid and

Correspondence: S.P. Manikandan, Department of Chemical Engineering, Kongu Engineering College, Erode-638 060, India.
E-mail: sriperiasamy@gmail.com
Paper received: 25 January 2021
Paper revised: 12 May 2021
Paper accepted: 28 May 2021

<https://doi.org/10.2298/CICEQ210125021M>

studied the natural convection of nanofluid in heterogeneous heating of square cavity. The study proposed the correlation equation to relate the Nusselt and Rayleigh numbers.

Mohebbi *et al.* [9] studied the effect of the γ -Al₂O₃ nanoparticle addition in a water-based fluid on the natural convection heat transfer of the corrugated T shaped cavity. They have employed the Lattice Boltzmann method for their study. They have examined the impact of the nanoparticle Rayleigh number, solid volume fraction, and the aspect ratio of the grooves cavity on the streamlines and the averaged Nusselt number. They have obtained a positive impact on heat transfer performance by nanoparticle addition. Li and Peterson [10] studied the natural convection heat transfer of the nanofluid prepared by suspending Al₂O₃ nanoparticles (47 nm) in water. The experiments were conducted with different particle volume fractions ranging from 0.5 to 6 vol.%. They have reported the visualization results and the causes of the deterioration of the prepared nanofluid natural convective heat transfer. Pak and Cho [11] studied the hydrodynamic effect and heat transfer behavior of the Al₂O₃ and TiO₂ based nanofluid in a horizontal circular tube. They found that the Nusselt number for the fully developed turbulent flow enhanced significantly concerning the nanoparticle volume fraction and the Reynolds number. They have proposed a new correlation for the turbulent convective heat transfer in nanofluids. Maiga *et al.* [12] used the Al₂O₃/ethylene glycol, and Al₂O₃/water nanofluids were to investigate the turbulent and laminar flow effect of a nanofluid inside circular tubes. They found that the heat transfer enhancement was higher for the Al₂O₃/ethylene glycol nanofluid when compared to the Al₂O₃/water nanofluid. The experimental study performed for the Al₂O₃-water mixture by Nguyen *et al.* [13] showed the enhancement in the heat transfer coefficient by 40% at 6.8 vol.% of nanoparticles. Al₂O₃/water nanofluid was used by Pandey *et al.* [14] to investigate the heat transfer performance of the prepared nanofluid in a counter flow corrugated plate heat exchanger. They studied the impact of nanofluid and water as coolants on heat transfer, frictional losses, and exergy loss. It was noted that the heat transfer behavior improves with the decrease in the nanoparticle concentration for water-nanofluid systems.

Prasad *et al.* [15] studied the heat transfer effect and friction of Al₂O₃ nanoparticles dispersed in water in a U-tube heat exchanger. They determined the Nusselt number at various Reynolds numbers and different nanoparticle volume fractions. The study concludes that the maximum increment in the Nusselt number occurs with the maximum Reynolds number.

Huang *et al.* [16] used Al₂O₃ to study the effect of the Al₂O₃/water nanofluid on heat transfer and pressure drop characteristics in a chevron-type plate heat exchanger. The study showed that at a constant Reynolds number, the heat transfer enhancement in the nanofluid was better than that in the base fluid. The heat transfer enhancement may be due to the increase in thermal conductivity. Xie *et al.* [17] prepared a nanofluid with different metal oxide suspensions of nanoparticles (Al₂O₃, ZnO, SiO₂, MgO, and TiO₂) in ethylene glycol. The study focused on the thermal conductivity and heat transfer effects. According to their research, the MgO/EG nanofluid showed the highest heat transfer enhancement with 41% improvement in thermal conductivity compared with other suspensions at a volume concentration of 5%.

Satti *et al.* [18] studied thermal conductivity in the ZnO, Al₂O₃, CuO, and SiO₂ nanoparticle suspensions in a water and propylene glycol mixture base fluid. Their operating conditions were temperature ranging from 30 to 90°C and a nanoparticle concentration up to 6 vol.%. Their findings were the thermal conductivity proportionately increases with the nanoparticle concentration and the operating temperature. This result shows that the nanofluid could be utilized for higher temperature applications. Thermal conductivity and heat transfer behavior of graphene, TiO₂, and ZnO nanoparticles suspended in an ethylene glycol-water mixture was analyzed by Periasamy and Baskar [19-21]. Their analysis revealed that the thermal conductivity and the heat transfer coefficient were enhanced by increasing the nanoparticle volume fraction. Sahoo *et al.* [22] and Yu *et al.* [23] observed that as the nanoparticle loading of Al₂O₃ in the 40:60 (water: ethylene glycol) mixture by mass ratio increased, the viscosity of the nanofluid also increased. Huang *et al.* [24] studied the heat transfer characteristics experimentally using Al₂O₃ nanoparticles in a plate heat exchanger. They concluded that the heat transfer enhanced significantly at a constant Reynolds number than the base fluid without nanoparticles. The thermal conductivity enhancement is the reason for this heat transfer enhancement.

Based on the literature survey, several studies were found concerning the application of nanofluids in heat transfer for improving the efficiency of a heat exchanger. However, the full factorial design has rarely been used to analyze the influence of various input factors on the heat transfer characteristics of nanofluids. In this study, a natural convection heat transfer apparatus was used, whereas Al₂O₃ nanoparticles were suspended in a base fluid mixture of water-ethylene glycol. The effects of input factors such as the heat input, the nanoparticle volume fraction

and the base fluid concentration on the experimental heat transfer coefficient ($h_{exp,nf}$) were analyzed using the residual plot, Pareto chart, contour plot, and 3D surface plot.

MATERIALS AND METHODS

Experimental procedure

The experiment was conducted in a natural convection experimental setup. The schematic layout and photography of the experimental setup are shown in Figure 1. The experimental setup consists of a vertical stainless steel (SS) tube enclosed in a duct. The diameter and length of the tube are 0.045 m and 0.5 m, respectively. The front side of the rectangular duct is made of a transparent section to facilitate visual observation. The heating was conducted by an electrical heating element embedded in a copper tube. The thermocouples were inserted along the tube to measure the surface temperature at various heights. The tube surface was polished to minimize radiation loss. An ammeter and voltmeter were used for determining the wattage dissipated by the heat source.

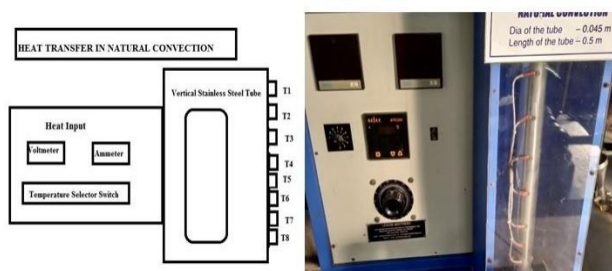


Figure 1. Schematic layout and photography of the experimental set up.

The input factors were employed in the experiment as per the design matrix. After the steady-state attainment, the temperatures T_1 to T_8 were noted down. In addition, the ambient temperature was recorded. The experiment was repeated for different input factors based on the MINITAB DOE results. The convective heat transfer coefficient was calculated by the following formulae.

$$h_{exp,nf} = \frac{Q}{A(T_s - T_a)}$$

where T_s is the surface temperature calculated as the average temperature between T_2 and T_7 , T_a is ambient temperature calculated as the average temperature between T_1 and T_8 , and A is the tube surface.

Factorial design and analysis

Input parameters and their levels

The experiments were conducted at all combinations of the factor levels, as provided by the

design software, and the output response (heat transfer coefficient) was determined. Each experimental operating condition was a "Run", the output response was an "Observation," and the entire set of runs was the "Design." [25-27]. A two-level full factorial design was employed with two replications, which provides 16 experimental combinations. Table 1 provides the design summary and factor and level for the full factorial design applied in the present study.

Table 1. Design summary: factor and level for the full factorial design

Factors	Level		
Base design			
Number of experimental runs			
Replicates			
Blocks			
Input Factors	Code	Low	High
Heat Input, W	A	10	100
Nanoparticle volume fraction, vol. %	B	0.1	1.0
Base fluid volume fraction, vol. %	C	30	50

Statistical analysis was applied to investigate the significance of the input factors and their interactions on the output response. Table 2 exhibits the experimental results of the 2^3 full factorial design.

Stepwise regression model for elimination of insignificant factors

The stepwise regression method was used in MINITAB to eliminate the nonsignificant factors. Minitab added or removed a term in the stepwise analysis in each step. In addition, a mixed selection approach, i.e., a combination of the forward and backward selection of variables, is used. The results of the stepwise regression model were tabulated and shown in Table 3. Since the values of R^2 and R^2_{adj} were close to each other, the model did not include insignificant parameters [28]. The developed regression equation in its coded form is provided below.

$$h_{nf} = 0.258A + 43.6B + 1.24C - 15.2$$

RESULTS AND DISCUSSION

Residual plots for the heat transfer coefficient of Al₂O₃/EG/W nanofluids

In statistics, a residual plot is used for finding the fitness of data for the performed experimental results. A residual plot is drawn by taking the independent variable on the horizontal axis and the residual values on the vertical. Figure 2 presents the residuals versus

Table 2. Experimental results of 2³ full factorial design

Standard order	Run order	Factorial input variable			Response variable, $h_{exp,nf}$, (W/m ² K)
		A Heat Input, Q (W)	B Nanoparticle volume fraction (vol.%)	C Base fluid volume fraction (vol.%)	
1	4	100	1.0	50	114
2	1	10	0.1	30	28
3	3	10	1.0	50	102
4	5	10	0.1	30	31
5	7	10	1.0	50	92
6	6	100	0.1	30	42
7	8	100	1.0	50	108
8	2	100	0.1	30	48
9	15	10	1.0	50	87
10	14	100	0.1	30	65
11	12	100	1.0	50	118
12	9	10	0.1	30	30
13	11	10	1.0	50	82
14	10	100	0.1	30	38
15	16	100	1.0	50	106
16	13	10	0.1	30	33

Table 3. Factorial fit and stepwise regression results for h , nf versus A, B, C

Term	Coef	SE Coef	T	P
Constant	-15.13	11.28	-1.35	0.203
A	0.25833	0.05609	4.61	0.001
B	43.611	5.609	7.78	0.000
C	1.2375	0.2524	4.90	0.000
S	10.096			
R-Sq	89.8%			
R-Sq(adj)	87.3%			

Source	DF	Seq SS	MS	F	P
Regression	3	10774.7	3591.6	35.23	0.000
Residual error	12	1223.3		101.9	
Pure error	8	31.5			
Total	15	11998			

the fitted values, histogram, and the residuals versus the order of the data for the convective heat transfer coefficient. Based on the present study, most of the data are linearly associated, and hence the model is best fitted with the obtained data. The residual plot also shows the interaction between the input factors and the output response. All these residual plots clearly show the fitness of the present research data. A good fit within the limit is also observed, indicating no unexpected errors in the developed model [29].

Pareto chart for the heat transfer coefficient of Al₂O₃/EG/W nanofluids

Pareto chart is very useful in identifying the significant factors and their interactions on the response factor for the given experimental results [30].

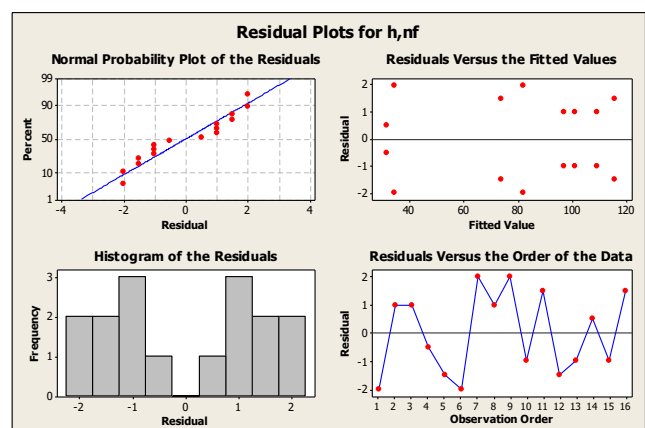


Figure 2. Residual plots for heat transfer coefficient of nanofluids.

The Pareto chart is plotted with the response factor of the convective heat transfer coefficient to segregate the crucial factors from insignificant factors. Figure 3 shows the Pareto chart of the standardized effects on the heat transfer coefficient of nanofluids. In this Figure, the bars represent factors *B* (nanoparticle volume fraction), *A* (heat input), *AB* (interaction of *A* and *B*), and *C* (base fluid volume fraction) cross the reference line (i.e., 2.31). These factors are statistically significant at the 0.05 level with the current model terms.

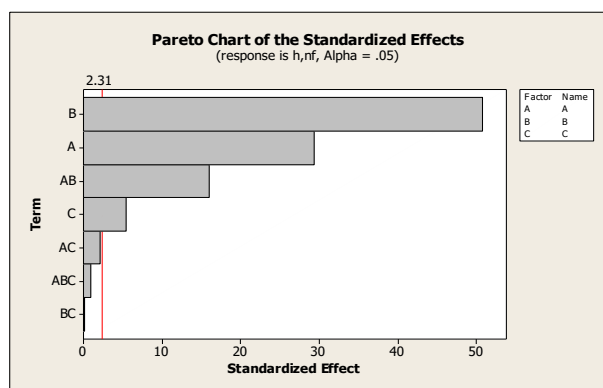


Figure 3. Pareto chart of the standardized effects on heat transfer coefficient of Nanofluids.

Contour plot for heat transfer coefficient of Al₂O₃/EG/W nanofluids

The effects of the process variables, such as the heat input, nanoparticle volume fraction, and base fluid concentration, are optimized by the full factorial design. A three-dimensional contour plot was drawn from the developed model, as shown in Figures 4(a) and (b). Figure 4(a) depicts the contour plot for the heat transfer coefficient concerning the input factors *A* and *C*. A contour plot shows a 2-dimensional view in which all points with the same response are linked to produce contour lines. Contour plots help investigate the effect on the desired response for the operating conditions. It was observed from figure 4(a) that the heat transfer coefficient (output response) varies between the ranges from 45 W/(m²K) to 105 W/(m²K) based on the variations on both *A* (heat input) and *C* (base fluid volume fraction). With increasing the heat input and the base fluid concentration, the heat transfer coefficient increases significantly, which shows that the heat input and the base fluid concentration favor the heat transfer enhancement.

Figure 4(b) provides the contour plot for the heat transfer coefficient for the input factors *A* and *B*. The heat transfer coefficient increases gradually for the heat input and the nanoparticle volume fraction. The maximum enhancement of 105 W/(m²K) was

observed at the heat input of 100 W and the nanoparticle volume fraction of 1.0 vol.%. This result shows that the nanoparticle addition significantly enhances the heat transfer characteristics of the base fluid used in industries.

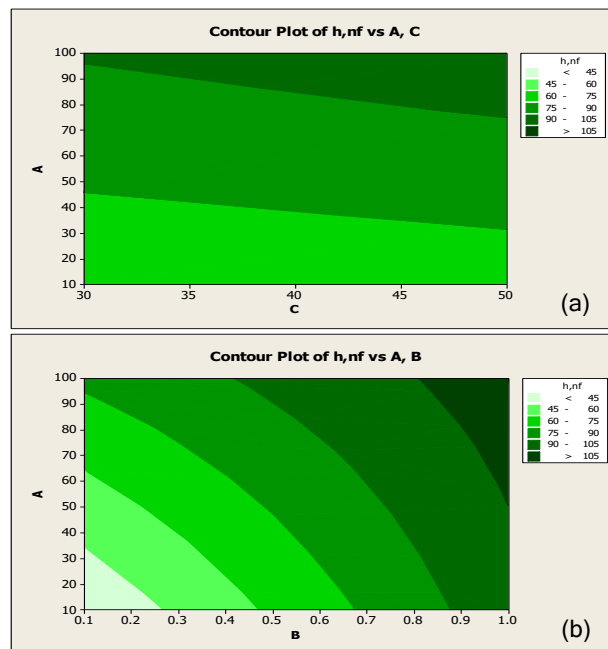


Figure 4. Contour plot for heat transfer coefficient of nanofluids.

3D surface plot for the heat transfer coefficient of Al₂O₃/EG/W nanofluids

The surface plot for the heat transfer coefficient concerning input factors *B* and *A* is shown in Figure 5. The heat transfer coefficient increases gradually for the nanoparticle volume fraction and the heat input. The maximum thermal conductivity enhancement was observed at a nanoparticle fraction of 1.0 vol.% and heat input of 100 W.

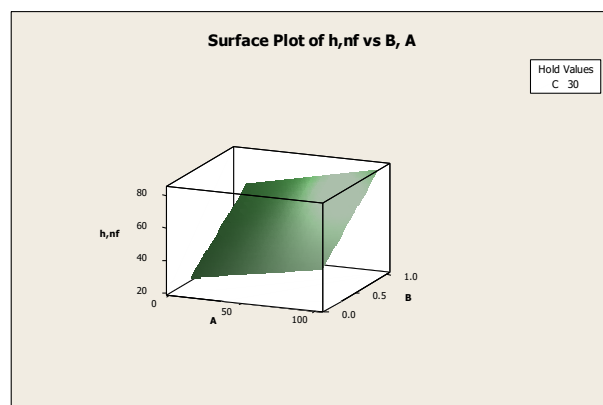


Figure 5. 3D surface plot for heat transfer coefficient of nanofluids.

An experiment was performed at the optimum conditions to validate the developed equation. As a result, a good agreement between the experimental

values and the values calculated by the developed equation was observed. Furthermore, it was also noticed that the heat transfer coefficient variations fall within $\pm 5\%$ deviation, which shows the accuracy of the developed equation.

CONCLUSION

The effect on the heat transfer coefficient of the Al₂O₃ nanoparticle suspended ethylene glycol/water base fluid was analyzed using the 2³ full factorial design matrix and the MINITAB design software. The influence of the heat input (*A*), nanoparticle volume fraction (*B*), and base fluid volume fraction (*C*) was studied in a natural convection heat transfer apparatus. The obtained results were analyzed by plotting residual, contour, 3D surface plots, and the Pareto chart. Based on the residual plot, most of the data are linearly fitted, and hence the model is best fitted for the present study. The maximum heat transfer coefficient of 125 W/(m²K) was observed corresponding to the heat input of 100 W, the nanoparticle fraction of 1.0 vol.%, and the 50 vol.% base fluid concentration. It may be concluded from the results of the contour and surface plots that the heat transfer coefficient increases gradually by increasing the heat input, nanoparticle concentration, and base fluid concentration.

Acknowledgment

The authors thank the management of Kongu Engineering College for the contribution of the SEED Grand and the Department of Chemical Engineering for the facility provided.

REFERENCES

- [1] S.U.S. Choi, S. Lee, S. Li, J.A. Eastman, *J. Heat Transfer* 121 (1999) 280-289.
- [2] I.M. Shahrul, I.M. Mahbubul, R. Saidur, S.S. Khaleduzzaman, M.F.M. Sabri, M.M. Rahman, *Numer. Heat Transfer Part A: Appl.* 65 (2014) 699-713.
- [3] I.M. Shahrul, I.M. Mahbubul, R. Saidur, M.F.M. Sabri, S.S. Khaleduzzaman, *J. Chem. Eng. Jpn.* 47 (2014) 340-344.
- [4] I.M. Shahrul, I.M. Mahbubul, R. Saidur, M.F.M. Sabri, M.A. Amalina, S.S. Khaleduzzaman, *Adv. Mater. Res.* 832 (2014) 154-159.
- [5] C.Y. Lin, J.C. Wang, T.C. Chen, *Appl. Energy* 88 (2011) 4527-4533.
- [6] S.K. Das, N. Putra, P. Thiesen, W. Roetzel, *J. Heat Transfer* 125 (2003) 567-574.
- [7] D. Wen, Y. Ding, *Int. J. Heat Mass Transfer* 47 (2004) 5181-5188.
- [8] I. Rashidi, O. Mahian, G. Lorenzini, C. Biserni, S. Wongwises, *Int. J. Heat Mass Transfer* 74 (2014) 391-402.
- [9] R. Mohebbi, S. H. Khalilabad, Y. Ma, *J. Appl. Fluid Mech.* 12 (2019) 1151-1160.
- [10] H.C. Li, G.P. Peterson, *Adv. Mech. Eng.* 2 (2010) 1-10.
- [11] B.C. Pak, Y. Cho, *Exp. Heat Transfer* 11 (1998) 151-170.
- [12] S.E.B. Maiga, C.T. Nguyen, N. Galanis, G. Roy, *Superlattices Microstruct.* 35 (2004) 543-557.
- [13] C.T. Nguyen, G. Roy, C. Gauthier, N. Galanis, *Appl. Therm. Eng.* 27 (2007) 1501-1506.
- [14] S.D. Pandey, V.K. Nema, *Exp. Therm. Fluid Sci.* 38 (2012) 248-256.
- [15] P.V. Durga Prasad, S. Gupta, M. Sreeramulu, L.S. Sundar, M.K. Singh, A.C.M. Sousa, *Exp. Therm. Fluid Sci.* 62 (2015) 141-150.
- [16] D. Huang, Z. Wu, B. Sunden, *Int. J. Heat Mass Transfer* 89 (2015) 620-626.
- [17] H. Xie, W. Yu, W. Chen, *J. Exp. Nanosci.* 5 (2010) 463-472.
- [18] J.R. Satti, D.K. Das, D. Ray, *Int. J. Heat Mass Transfer* 107 (2017) 871-881.
- [19] S.P. Manikandan, R. Baskar, *Chem. Ind. Chem. Eng. Q.* 24 (2018) 309-318.
- [20] S.P. Manikandan, R. Baskar, *Chem. Ind. Chem. Eng. Q.* 27 (2021) 15-20.
- [21] S.P. Manikandan, R. Baskar, *Chem. Ind. Chem. Eng. Q.* 27 (2021) 177-187.
- [22] B.C. Sahoo, R.S. Vajjha, R. Ganguli, G.A. Chukwu, D.K. Das, *Pet. Sci. Technol.* 27 (2009) 1757-1770.
- [23] W. Yu, H. Xie, Y. Li, L. Chen, Q. Wang, *Powder Technol.* 230 (2012) 14-19.
- [24] D. Huang, Z. Wu, B. Sunden, *Exp. Therm. Fluid Sci.* 72 (2016) 190-196.
- [25] R. V. Lenth, *Technometrics* 31 (1989) 469-473.
- [26] R. L. Plackett, J. P. Burman, *Biometrika* 33 (1946) 305-325.
- [27] H. Rostamian, M. N. Lotfollahi, *Period. Polytech. Chem. Eng.* 60 (2016) 93-97.
- [28] B.L. Dehkordi, A. Ghadimi, S.C. Henk, *Metselaar, J. Nanopart. Res.* 15 (2013) 1-9.
- [29] S.P. Manikandan, R. Baskar, *Period. Polytech. Chem. Eng.* 62 (2018) 317-322.
- [30] M. Khajeh, *Food Chem.* 129 (2011) 1832- 1838.

SRINIVASAN P. MANIKANDAN
NESAKUMAR DHARMAKKAN
NAGAMANI SUMANA

Department of Chemical Engineering,
Kongu Engineering College,
Erode-638 060,
India

NAUČNI RAD

ISTRAŽIVANJE PRENOSA TOPLOTE U NANOFLUIDU Al_2O_3 /VODA-ETILEN GLIKOL KORIŠĆENJEM FAKTORIJALNOG DIZAJNA

Eksperimentalno proučavanje koeficijenta prenosa toplote u nanofluidima igra značajnu ulogu u poboljšanju brzine prenosa toplote izmenjivača toplote. Aparatura za prirodnu konvekciju je korišćena za proučavanje prenosa toplote u suspenziji nanočestica Al_2O_3 u mešavini voda-etilen glikol kao osnovnog fluida. Efekti unosa toplote, zapreminskog udela nanočestica i koncentracije osnovnog fluida na koeficijent prenosa toplote proučavani su korišćenjem 2^3 punog faktorijalnog plana (16 eksperimenata) i softvera MINITAB Design. Nivoi za unos toplote, zapreminski udeo nanočestica i koncentracija osnovnog fluida bili su 10 W i 100 W, 0,1% i 1% v/v i 30% and 50% v/v, redom. Na osnovu eksperimentalnih podataka, nacrtani su rezidualni, konturni i 3D površinski grafici, kao i Pareto grafikon. Najveće poboljšanje koeficijenta prenosa toplote postignuto je pri visokom nivou zapreminskog udela nanočestica, umereno poboljšanje sa visokim nivoom toplotnog unosa, a blago poboljšanje sa koncentracijom baznog fluida.

Ključne reči: Al_2O_3 nanofluid, puni faktorijalni plan, prenos toplote, prirodna konvekcija.

MURUGESAN M.
PALANISAMY¹
KANNAN KANDASAMY²
VENKATA R. MYNENI³

¹ Department of Food
Technology, Excel Engineering
College, TN
India

² Department of Chemical
Engineering, Kongu Engineering
College, TN,
India

³ Department of Chemical
Engineering, Mettu University,
Ethiopia

SCIENTIFIC PAPER

UDC 628.4.034:66:502

TWO-PHASE LEACHING FOR METAL RECOVERY FROM WASTE PRINTED CIRCUIT BOARDS: STATISTICAL OPTIMIZATION

Article Highlights

- Two-stage leaching was employed for the efficient recovery of heavy metals from PCBs
- Optimization by RSM results in a leaching efficiency of 97.06% Cu, 94.66% Sn, 96.64% Zn, and 96.89% Pb
- Simultaneous extraction has proved to be successful in separating and recovering heavy metals

Abstract

The rapid growth of technology is inevitable in humankind's life and has a significant stint in electronic waste (e-waste) generation. Electronic waste possesses tremendous environmental and health effects, and one such major contributor to it is printed circuit boards (PCBs). The present work deals with the recovery of heavy metals from PCBs by using aqua regia as a leaching reagent in two stages (first stage HCl and HNO₃ and second stage HCl and H₂SO₄). The response surface methodology was used to determine the optimal recovery conditions for the heavy metal ions: the recovery time of 5 h, the pulp density of 25 g/L, and the temperature of 90.1 °C with desirability 0.761. These optimized values provide a maximum recovery rate of Cu (97.06%), Sn (94.66%), Zn (96.64%), and Pb (96.89%), respectively. EDXs are used to analyze the metal concentrations of the sample before and after treatment.

Keywords: aqua regia, e-Waste, printed circuit board, response surface methodology, two-step leaching.

Electronic waste (e-waste) means electrical or electronic waste. Technological advancement, business expansion, economic growth, and shorter electrical and electronic equipment (EEE) have contributed to a significant rise in e-waste. PCBs are the main components of this e-waste, which typically includes 40% metals, 30% ceramics, and 30% plastics [1,2]. The metallic composition consists primarily of 10–30 % of Cu and other metals such as Sn, Zn, Pb, Ni, Fe, Ag, Cd, Au, etc., in different proportions based on PCB sources [3]. The recovery of metals from PCBs is very difficult due to the heterogeneous distribution of materi-

als in PCBs. An analysis of PCBs by atomic adsorption spectroscopy shows that 2 kg of PCBs contains 5.94% of Sn, 21.3% of Cu, 3.2% of Pb, and 2.24% of Fe [4]. Informal processing of e-waste in developing countries can lead to adverse effects on human health and environmental pollution. In 2016, 44.7 million metric tons of e-waste were produced worldwide [1,2]. An estimated 3.8 tons of e-waste were produced annually in India, of which only 19,000 tons were recycled. India faces a considerable challenge to dispose of an estimated 4.5 tons of e-waste per year produced domestically and imports from abroad [5]. If the e-waste was directly disposed of by filling the soil without removing metal ions from PCBs, the pollution of land and water supplies would result.

E-waste recycling has been accomplished through formal and informal techniques in several countries [6]. While formal recycling techniques ensure protection and efficient separation but are costly to install and

Correspondence: M.M. Palanisamy, Department of Chemical Engineering, Erode Sengunthar Engineering College, TN, India.
E-mail: engineermurugesan@gmail.com
Paper received: 15 January 2021
Paper revised: 21 April 2021
Paper accepted: 15 June 2021

<https://doi.org/10.2298/CICEQ210115022M>

operate. Therefore, cheaper informal processes are highly admirable and oriented [7]. These metals can be found in dust, air, water, and soil, affecting human health and the environment. Exposure to metals such as Pb and Cd affects reproductive health, development, mental instability, and damage to human DNA [8-11]. Also, low levels of Pb exposure in children and pregnant women indicate major growth problems [12]. It also reported that the lung dysfunction of workers, such as diggers and scrap disposers, is due to the inhalation of nickel-contaminated air [9,13,14]. Health symptoms, like headache, dizziness, irritation in the eye, nose, mouth, etc., are due to exposure to Cu, which is present in the landfills [15-17].

The methods used to recover metals from PCBs are essentially physical/mechanical and chemical separation. As far as chemical separation is concerned, electro-winning, hydrometallurgy, and pyrometallurgy have been widely used [18]. The pyrometallurgy process involves heating e-waste at high temperatures to recover precious metals. This procedure develops dangerous gases, which must be extracted from the air using a flue gas cleaning device [19]. Several studies on the feasibility of metal recovery from PCBs have been published in the last decade. Hydrometallurgical procedures, such as leaching, are very crucial in these studies. Several leaching reagents demonstrate major improvements in metal recovery. When treated with different acidic media HNO₃, HCl, and H₂SO₄, PCBs were cut to extract Cu²⁺ ions, the recovery % of Cu²⁺ was 97.5%, 65%, and 76.5%, respectively [18]. Just traces of other metals can be extracted through this copper targeted extraction. While using HCl as leaching reagent under the stated conditions, the PCBs sample of size 4x4 cm results in separation of Cu, Zn, Sn, and Pb with composition 117.33 mg g⁻¹, 28.97 mg g⁻¹, 10.41 mg g⁻¹, and 9.34 mg g⁻¹, respectively [19]. The Zn and Pb leached amounts were very small compared to the typical PCB metal content. By leaching crushed PCBs (size between 0.43-3.33 mm) using sodium cyanide solution, the grades are 16%, 2.0%, 1%, and 1% of Cu, Pb, Zn, and Sn, respectively [20]. It has the most negligible compositional value compared to the average weight of the total metals. PCB waste leaching with H₂SO₄ and H₂O₂ yielded 76% Zn, 85% Cu, 82% Fe, 77% Al, and 70% Ni after 480 min of leaching [21]. Other valuable metals remain as traces in the leaching solution. The deposition of extracted metals possesses different dendritic growth concerning the leaching reagent used. The copper obtained by leaching of PCBs with H₂SO₄ solution presented a fine dendritic structure with branches of about 80-100 μm [22,23]. Besides that, the significant recovery rate of copper through bioleaching was reported in our previous research [24,25].

Several studies showed that heavy metals were successfully extracted from printed circuit boards by hydrometallurgical techniques. There were limitations such as the sluggishness of the process; higher processing times, which had resulted in less efficient recovery and had an impact on the recycling economy. Few researchers proposed methods of hydrometallurgical leaching followed by selective extraction of metals, which is more costly. The proposed recovery process utilizes two stages of leaching, which gave a more efficient recovery of heavy metals. This study deals with extracting metal ions such as Zn²⁺, Sn²⁺, Cu²⁺, Pb²⁺, etc., from PCBs by two-stage leaching technology. Furthermore, the experimental results are optimized through RSM at various parameters, like shaking speed, size, contact time, pulp density, and temperature.

MATERIALS AND METHODS

Sample collection and preparation

The waste PCBs were obtained from the e-waste disposal units in India. For the experiments, 500 g of PCB scraps were broken into 15-20 cm particles and shredded using pliers and four-blade cutting shredder into small pieces around 50x50-30x30 mm [22,23,26-28]. Metals and non-metals need to be separated [22,23]. This separation is not simple due to the difference in the physical characteristics of metals and non-metals, so different separation methods, such as pneumatic separation, magnetic separation, filtering, eddy current separation, electrostatic separation, etc., can be used to enrich metals and non-metals [20]. The electronic components, such as a capacitor, diode, resistor, transistors, etc. [29], are disassembled. These shredded PCBs were then heated at 700-900 °C in a muffle furnace to enhance the PCBs' flexibility and crushing properties [19,27]. Therefore, samples are comminuted using a jaw crusher to reduce the particle size. The crushed PCBs obtained from the crusher were then pulverized and milled using a ball mill to reduce the particles further. Particles of different mesh sizes were analyzed. The step-wise procedure employed is explained in Fig.S1 (available from the author, upon request).

The crushed PCBs fraction from the lower screens of jaw crushers of an 80 kg hr⁻¹ capacity with a clearance of 10 mm was not feasible for a better ions recovery. Thus, it was further subjected to the 5 mm clearance jaw crusher, resulting in the samples of 65, 53, 48, or 36 g from the sieves with a mesh size of 0.3, 0.18, 0.05 mm, and pan, respectively, when screened using a rotary sieve shaker (0.25 HP. 80 V) at a speed of 60 rpm. As

the reduction in size increased the recovery rate of metal ions [8], the resulting crushed samples were processed into the powder form using a pulverizer with a disk diameter of 175 mm operated by a three-phase motor (225–445 V) at 1400 rpm. The resulting powder samples were screened through sieves of different mesh sizes, and the weight fraction of the bottom product (sieves from 52 B.S.S. to pan) increased but was not adequate for the anticipated recovery. The pulverized PCB powder was milled in a ball mill having 5000 g balls at a speed of 60–120 rpm with a mill diameter of 200 mm driven by a 0.25 HP three-phase motor, which resulted in a much size reduction; the highest weight fraction was obtained at the lowest sieve. The weight fractions obtained at each sieve were separately collected and used for leaching (Table 1).

Mixture compositions

The metal recovery from PCB was carried out in two leaching stages using HCl and HNO₃ in the first stage and HCl and H₂SO₄ in the second stage. The leaching agent was prepared by mixing HCl and HNO₃ in a 3:1 ratio under the specified conditions. In previous studies with aqua regia as a leaching reagent, heavy metals, such as Cu, Sn, Pb, and Zn, were extracted from PCBs with a high recovery rate (Table 2).

The aqua regia preparation mixing concentrated strong acids, namely HCl (35%) and HNO₃ (65%), in a 3:1 ratio. The solutions were kept away from the organic contaminants to avoid vigorous or violent reactions at a low temperature.

Table 1. Analysis of PCBs size reduction

Mesh size		Weight fraction (grams)			
		Jaw crusher		Pulveriser	Ball mill
B.S.S	(mm)	Clearance (10 mm)	Clearance (5 mm)	Feed size (6 mm)	Ball weight (500g)
4	4	155	118	45	27
7	2.3	125	92	57	35
25	0.6	95	76	69	58
52	0.3	52	65	87	64
85	0.18	30	53	60	78
300	0.05	22	48	85	82
Pan	-	15	36	79	120

Table 2. Recovery data of metals with different leaching agents

Leaching media used	Heavy metals recovery %									References
	Cu	Sn	Zn	Pb	Cr	Ni	Ag	Au	Fe	
H ₂ SO ₄ + H ₂ O ₂	96.72	-	98	-	53.03	97.7	-	-	0.44	[22]
HNO ₃ and HCl+ HNO ₃	86.9	92.7	-	-	-	-	-	-	-	[23]
HCl + HNO ₃	92.7	93.3	-	-	-	-	-	-	-	[26]
NaCN	77.7	-	-	-	-	-	51.6	47.9	-	[27]
(NH ₄) ₂ S ₂ O ₃ and CuSO ₄	78.8	-	56.7	-	-	-	-	-	-	[28]
H ₂ SO ₄ + NH ₃	88.6	-	99.2	-	98.2	98	-	-	-	[30]

Experimentation with various parameters on metal recovery

All the experiments were conducted in conical flasks fixed at a temperature-controlled shaker. The primary analysis was performed by applying the specific conditions to obtain a standard recovery rate. Namely, 20 g of PCB samples were treated with 0.5 L of the leaching agent in the conical flask at 80 °C and shaken by the shaker at a shaking speed of 120 rpm for 3 h. At the end of this effective contact time, the shaker was stopped, and the solution in the conical flask was filtered using filter paper. After filtration, the metal composition of the retained filtrate was determined. The leaching rate depends on various parameters, such as shaking intensity, particle size, contact time, pulp density, and temperature. Different values for the recovery rate and the composition of heavy metals were obtained by varying these parameters.

Pulp density

The 0.05 mm PCBs samples (5, 10, 15, 20, and 25 g) were taken in separate conical flasks, and 0.5 L of aqua regia was inserted in each flask. The conical flasks were securely closed using a lid, fixed on the shaker, and shaken (80 rpm) at 80 °C for 3 h. After 2 h, the solutions in the conical flasks were filtered separately using filter paper. The metal components deposited on the filter paper were dried and analyzed.

Temperature

Some acids improve the recovery rate with increased temperature, while others exhibit a decreased recovery rate at higher temperatures [31].

However, the dissolved oxygen concentration of the aqueous phase is reduced as the temperature increases. The 0.3 mm particles (20 g) were mixed with 0.5 L of aqua regia in a conical flask and shaken for 3 h in a shaker at 120 rpm at 20, 40, 60, 80, and 100 °C. After shaking, the solutions were filtered and analyzed.

Time

Duration is another primary parameter influencing the recovery rate. The leaching rate rises with time, but there is no appreciable recovery after a certain period. The time range with the maximum recovery rate is known as the efficacy of the leaching cycle [22,23]. The samples were combined 0.5 L of the leaching agent with 20 g of 0.3 mm particles in conical flasks and shaken separately at 80 rpm for 1, 2, 3, 4, and 5 h at 80 °C. The solutions were filtered, dried, and analyzed.

Shaking Speed

The collision between the leaching agent and the PCB particles increases with increasing the shaking speed, leading to an increased ion exchange rate. The effect of shaking speed was tested at 40, 80, 120, 160, and 200 rpm. In these experiments, 5 g of 0.3 mm PCB particles were shaken with 0.5 L of aqua regia at 80 °C. The solution collected at each speed was filtered and analyzed.

Size

The sample size has an essential role in metal leaching. The leaching rate can increase or decrease with a change in the particle size. The PCB samples (20 g) containing 4, 2.3, 0.6, 0.3 mm, or <0.05 mm particles were combined with 0.5 L of the leachate agent in different conical flasks. The mixtures in conical flasks were shaken for 2 h at 80 rpm at 80 °C. The resulting solutions were filtered, and the filtrates were analyzed.

Response surface methodology (RSM)

The study was conducted to obtain the optimum values of various parameters for recovering metal ions from PCBs by the response surface methodology [31]. The influence of various process factors (shaking speed, size, contact time, pulp density, and temperature) are studied for metal ions recovery. In the present study, the input process factors were temperature, pulp density, and time. The levels of the selected process factors in coded and uncoded forms correspond to the Box-Behnken design (Table 3). The response (output variable) is the metal recovery (in %).

Table 3. Levels of different process variables in coded and uncoded form chemical leaching % of heavy metals (Box-Behnken Method)

Variable	Name of the Process Variable	Range and levels		
		-1	0	1
A	Time, h	3	4	5
B	Temperature, °C	60	80	100
C	Pulp density, g L ⁻¹	15	20	25

RESULTS AND DISCUSSION

Sample analysis of PCBs (Sizes and metal elements)

The graphical representation of the size analysis reveals that subject to the size decrease sequence, the fraction of sample generated on the screens with larger mesh sizes has decreased. However, the total weight collected in the sieves was maintained roughly with marginal loss. The sample collected at the ball mill was much less than 0.05 mm from the analytical data of each procedure. Numerous experiments were used a shredded sample dimension less than 0.5 mm, contributing to an elevated heavy metal recovery rate [32-35]. The graphical representation of the PCB sample size analysis showed that the fraction of the sample obtained in the sieves with larger mesh size decreased when it was subjected to a sequence of size reduction operations. Various studies used a shredded sample size of less than 0.5 mm, which resulted in a high recovery rate of heavy metals [32]. The present work used the 0.05 mm particles, while the same analyses were performed. Fig. S2 (available from the author upon request) shows the results obtained with the 0.05 mm sample.

EDXs and SEM were used to analyze the metal concentrations of the preliminary samples. To ensure uniformity and to obtain metal composition by SEM with EDXs, the samples were randomly mixed, and the final contents of the metals were as follows: 3.15% Cu, 42.4% Sn, 1.16% Zn, 27.81% Pb, and 25.48% the other metals (Fig.1).

Experimental results

Effect of pulp density

The recovery rate increases with an increase in the pulp density of the sample over time [34]. After reaching the state of equilibrium, the recovery becomes constant. The graph (Fig. 2) shows an improvement in

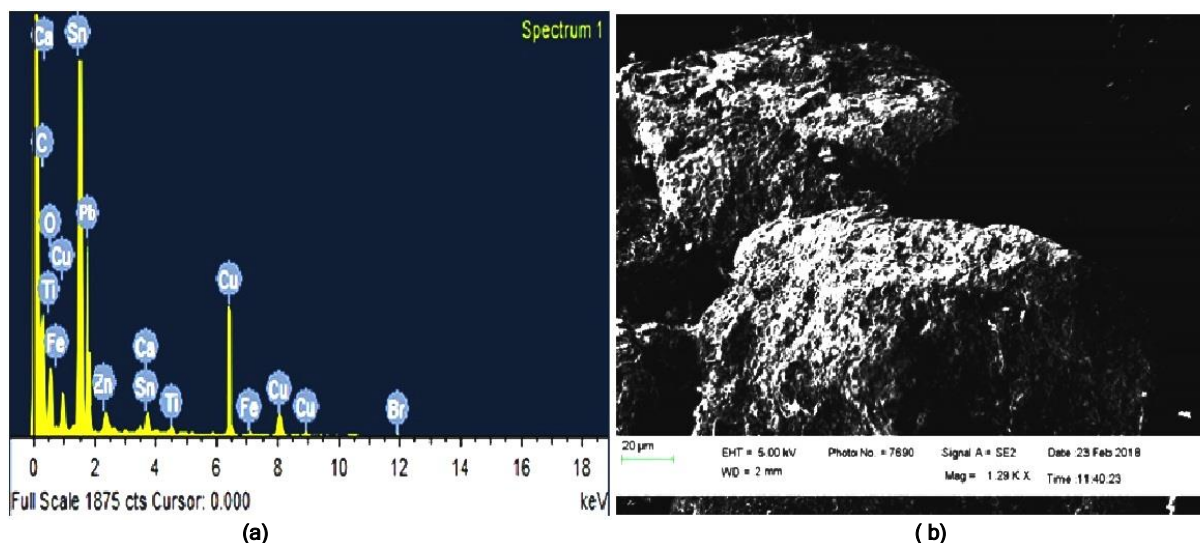


Figure 1. Presence of metals from PCBs sample by a) EDXS & b) SEM images

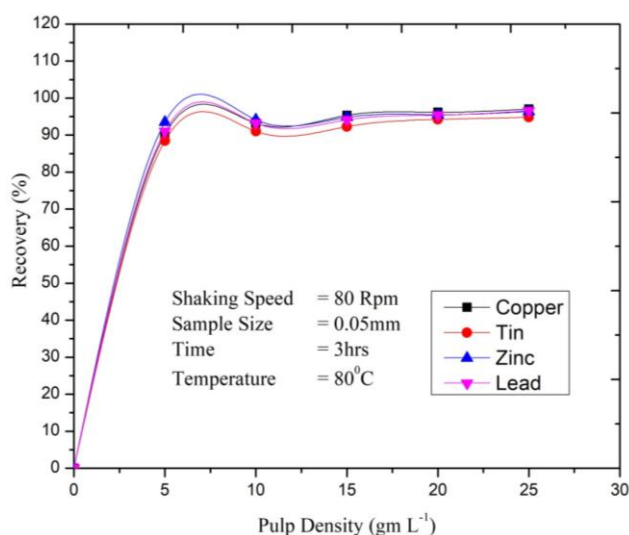


Figure 2. Graphical representation of % recovery of metals with a pulp density.

the PCB pulp density. The metals recovered in the deteriorating order of Cu, Sn, Zn, and Pb. The pulp densities were improved by 5 g L⁻¹, and all metals displayed a marginal improvement in recovery rates of 97.06% Cu, 94.87% Sn, 96.39% Zn, and 96.60% Pb.

Effect of temperature

Fig. 3a shows an appreciable rise in the recovery with increased temperature. The previous results show no noticeable improvement in recovery at temperatures above 80 °C [36]. Thus, the leaching depends on temperature only up to a certain limit above which it is independent of the temperature. At 80 °C, the following recoveries were achieved: 97.46% of Cu, 93.59% of Sn, 92.56% of Zn, and 97.84% of Pb.

Effect of Time

Fig. 3b shows that the metal recovery increases with an increase in the time over some time, and after

that, it becomes almost constant. After 3 h leaching, the metal recovery values were 97.46% Cu, 93.56% Sn, 92.56% Zn, and 96.91% Pb.

Effect of Speed

Fig. 3c indicates the relationship between the metal recovery and shaking intensity. At first, the recovery increases by increasing the shaking speed while decreasing at higher speeds [37]. The ionic metal dissociation depends on how long the acid holds on the sample's surface. As the speed increases, there is insufficient time to detach ions from the metal surface because of a shorter interaction time between the metal surfaces and the leaching agent. The result shows a complete metal regeneration at a speed of 80 rpm. It gives a recovery of 95.35% of Cu, 97.76% of Sn, 96.39% of Zn, and 98.76% of Pb.

Effect of Size

In the study of leaching the particles of different sizes using aqua regia, the highest recovery rate was obtained with the PCB sample with the smallest particle size (0.05 mm). The recovery values were as follows: 95.79% of Cu, 93.59% of Sn, 92.56% of Zn, and 97.84% of Pb (Fig. 3d).

Optimization parameters by Design of Experiments (DOE)

The present study used the central composite design (CCD) with three factors. The experimental design had 17 runs, including 8 (2³) factorial points, 6 (2×3) axial points, and 5 center points were conducted. All experiments were done using 250 ml Erlenmeyer flasks containing 50 ml solution while the shaking speed and the sample size were adjusted at 80 rpm and 0.05 mm, respectively. The CCD for Cu, Sn, Zn, and Pb leaching was combined with the RSM to optimize the

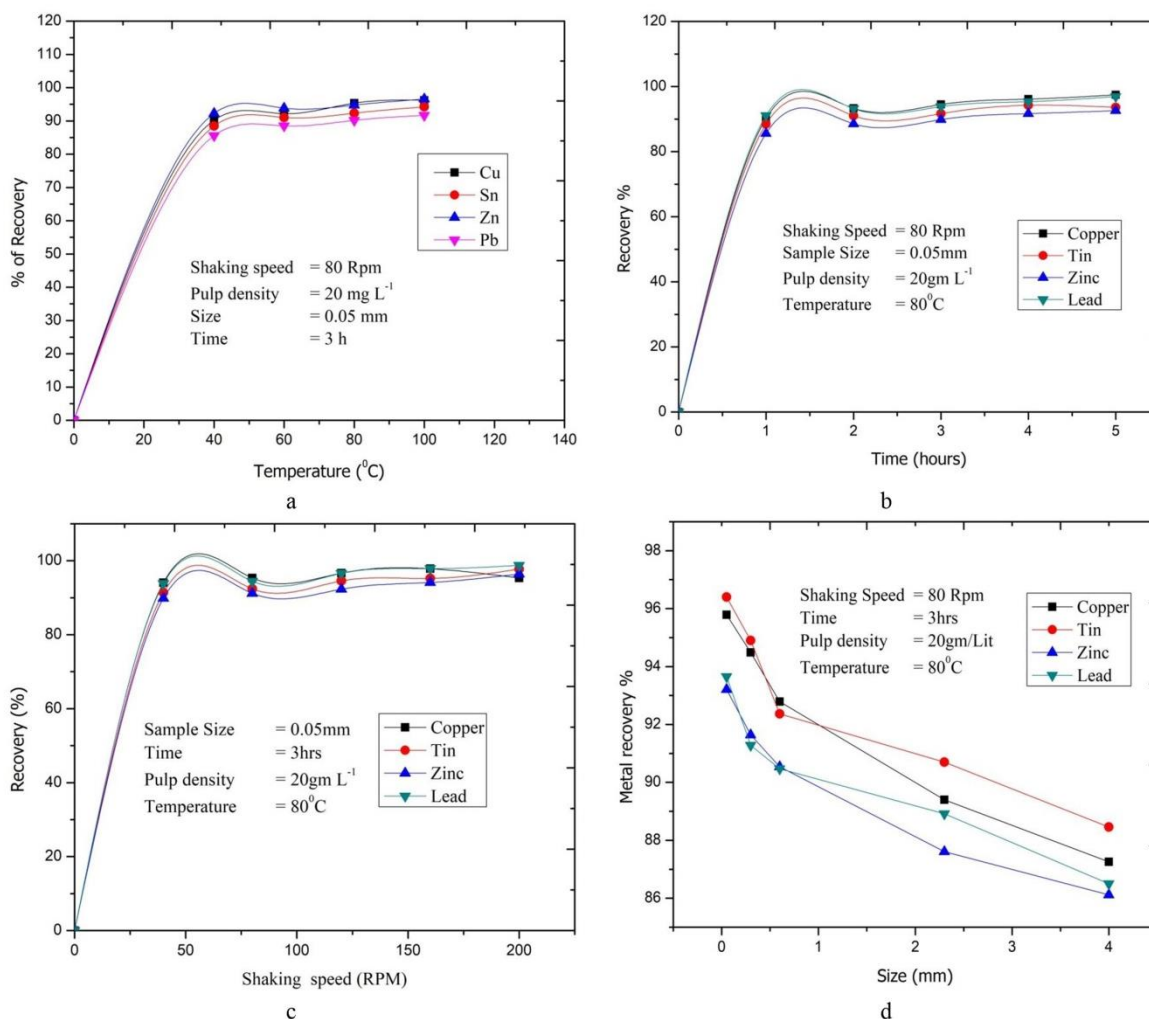


Figure 3. Graphical representation of % recovery of: a) metals with temperature; b) metals with time; c) metals with shaking speed; d) metals with size.

operating parameters and the maximum metal recovery Table 4.

RSM for heavy metals (Cu, Sn, Zn, and Pb) from PCBs

$$\% \text{ of } C = +94.61 + 0.1 \cdot A + 2.01 \cdot B + 1.21 \cdot C + 0.21 \cdot A \cdot B - 0.14 \cdot A \cdot C - 0.57 \cdot B \cdot C - 0.54 \cdot A^2 - 1.42 \cdot B^2 - 0.45 \cdot C^2 \quad (1)$$

$$\% \text{ of } Sn = +91.62 + 0.014 \cdot A + 1.62 \cdot B + 1.35 \cdot C + 0.41 \cdot A \cdot B + 0.37 \cdot A \cdot C - 0.57 \cdot B \cdot C - 0.27 \cdot A^2 - 1.14 \cdot B^2 - 0.58 \cdot C^2 \quad (2)$$

$$\% \text{ of } Zn = +89.49 - 0.20 \cdot A + 1.96 \cdot B + 1.63 \cdot C + 0.40 \cdot A \cdot B + 0.89 \cdot A \cdot C - 0.68 \cdot B \cdot C - 0.77 \cdot A^2 - 1.49 \cdot B^2 - 0.50 \cdot C^2 \quad (3)$$

$$\% \text{ of } Pb = +93.71 - 0.030 \cdot A + 1.78 \cdot B + 1.31 \cdot C - 0.075 \cdot A \cdot B + 0.38 \cdot A \cdot C - 0.72 \cdot B \cdot C - 0.62 \cdot A^2 - 1.19 \cdot B^2 - 0.84 \cdot C^2 \quad (4)$$

where *A* represents the contact time (h), *B* is the temperature (°C), and *C* is the pulp density (g L⁻¹). The response of each parameter was predicted within the limits through the model in function of coded factor. Here, the maximum and minimum coded factor levels are +1 and -1. The response surface was visualized in three-dimensional plots that exhibit the two factors' functions while keeping the third factor constant. The interaction between the pulp density and the temperature was observed when the time was kept constant at the optimal value (4 hours). The

The multiple nonlinear regression was used to determine the multivariable equation connecting the Cu, Sn, Zn, and Pb recoveries with the coded leaching variables (Table 4):

effect of these parameters on the Cu separation was significant, up to their optimal values. However, the effect was insignificant or negative when exceeding the optimal concentrations. Furthermore, the pulp density positively affected the recovery when the concentration of the leaching agent increased at a constant contact time. Similarly, the recovery rate increased initially in the first two hours and then slightly decreased due to the reduction of the Sn concentration. Figures 4(c) and 4(d) show the surface plots indicating the simultaneous effect of the two

factors on the Zn and Pb extraction, while the third factor was at the center level. The predicted design plots (Fig.4a-d) show the red zones above 95.38% of Cu, 92.49% of Sn, 90.96% of Zn, and 94.7% of Pb

and the yellow zones above 93% of Cu, 91% of Sn, 89% of Zn, and 93% of Pb, and the blue zones above 88.95% of Cu, 86.36% of Sn, 83.65% of Zn, and 88.51% of Pb

Table 4. Experimental and predicted results from CCD with optimal parameters for leaching

Run no.	A	B	C	Leaching of heavy metals (%)							
				Experimental				Predicted			
				Cu	Sn	Zn	Pb	Cu	Sn	Zn	Pb
1.	-1	-1	0	90.68	88.99	85.51	90.07	90.6875	88.9875	85.49625	90.07125
2.	1	-1	0	90.6	88.2	85.9	90.16	90.5925	88.19	85.89625	90.16125
3.	-1	1	0	94.27	91.4	90.2	93.79	94.2775	91.41	90.20375	93.78875
4.	1	1	0	95.05	92.26	89	93.58	95.0425	92.2625	89.01375	93.57875
5.	-1	0	-1	92.1	89.78	88.1	91.34	92.1	89.77625	88.10125	91.34125
6.	1	0	-1	92.7	89.06	85.94	90.53	92.715	89.06375	85.93125	90.53125
7.	-1	0	1	94.82	91.73	89.57	93.22	94.805	91.72625	89.57875	93.21875
8.	1	0	1	94.86	92.49	90.96	93.91	94.86	92.49375	90.95875	93.90875
9.	0	-1	-1	88.95	86.36	83.65	88.51	88.9425	86.36625	83.6625	88.5075
10.	0	1	-1	94.11	90.75	88.94	92.22	94.1025	90.74375	88.935	92.22
11.	0	-1	1	92.5	90.18	88.27	91.28	92.5075	90.18625	88.275	91.28
12.	0	1	1	95.38	92.31	90.84	94.7	95.3875	92.30375	90.8275	94.7025
13.	0	0	0	94.8	91.77	90.25	93.8	94.612	91.62	89.92	93.712
14.	0	0	0	94.62	91.6	90	93.44	94.612	91.62	89.92	93.712
15.	0	0	0	94.5	91.6	89.8	93.8	94.612	91.62	89.92	93.712
16.	0	0	0	94.56	91.68	89.67	93.75	94.612	91.62	89.92	93.712
17.	0	0	0	94.58	91.45	89.88	93.77	94.612	91.62	89.92	93.712

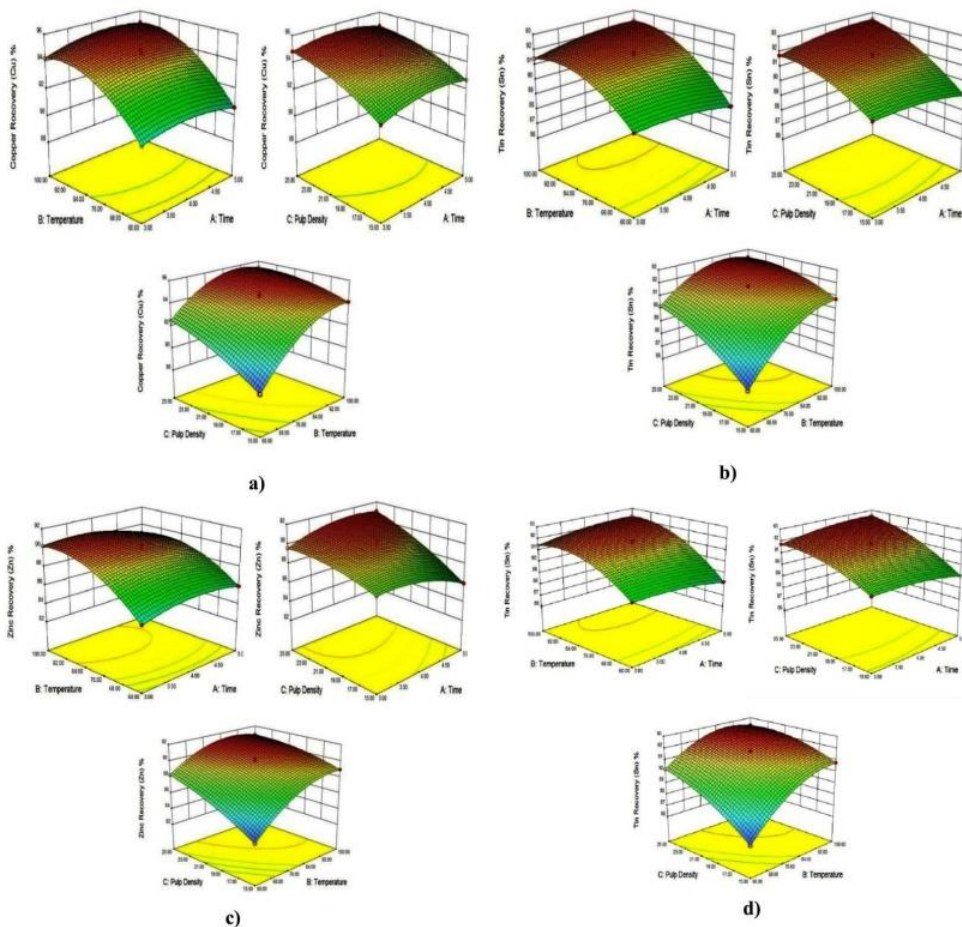


Figure 4. RSM plots and Interactions between the pulp density, temperature, and time by a) Cu; b) Sn; c) Zn; d) Pb recovery rate.

Evaluation of the model

The stability models were validated using the analysis of variance (ANOVA) (Table 5). The low probability (<0.05) with F-values of 848.04, 633.92, 286.97, and 425.51 for Cu, Sn, Zn, and Pb, respectively, implied that the model was accurate. Also, the acceptable and reasonable values of the lack of fit with F-value of 0.023 0.010, 0.006, and 0.0004 for Cu, Sn, Zn, and Pb, respectively, with the probability values higher than 0.05 indicated the suitability of the developed equations on an excellent presentation of the experimental data.

As presented in Table 6, the model has high R^2 values of 0.999, 0.999, 0.997, and 0.998 for Cu, Sn, Zn, and Pb, respectively, indicating a good agreement between the experimental and predicted values. Also, the predicted R^2 values of 0.998, 0.998, 0.996, and 0.997 for Cu, Sn, Zn, and Pb, respectively, are in reasonable agreement with the adjusted R^2 values of 0.998, 0.997, 0.994, and 0.996 for Cu, Sn, Zn, and Pb, respectively. The model's adequate precision (signal to noise ratio) was found to be 96.96, 89.14, 57.04, and 69.590 for Cu, Sn, Zn, and Pb, respectively, which indicated an adequate signal and demonstrated that this model could be used to navigate the design space. The predicted values of the responses were in agreement with the observed values over the selected range of the independent

variables with the reasonably higher values of the coefficient of determination (R^2), as can be seen in Fig. 5a.

Desirability plot for recovery of heavy metals from PCBs

The desirability profile for the heavy metals removal versus the variables is shown in Fig. 5b. The desirability varies from 0.0 to 1.0, corresponding to approaching the undesirable to the very desirable condition. The optimum removal of 95.33% of Cu, 92.95% of Sn, 90.99% of Zn, and 94.44% of Pb was obtained under the following operating conditions: the leaching time of 5 h, the temperature of 90.01 °C, and the pulp density of 25 g L⁻¹ with the desirability of 0.761.

Maximum recovery by optimization study

Under the optimum conditions, i.e., the time of 5 h, the temperature of 90.01 °C, and the pulp density of 25 g L⁻¹ (20 g of the sample treated with 0.5 L of aqua regia, 80 rpm of shaking speed, and 0.05 mm of particle size, the recovery of heavy metals were 97.06% of Cu, 94.66% of Sn, 96.64% of Zn, and 96.89% of Pb.

The metal contents present in the PCB after leaching were 0.09% of Cu, 2.28% of Sn, 0.04% of Pb, 0.91% of Zn, and 1.72% of the others (Fig. 6)

Table 5. ANOVA table for the model to predict % of leaching of copper, tin, zinc, and lead

Source	Model to predict % of leaching of Cu					Model to predict % of leaching of Sn				
	Sum of Squares	df	Mean Square	F-value	p-value Prob> F	Sum of Squares	df	Mean Square	F-value	p-value Prob> F
Model	57.33024	9	6.370027	848.0447	< 0.0001	45.82593	9	5.09177	633.9242	< 0.0001
A-Time	0.22445	1	0.22445	29.88113	0.0009	0.001513	1	0.001513	0.188306	0.4774
B-Temp	32.3208	1	32.3208	4302.883	< 0.0001	21.09251	1	21.09251	2626.013	< 0.0001
C-P den	11.76125	1	11.76125	1565.781	< 0.0001	14.4722	1	14.4722	1801.786	< 0.0001
AB	0.1849	1	0.1849	24.61582	0.0016	0.680625	1	0.680625	84.73766	< 0.0001
AC	0.0784	1	0.0784	10.43743	0.0144	0.5476	1	0.5476	68.17608	< 0.0001
BC	1.2996	1	1.2996	173.0164	< 0.0001	1.2769	1	1.2769	158.9738	< 0.0001
A ²	1.220978	1	1.220978	162.5494	< 0.0001	0.309796	1	0.309796	38.56954	0.0004
B ²	8.532009	1	8.532009	1135.87	< 0.0001	5.436059	1	5.436059	676.7882	< 0.0001
C ²	0.865946	1	0.865946	115.2838	< 0.0001	1.434796	1	1.434796	178.6318	< 0.0001
Residual	0.05258	7	0.007511	-	-	0.056225	7	0.008032	-	-
Lack of Fit	0.0009	3	0.0003	0.02322	0.9945	0.000425	3	0.000142	0.010	0.4984
Pure Error	0.05168	4	0.01292	-	-	0.0558	4	0.01395	-	-
Cor Total	57.38282	16	-	-	-	45.88215	16	-	-	-

Table 5. ANOVA table for the model to predict % of leaching of copper, tin, zinc, and lead (Continued)

Source	Model to predict % of leaching of Zn					Model to predict % of leaching of Pb				
	Sum of Squares	df	Mean Square	F-value	p-value Prob> F	Sum of Squares	df	Mean Square	F-value	p-value Prob> F
Model	71.84526	9	7.982807	286.967	< 0.0001	51.59225	9	5.732472	425.5056	< 0.0001
A-Time	0.31205	1	0.31205	11.21761	0.0123	0.0072	1	0.0072	0.534436	0.4885
B-Temp	30.61531	1	30.61531	1100.563	< 0.0001	25.45411	1	25.45411	1889.389	< 0.0001
C-P den	21.15751	1	21.15751	760.5731	< 0.0001	13.80751	1	13.80751	1024.894	< 0.0001
AB	0.632025	1	0.632025	22.72012	0.0020	0.0225	1	0.0225	1.670113	0.2373
AC	3.150625	1	3.150625	113.2591	< 0.0001	0.5625	1	0.5625	41.75282	0.0003
BC	1.8496	1	1.8496	66.48966	< 0.0001	0.021025	1	0.021025	1.560628	0.2517
A ²	2.528947	1	2.528947	90.91093	< 0.0001	1.617221	1	1.617221	120.0419	< 0.0001
B ²	9.379184	1	9.379184	337.1642	< 0.0001	5.985095	1	5.985095	444.2571	< 0.0001
C ²	1.063184	1	1.063184	38.21949	0.0005	2.986884	1	2.986884	221.7082	< 0.0001
Residual	0.194725	7	0.027818	-	-	0.094305	7	0.013472	-	-
Lack of Fit	0.000925	3	0.000308	0.006364	0.9992	2.5E-05	3	8.33E-06	0.000354	1.0000
Pure Error	0.1938	4	0.04845	-	-	0.09428	4	0.02357	-	-
Cor Total	72.03999	16	-	-	-	51.68655	16	-	-	-

Table 6. Quality of the quadratic model for the leaching of heavy metals

Parameters	Cu	Sn	Zn	Pb
Standard deviation (SD)	0.087	0.090	0.170	0.120
Mean	93.48	90.68	88.62	92.46
Coefficient of variation (CV %)	0.092	0.099	0.190	0.130
Predicted residual error sum of squares (PRESS)	0.095	0.094	0.320	0.150
R-Squared(R ²)	0.999	0.999	0.997	0.998
Adj R-Squared (R ² _{adj})	0.998	0.997	0.994	0.996
Pred R-Squared (R ² _{pred})	0.998	0.998	0.996	0.997
Adequate precision (AP)	96.96	89.14	57.04	69.59

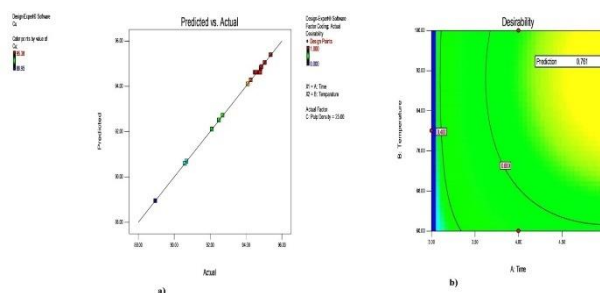


Figure 5. a) Comparison plot between the experimental and predicted data b) Desirability plot for recovery of heavy metals from PCBs.

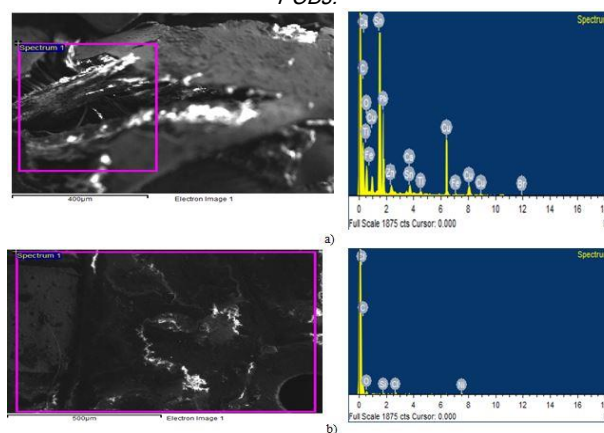


Figure 6. EDXs spectrum analysis for metal ions obtained before (a) Metals composition in before treatment of (PCBs) and after (b) Metals composition in after-treatment of (PCBs) PCBs.

CONCLUSION

The two-phase leaching was used to recover the heavy metals from PCBs under various operating conditions. Temperature, time, and pulp density were the most crucial process factors, while the particle size and the shaking speed showed a marginal effect on the metal recovery. The optimum removal of 95.33% of Cu, 92.95% of Sn, 90.99% of Zn, and 94.44% of Pb with the desirability of 0.761 was achieved in 5 h, the temperature of 90.01 °C, and the pulp density of 25 g L⁻¹. Hence, this metal leaching process was proposed to reduce the environmental impacts of e-wastes caused by the leaching of heavy metals.

Acknowledgment

This study was carried out using the laboratory facilities in the Erode Sengunthar Engineering College and Kongu Engineering College. The corresponding author would like to acknowledge and thank his parents and brother Dr. P. Selvarasu, PG Assist Zoology, Govt Higher Secondary School, Vellore, for their kind support.

Nomenclature

CCD	-	Central Composite Design
Cu	-	Copper
e-waste	-	Electronic Waste
EDS	-	Scanning Electron Microscopy
EDXs	-	Energy-Dispersive X-Ray Spectroscopy
EEE	-	Electrical and Electronic Equipment
H ₂ SO ₄	-	Sulphuric acid
HCl	-	Hydrochloric acid
HNO ₃	-	Nitric acid
P den	-	Pulp density
Pb	-	Lead
PCBs	-	Printed Circuit Boards
RSM	-	Response Surface Methodology
Sn	-	Tin
WEEE	-	Waste of Electrical and Electronic Equipment
Zn	-	Zinc

REFERENCES

- [1] H. Yang, J. Liu, J. Yang, *J. Hazard. Mater.* 187 (2011) 393-400.
- [2] L. Wei, Y. Liu, *Procedia Environ. Sci.* 16 (2012) 506-514.
- [3] M.F. Bari, N. Begum, S.B. Jamaludin, S.B. Hamaludin, *Proc. Malays. Metall. Conf., Univ. Malays. Perlis, Malaysia* (2009) p. 1-4.
- [4] L. Flandinet, F. Tedjar, V. Ghetta, J. Fouletier, *J. Hazard. Mater.* 1 (2012) 485-490.
- [5] L.A. Castro, A.H. Martins, *Braz. J. Chem. Eng.* 26 (2009) 649-657.
- [6] S. Gupta, G. Modi, R. Saini, *Int. Ref. J. Eng. Sci.* 3 (2014) 05-17.
- [7] D. Jian-Jun, W.E.N. Xue-Feng, Z. Yue-Min, *Int. J. Min. Sci. Technol.* 18 (2008) 454-458.
- [8] C. Frazzoli, O. Ebere, R. Dragone, A. Mantovani, *Environ. Impact Assess. Rev.* 30 (2010) 388-399.
- [9] J. Zhang, Y. Jiang, J. Zhou, B. Wu, Y. Liang, Z. Peng, D. Fang, B. Liu, H. Huang, C. Wang, F. Lu, *Environ. Sci. Technol.* 44 (2010) 3956-3962.
- [10] X. Xu, H. Yang, A. Chen, Y. Zhou, K. Wu, J. Liu, Y. Zhang, X. Huo, *Reprod. Toxicol.* 33 (2012) 94-98.
- [11] X. Huo, L. Peng, X. Xu, L. Zheng, B. Qiu, Z. Qi, B. Zhang, D. Han, Z. Piao, *Environ. Heal. Perspect.* 115 (2007) 1113-1117.
- [12] M.A. Barakat, *Hydrometallurgy* 49 (1998) 63-73.
- [13] Y. Guo, X. Huo, Y. Li, K. Wu, J. Liu, J. Huang, G. Zheng, Q. Xiao, H. Yang, Y. Wang, A. Chen, X. Xu, *Sci. Total Environ.* 408 (2010) 3113-3117.
- [14] K. Huang, J. Guo, Z. Xu, *J. Hazard. Mater.* 164 (2009) 399-408.
- [15] Y. Li, X. Huo, J. Liu, L. Peng, W. Li, X. Xu, *Environ. Monit. Assess.* 177 (2011) 343-351.
- [16] V. Grudić, I. Bošković, A. Gezović, *Chem. Biochem. Eng. Q.* 32 (2018) 299-305.
- [17] M. Chen, J. Huang, O.A. Ogunseitan, N. Zhu, Y. Wang, *J. Waste Manage.* 41 (2015) 142-147.
- [18] I. Masavetas, A. Moutsatsou, E. Nikolaou, S. Spanou, A. Zoikis-Karathanasis, E.A. Pavlatou, *Glob. NEST J.* 11(2009) 241-247.
- [19] H. Li, J. Eksteen, E. Oraby, *Resour. Conserv. Recycl.* 139 (2018) 122-139.
- [20] R. Montero, A. Guevara, E. De La Torre, *Int. J. Earth Sci. Eng.* 2 (2012) 590-595.
- [21] J. Ficeriova, P. Baláž, E. Gock, *Acta Montan. Slovaca.* 16 (2011) 128-131.
- [22] R. Vijayaram, K. Chandramohan *Res. J. Eng. Sci.* 4 (2013) 2-4.
- [23] R. Vijayaram, D. Nesakumar, K. Chandramohan, *Res. J. Eng. Sci.* 2 (2013) 11-14.
- [24] M.P. Murugesan, K. Kannan, *J. Ceram. Process. Res.* 21 (2020) 75 - 85.
- [25] M.P. Murugesan, K. Kannan, T. Selvaganapathy, *Mater. Today Proc.* 26 (2020) 2720 - 2728.
- [26] E. Kantarelis, W. Yang, W. Blasiak, C. Forsgren, A. Zabaniotou, *Appl. Energy* 88 (2011) 922-929.
- [27] A. Tripathi, M. Kumar, D.C. Sau, A. Agrawal, S. Chakravarty, *Int. J. Metall. Eng.* 1 (2012) 17-21.
- [28] E.Y. Yazici, H. Deveci, *Hydrometallurgy.* 139 (2013) 30-38.
- [29] G. Zheng, X. Xu, B. Li, K. Wu, T.A. Yekeen, X. Huo, *J. Exposure Sci. Environ. Epidemiol.* 23 (2012) 67-72.
- [30] C. Li, F. Xie, Y. Ma, T. Cai, H. Li, Z. Huang, G. Yuan, *J. Hazard. Mater.* 178 (2010) 823-833.
- [31] P. Sivakumar, D. Prabhakaran, M. Thirumarimurugan, *Bioinorg. Chem. Appl.* 1 (2018) 1-10.
- [32] Z. Ping, F. Zeyun, L. Jie, L. Qiang, Q. Guangren, Z. Ming,

- J. Hazard. Mater. 166 (2009) 746-750.
- [33] M. Kumar, J.C. Lee, M.S. Kim, J. Jeong, K. Yoo, Environ. Eng. Manag. J. 13 (2014) 2601-2607.
- [34] C. Wang, F. Lu, Environ. Sci. Technol. 44 (2010) 3956-3962.
- [35] Q. Wang, B. Gao, L. Chen, J. Environ. Sci. Health, Part A: Environ. Sci. Eng. 1 (2011) 37-41.
- [36] P. Zhu, Y. Chen, L.Y. Wang, M. Zhou, Waste Manage. 32 (2012) 1914-1918.

MURUGESAN M.
PALANISAMY¹

KANNAN KANDASAMY²
VENKATA R. MYNENI³

¹ Department of Food
Technology, Excel Engineering
College, TN
India

² Department of Chemical
Engineering, Kongu Engineering
College, TN,
India

³ Department of Chemical
Engineering, Mettu University,
Ethiopia

NAUČNI RAD

IZDVAJANJE METALA IZ OTPADNIH ŠTAMPANIH PLOČA DVOSTEPENIM LUŽENJEM: STATISTIČKA OPTIMIZACIJA

Brzi razvoj tehnologije je neizbežan i ima značajan udeo u generisanju elektronskog otpada (e-otpada). Elektronski otpad ima ogromne efekte na životnu sredinu i zdravlje ljudi, a veliki doprinos tome daju štampane ploče. Ovaj rad se bavi dobijanjem teških metala iz otpadnih štampanih ploča carskom vodom (aqua regia). kao reagensa za luženje u dve faze (prva faza HCl i HNO₃ i druga faza HCl i H₂SO₄). Metodologija površine odziva je korišćena za određivanje optimalnih uslova izdvajanja jona teških metala: vreme luženja od 5 h, gustina suspenzije od 25 g/l i temperatura od 90,1 oC sa vrednošću funkcije poželjnosti 0,761. Ovi optimalni procesni uslovi obezbeđuju maksimalnu stepen izdvajanja metala: Cu (97,06%), Sn (94,66%), Zn (96,64%) i Pb (96,89%). Energijska disperziona spektrofotometrijska (EDX) analiza je korišćena za analizu koncentracije metala u uzorku pre i posle tretmana.

Ključne reči: carska voda, e-otpad, štampana ploča, metodologija površine odziva, dvostepeno luženje.

FLORIN ENACHE ^{1,2}
DAN DĂNULESCU ¹
ION BOLOCAN ²
DIANA CURSARU ²

¹ Petrotel-Lukoil Refinery, 235
Mihai Bravu Street, 100410,
Ploiesti, Romania

² Department of Petroleum
Refining Engineering and
Environmental Protection,
Petroleum-Gas University of
Ploiesti, 39 Bucharest Boulevard,
100680, Ploiesti, Romania

SCIENTIFIC PAPER

UDC 665.64.097

THE REDUCTION OF FCCU AFTERBURNING THROUGH PROCESS OPTIMIZATION AND REGENERATOR REVAMPING

Article Highlights

- A methodology applied in FCC unit to investigate the afterburning causes
- Technical solutions to reduce the afterburning
- Symmetrical layout of the cyclones reduces the afterburning

Abstract

Operating the fluid catalytic cracking unit (FCCU) in afterburning conditions can increase the regenerator temperatures above the metallurgical design leading to mechanical failures of the cyclones and plenum chamber. This paper presents the methodology applied in a commercial FCCU to investigate the afterburning causes and the technical solutions that can be implemented to reduce the afterburning. Thus, by evaluating the regenerator temperature profile, regenerator as-build design, and the internals mechanical status, it was concluded that the main cause of afterburning was the non-uniform distribution and mixing of air and catalyst. The industrial results showed that optimizing the catalyst bed level, stripping steam, reaction temperature, and equilibrium catalyst (e-cat) activity reduced the afterburning by 39%. Other process parameters such as feed preheat temperature, slurry recycling, and excess oxygen did not significantly influence afterburning because of air and catalyst maldistribution. Revamping the regenerator to assure a symmetrical layout of cyclones reduced the afterburning by 86%, increased the fines retention in FCCU inventory, and provided a better regeneration of the spent e-cat. The reduction of operating temperatures at around 701 °C removed the risk of catalyst thermal deactivation, and therefore the e-cat activity was increased by 10.2 wt. %.

Keywords: FCCU, regenerator, afterburning, e-cat, cyclones, revamping.

Fluid Catalytic Cracking Unit (FCCU) is one of the most important catalytic processes in the refinery that converts heavy hydrocarbon fractions into more valuable products. The FCCU design consists of a reactor and a regenerator interconnected to transfer the spent and regenerated catalyst between this equipment. In the reactor (riser), the feedstock (blends

of gas oils and residue) is catalytically cracked at temperatures of 510–540 °C, to the following products: dry gas, propane, propylene, C₄, gasoline, light cycle oil (LCO, hydrotreated downstream to produce diesel), heavy cycle oil (HCO, directed for processing to delayed coker unit) and coke. After stripping residual hydrocarbons with steam, the spent catalyst is directed to the regenerator, where the coke is burned off with hot air at 680–710 °C. The regenerated catalyst is then circulated to the riser and contacted with the preheated feedstock [1–3]. Taking into consideration the key role that FCCU has is mandatory for the refinery engineers to assure a successful operation of the reaction-regenerator section. One of the issues affecting the reliability and efficiency of the industrial unit is the regenerator afterburning.

Correspondence: D. Cursaru, Department of Petroleum Refining Engineering and Environmental Protection, Petroleum-Gas University of Ploiesti, 39 Bucharest Boulevard, 100680, Ploiesti, Romania.

E-mail: dianapetre@upg-ploiesti.ro

Paper received: 30 April, 2021

Paper revised: 12 June, 2021

Paper accepted: 27 June, 2021

<https://doi.org/10.2298/CICEQ210430023E>

The FCCU afterburning is caused by incomplete burning of coke carbon in the regenerator dense phase. Consequently, the combustion of CO to CO₂ can occur in the dilute or gas phase, leading to increased temperatures in the corresponding regenerator area. This situation happens because the heat released from the CO combustion is about three times higher than the heat released from the carbon-to-CO combustion. This combustion must occur in the dense catalyst bed. Without the catalyst bed to absorb this heat of combustion, the temperature increases rapidly in the dilute phase and flue gas system [4,5].

Severe afterburning can damage the regenerator internals (as cyclones and plenum chamber) and contribute to catalyst thermal deactivation [3,5-7]. Many FCC units operate with a limited degree of afterburning, as long as the dilute and gas-phase temperatures do not exceed the metallurgical limit of the regenerator internals [5,7]. Of course, when the regenerator temperatures reach the maximum design limits of the equipment, it is mandatory to take the necessary measures for a safe operation. The level of the afterburning phenomenon depends on the unit's operating conditions and the regenerator design, which influences the effectiveness of the contact between the combustion air and the spent catalyst.

Operating solutions for afterburning control

The operating options recommended in the technical literature for reducing the afterburning are the following:

Usage of Pt-CO promoter. Pt-CO promoter is added to accelerate the CO combustion in the regenerator's dense phase and minimize the higher temperature excursions because of afterburning in the dilute phase and across cyclones [1-9].

Increasing the dense bed temperatures to speed up the rate of CO burning in the bed. This can be achieved by maximizing feed preheat temperature, increasing the catalyst activity, increasing the dense bed level and regenerator pressure [4,5,7,10].

Optimizing the catalyst stripping steam rate. If the stripper operation is not optimized, un-stripped hydrocarbon can enter the regenerator and burn in the dilute phase generating high temperatures/afterburning [4,5].

Optimizing the flue gas excess oxygen to assure enough oxygen for complete combustion of coke at CO₂ [2,4,11].

Regenerator hardware that influences the afterburning

The regenerator design and mechanical integrity of the internals are critical in achieving low afterburning [4,5,7,10,12]:

The air distribution. It is essential to assure a uniform distribution of air through the regenerator. Any failure of the air grid can create a poor area air distribution and consequently can increase afterburning and CRC (carbon on the regenerated catalyst).

The spent catalyst distribution. The spent catalyst should be distributed as evenly as possible across the catalyst bed.

Regenerator design. The most well-known FCC unit is the bubbling bed regenerator, and in this design, the catalyst enters the top of the bed and leaves at the bottom in countercurrent flow to air. Usually, this type of FCCU is associated with different degrees of afterburning, but this issue was resolved with the introduction of Pt-CO promoters in the 1970s. Other designs, such as the Exxon Flexicracker, introduce the spent catalyst at the bottom of the bed with a catalyst overflow well in concurrent flow [5].

UOP introduces the high-efficiency combustor regenerator to minimize the afterburning, which is designed to burn the coke to CO₂ without CO promoter completely and with low excess oxygen [13]. Another advantage of this design is that the NO_x emissions are reduced. Improving spent catalyst distribution and adding horizontal baffles in the dense bed of the regenerator are effective measures that can be implemented to minimize the afterburning [14-16]. With the rapid development of computer technologies, computational fluid dynamics (CFD) simulation has gradually become an important tool available to the refineries to evaluate the regenerator's catalyst and air distribution [14,15,17].

This study was conducted over 1000 days to assure the time needed for monitoring and evaluating a commercial FCC Unit during regular operation. The FCCU has been experiencing the afterburning since changing the operation mode from partial burn to entire burn operation. To control the afterburning, Pt-CO promoter was dosed, but even in this situation, the afterburning remains at high rates up to 113 °C. The high-temperature operation led to regenerator cyclones and plenum chamber failure and consequently to an emergency shutdown of the unit. Also, it was considered that operating the regenerator at high temperatures affected the e-cat activity because of thermal deactivation. Therefore, the refinery needs to analyze and implement the necessary measures to reduce the afterburning and improve the FCCU operation.

MATERIALS AND METHODS

Materials

The FCCU process a heavy, non-hydrotreated

feedstock (density = 914 - 945 kg/m³, KUOP = 11.5 - 11.8) with high contaminant content (S = 1.0 - 2.2 wt.%, N = 1400 - 1900 wt. ppm). The FCCU feedstock is a mixture of around 90 wt.% vacuum gas oil (VGO) and 10 wt.% heavy coker gas oil (HCGO).

FCC Unit

The FCC Unit is a UOP side-by-side configuration with a bubbling bed regenerator and was first commissioned in 1980. The design capacity of the FCCU is 1,000,000 t/year. Initially, the FCCU was designed to operate in the partial burn, but later, the operation mode was converted to complete burn based on an engineering revamp project. The revamping involved implementing a new air grid and a new spent catalyst distributor.

FCCU catalyst and additives

During the study, the same type of commercial FCC fresh catalyst was dosed with Pt-CO promoter to assure 1.6 wt. ppm platinum on equilibrium catalyst (e-cat). The FCCU inventory is 200 tons e-cat.

FCCU afterburning

The afterburning was evaluated based on the temperature differences between the dense, dilute, and gas phases. The regenerator temperatures were measured using 12 Emerson thermocouples type K (four thermocouples were designated to register each regeneration phase's temperature: dense bed, dilute phase, and gas phase).

RESULTS AND DISCUSSION

Afterburning evaluation

During the FCCU operation, there were recorded high-temperature differences up to 97 °C between dense and dilute phases and 113 °C between dense phase and flue gas temperature (Figure 1a).

Different temperatures were seen between the regenerator's phases and on the same elevation level (the same phase) but other areas/quadrants. Therefore, by plotting the temperature profile on each phase, it was noticed that the temperatures registered by the four thermocouples were similar only in the dense phase (Figure 1b). In the dense and gas phases, the temperatures were higher in the regenerator area where the spent catalyst inlet and regenerated catalyst outlet lines are located (Figures 1b and c).

A better view of the temperature profile was achieved by correlating each temperature value with the location of the thermocouples on the regenerator (lateral and top view - as presented in Figure 2). The regenerator temperature profile was plotted based on the average values registered on the 143d operation

day since, in this period, the FCCU was operated in severe afterburning conditions that eventually led to the unit emergency shut-down.

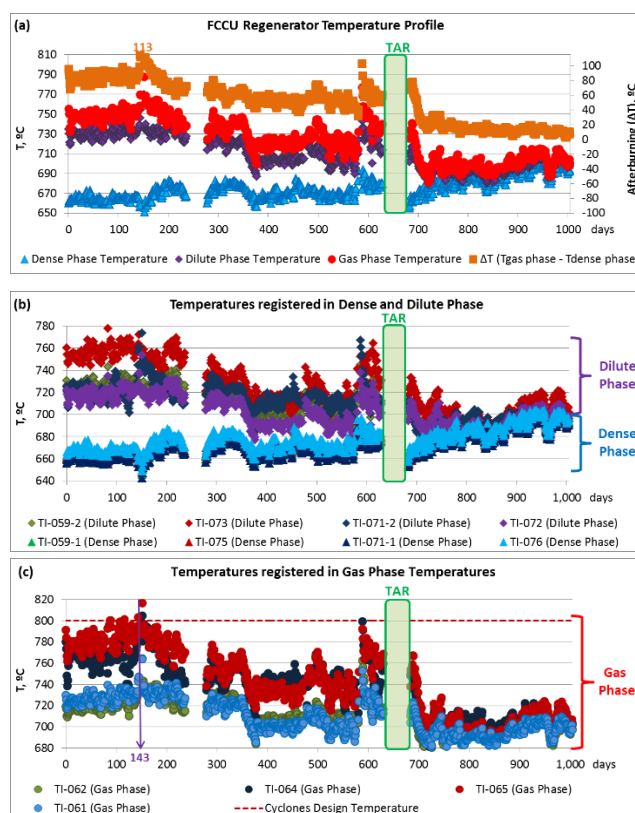


Figure 1. FCCU regenerator temperature profile: a. Average temperatures in dense, dilute, and gas phases; b. Temperatures registered by thermocouples in dense and dilute phases; c. Temperatures registered by thermocouples in the gas phase.

The data showed a 145 °C gap between the temperature registered in the dense phase by TI-075 (658 °C) and the flue gas at the 2nd stage cyclone outlet by TI-065 (803 °C). The 145 °C temperature difference demonstrated that the coke is not entirely burned. CO is formed in the dense bed that eventually is burned at CO₂ in the dilute and gas phases generating higher temperatures.

Afterburning effects

Regenerator internals metallurgy failure

Excessive afterburning is reported to cause significant mechanical damage to the regenerator internals [7,18]. The regenerator cyclones have a typical 15-30 years life depending on the erosion and mechanical fatigue. The base metal of cyclones will deteriorate with time leading to graphitization. Once this happens, the metal cannot be welded upon and repaired during a normal unit turnaround (TAR) [5]. High temperatures along with erosion and longtime

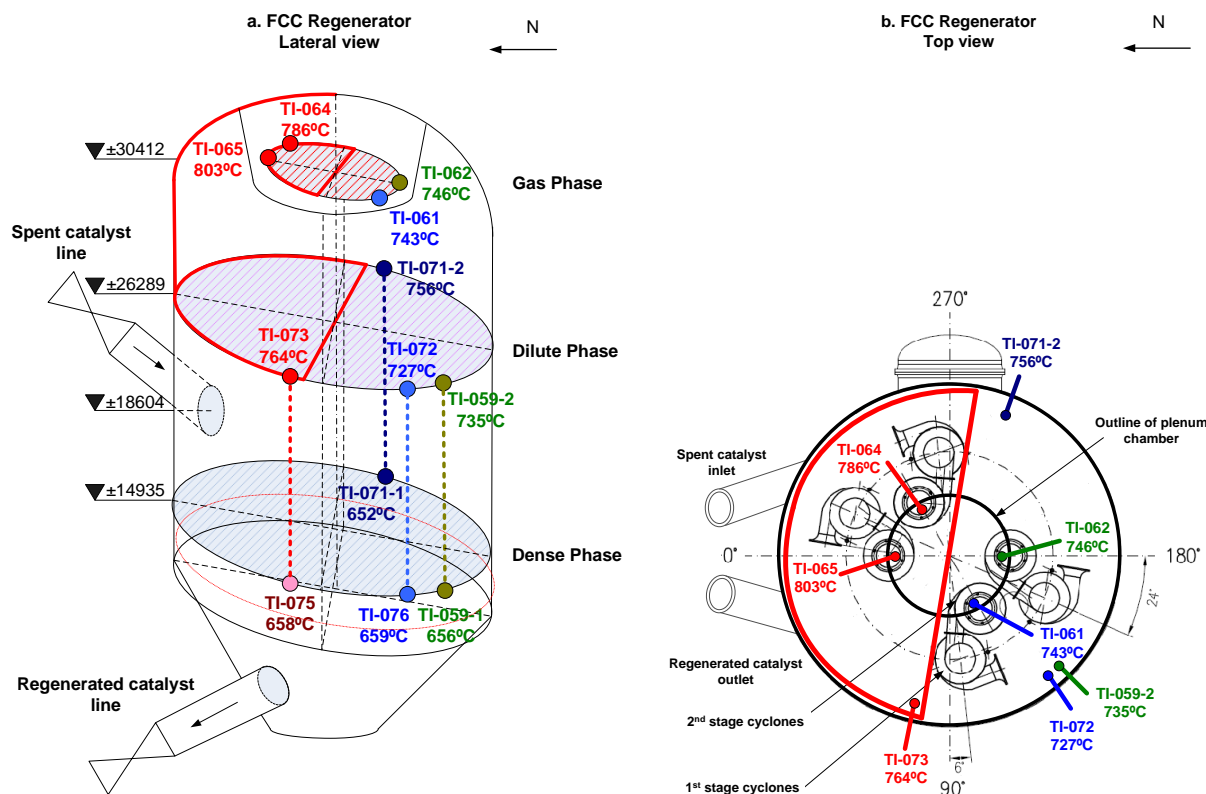


Figure 2. Temperatures registered by the regenerator's thermocouples on operation day no. 143: a. Regenerator lateral view - temperatures in dense, dilute, and gas phases; b. Regenerator top view - temperatures in dilute and gas phase.

operation for 21 years deteriorated the ASTM 304 type metallurgy of the internals and led to the following failures:

Cracks and holes in the 2nd stage cyclones: the unit experienced dipleg detachment from the cone of the cyclone at their welds which eventually led to unit emergency shut-down.

Cyclones and plenum chamber bodies' distortion and deformation due to stresses imposed by thermal gradients exacerbated by the afterburning.

The main reason for equipment failure is that the temperatures at the outlet of the 2nd stage cyclone (located near the spent catalyst inlet and regenerated catalyst outlet) exceeded the metallurgical design temperature, which is 800 °C for cyclones and plenum chamber. The data showed that during the 87-151 operation days, the gas phase temperatures (daily averages) were around 800 °C and increased to 817 °C on the 151st day (Figure 1 c). Also, it was seen that the highest operating temperatures were registered by the thermocouples TI-075, TI-073, and TI-065 that are located on the regenerator side near the spent catalyst inlet and regenerated catalyst outlet (Figure 2).

Due to the repeated mechanical failures of regenerator cyclones, the FCCU experienced six emergency shut-downs during 600 days of the

operation (until the regenerator revamping).

E-cat thermal deactivation

The high catalyst deactivation rates in the units with a high afterburning were attributed to higher dilute phase temperatures [5,8,11]. Operating the regenerator up to 800 °C during the first 180 days of industrial evaluation led to the reduction of the e-cat activity at around 61.7 wt.% with a minimum registered activity of 56.6 wt.% (Figure 3). Once the afterburning was eliminated, and the regenerator was operated at a maximum of 725 °C (after TAR), the e-cat activity increased to 71.9 wt.% (+10.2 wt.%) even if the fresh catalyst dosage rate was maintained at a minimum of 0.52 kg/ton feed. The operating temperatures of the regenerator and the fresh catalyst addition rate influenced the e-cat deactivation rate. The fresh catalyst addition rate was adapted to balance the e-cat losses caused by the cyclone failure and maintain the catalyst level in the regenerator. Discontinuous fresh catalyst dosages between 0.52 and 14.33 kg fresh catalyst/ton feed are also the reason for achieving different e-cat activities in the range of 56.5-76 wt.%. However, high temperatures operation (up to ~800 °C) led to rapid deactivation of the e-cat (Figure 3 - before TAR).

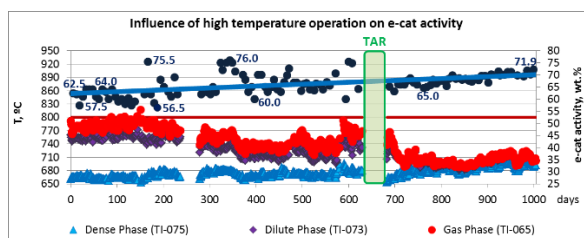


Figure 3. Influence of high-temperature operation on e-cat activity.

Carbon on regenerated catalyst

Carbon on the regenerated catalyst (CRC) registered during afterburning was between 0.1–0.38 wt.% (an average of 0.18 wt.%), higher than expected for a complete burn operation. After removing the afterburning, the CRC was reduced at 0.03 wt.%.

The inefficient coke burning due to non-uniform mixing of air and spent catalyst led to an increased CRC (Figure 4). The deposition of carbon on the catalyst temporarily blocks some of the catalytic sites, this being another factor that negatively influenced the catalyst activity.

Increasing of CRC in FCC units that are operating in afterburning conditions was also reported in other studies: one refinery reported an increase of afterburning and consequently of CRC from 0.05–0.10 wt.% to 0.15–0.2 wt.% because of the spent catalyst distributor failure and in another refinery case it was reported an increase in CRC up to 0.19 wt.% caused by air distributor failure [5].

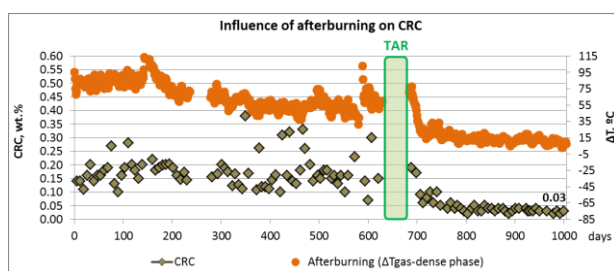


Figure 4. Increasing of CRC due to non-uniform mixing of air and catalyst.

Massive e-cat fines losses

Due to poor cyclone performances, all 0–40 μ e-cat fines from the regenerator were lost, as reported by others [6]. Loss of fines led to average particle size (APS) increase up to 110 μ . The coarse catalyst with no fines causes the formation of larger air bubbles and poor contact between air and catalyst. Low air and catalyst contact affected the complete burning of the coke in the catalyst bed and therefore increased the afterburning.

Replacing the old ineffective cyclones with new

ones, it was seen better retention of e-cat in the FCCU regenerator that led to an increase of 0–40 μ fines up to around 11.7 wt.% and consequently to a decrease of the APS from 110 μ to 85 μ . Better e-cat quality improved the FCCU operation and reduced the afterburning.

Afterburning Root Cause Analysis

Cyclones condition

Long time operation and high temperatures affected the integrity and, therefore, the performances of the cyclones. As a result, the cyclones have lost their capacity to retain the 0–40 μ e-cat fines in the regenerator. Lack of fines, low fluidization characteristics, and low e-cat activity are factors that increased the afterburning and enhanced the thermal deactivation of the e-cat. Another factor that influenced the unit operation was the existing design of the regenerator: The original design was for six pairs of cyclones, but only four sets of cyclones were installed during the construction phase of the FCC Unit. Two of the six plenum cyclones support nozzles were blanked and seal welded (Figure 5). It was concluded by analyzing the cyclones layout that the space created by the absence of the two pairs of cyclones affected the distribution of gas flow in the dilute phase and led to higher temperatures in the cyclones located on the spent cat inlet/regenerated cat outlet side. Based on the observations on the status and positioning of cyclones, it was proposed to replace the old cyclones and assure a symmetrical layout with a 90° orientation. This solution required a new top head and a new plenum chamber to suspend new cyclones.

Air Grid Evaluation

High afterburning/temperatures recorded in the area with the inlet spent catalyst suggested insufficient air to burn the carbon completely in a dense bed. Since other FCC units experienced high afterburning because of the air distributor failure [4,5], evaluating the air grid status was considered. Upon inspection, it was concluded the following:

There was no erosion of the jets, and the refractory lining was in good condition and intact. The air grid jet pattern assured an even air distribution to all quadrants of the regenerator.

To address the non-uniform carbon distribution in the regenerator, it was proposed to revise the jets plugging pattern of the air grid to direct more air to the spent catalyst inlet area (Quadrant I) and less air to the other regions of the regenerator. The proposed air grid plugging uses the same total number of plugged jets as the current air grid layout

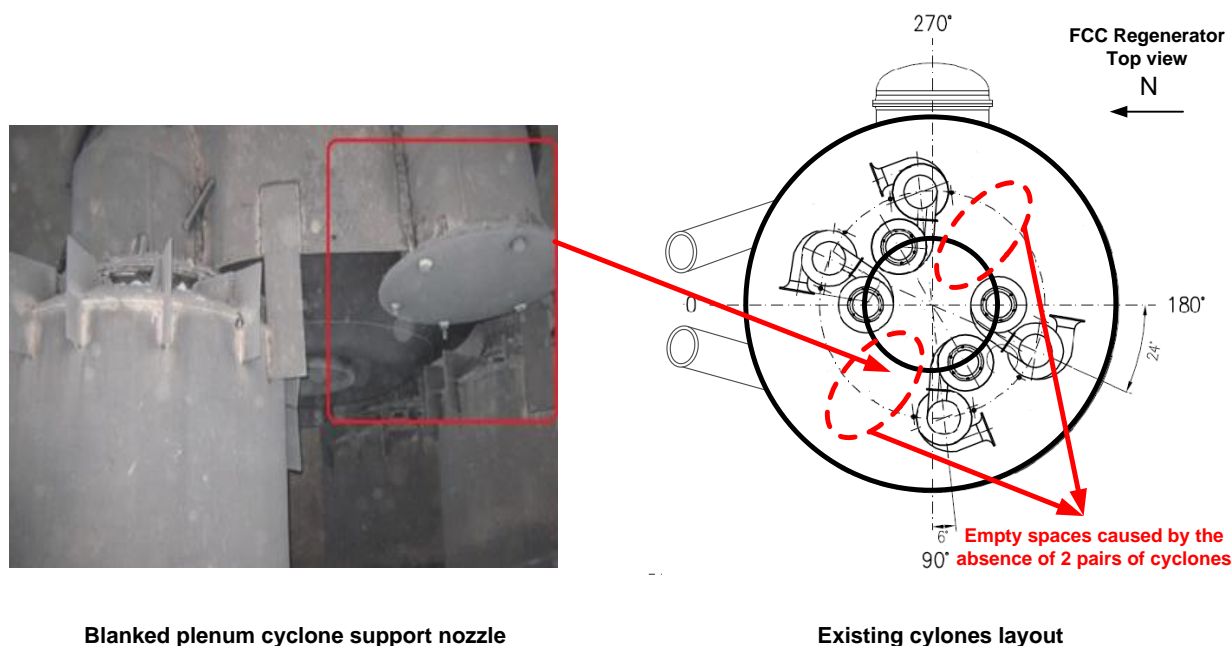


Figure 5. Non-symmetrical regenerator cyclones layout.

to ensure no impact on the air blower performances. It uses all open jets in the incoming spent catalyst quadrant, 29% of the total volume of air discharged by the air blower. However, since operating the regenerator with a 4 vol.% excess oxygen in flue gas did not improve the afterburning, it was considered that the CO breakthrough in the spent cat inlet area is also caused by other factors besides the air grid design. Therefore, the refinery postpones the revision of the air grid jets plugging pattern until the results achieved by cyclones replacement are evaluated.

Spent Catalyst Distribution

As presented, the refinery implemented a new spent catalyst distributor “ski jump” type during the FCCU revamping for a complete burn operation. The purpose of the distributor is to divert the spent catalyst away from the regenerator wall toward the center of the regenerator. Since the most severe afterburning was recorded in the cyclone pairs located on spent cat inlet/regenerated cat outlet there were evaluated the following hypothesis:

The catalyst is short-circuiting from the spent catalyst inlet to the regenerated cat outlet. Coke burning is higher on this side, leading to increased CO breakthrough and higher temperatures.

The spent catalyst outlet distributes the spent catalyst above the bed and close to the wall. This leads to the un-stripped hydrocarbon burning in the dilute phase and the slight movement of the catalyst to the side opposite the inlet.

Considering these assumptions, the idea of removing the catalyst distributor and extending the

spent cat pipe to submerge it into the catalyst bed was analyzed. This design will help discharge the catalyst further away from the wall and vessel entry point. Also, this modification would enable the un-stripped hydrocarbon to burn into the dense bed and not in the dilute phase.

Because the refinery did not have sufficient industrial evidence that replacing the spent catalyst distributor with a submerged pipe into the bed dense will reduce the afterburning, it was decided to postpone the implementation of this project until it was evaluated effect achieved by replacing the cyclones.

Influence of process parameters on afterburning reduction

Implementing a new refinery investment project requires time, depending on the size, cost, and importance. In our refinery case, the project for “Replacement of the regenerator cyclones and plenum chamber” took almost two years in which have been performed the following phases: preparation of the feasibility study, headquarter approval, organization of the tender for selecting the suppliers and contractor, equipment procurement, construction execution and so on. Since the cyclones replacement is a long process, the refinery needed to analyze the operating options recommended in the technical literature to reduce the afterburning. Unfortunately, it was seen that the results achieved are affected by numerous technological constraints. Therefore, the refinery target was to select those FCC process parameters that can be optimized to control the afterburning.

Usage of Pt-CO promoter. The FCC fresh catalyst was promoted with a commercial Pt-CO promoter (equivalent to 1.6 ppm Pt on e-cat). During the previous FCCU operation, it was noticed that higher Pt concentration did not improve the afterburning. Therefore, it was concluded that the afterburning was caused by the poor catalyst and air distribution as reported by others [6]. The FCCU optimization was performed at constant Pt-CO promoter dosage to not interfere with the results achieved by process parameters modification.

Maximize the feed preheat temperature (FPHT) to speed up the rate of CO burning in the catalyst bed. This can be achieved by modifying the following parameters:

Maximize the feed preheat temperature (FPHT). Analyzing the data collected, it seems that modifying the feed temperature between 170 °C to 280 °C had a different effect than the one presented in technical literature. Higher FPHT to riser increased the dilute/gas phase temperatures, and lower FPHT decreased the temperatures on top of the regenerator. This behavior is because an increase of the FPHT will reduce the cat/oil ratio, and consequently, the regenerator temperature will rise. Because of the air and catalyst non-uniform distribution, the temperatures will increase all over the regenerator (in all the 3 phases) and not only in the catalyst bed (Figure 6a).

Increasing slurry recycling to increase the coke production. The FCCU was designed for recycling the slurry to the riser. Increasing slurry recycling will increase coke production since slurry is a heavy feed with high aromatic content. Consequently, burning a higher quantity of coke in the regenerator will increase the dense bed temperature and reduce the afterburning [4,5].

During the study, slurry recycling did not have the results expected on the regenerator temperatures profile. On the contrary, in the first part of the evaluation (days no. 1 to 150), it was seen that the gas/dilute phase temperatures were increased when the slurry flow rate was increased. Therefore, in the period where the slurry recycle flow rate was also decreased (days no. 280–400), the gas/dilute temperatures decreased. For the rest of the evaluation (days no. 400–600), the slurry recycle flowrate fluctuation cannot be correlated with regenerator temperatures profile (Figure 6b). Since the slurry recycling did not affect afterburning, it was considered that the recycling flow rate insufficient to influence the process (+/-6 m³/h), compared to the FCCU feed flowrate (90 - 130 m³/h). That is why the refinery started to evaluate if the feed flow rate processed or the FCCU loading does affect the

regenerator temperatures.

FCC Feed flowrate. The industrial data showed a direct proportionality between the feed flow rate and the dilute/gas phase temperature (Figure 6c). Moreover, the regenerator temperature pattern can be explained by the fluctuation of the FCC feed flow rates (days no. 360–380). This behavior explains that increasing the FCCU feed flow rate will generate more coke and, consequently, burn in the regenerator, leading to higher temperatures. Unfortunately, in our case, both dilute- and gas-phase temperatures increased, which suggested that the burning rate of CO to CO₂ was insufficient in the dense bed. It took place also in the dilute and gas phases. Since the air blower flow rate was monitored and controlled to maintain enough oxygen (1-5 vol.%) to assure the complete burning, it was concluded that the poor distribution of the catalyst and air was the main cause of the high temperatures in the dilute/gas phase.

The increase of the catalyst activity by increasing the catalyst dosage. A high activity e-cat increases the coke production, and more coke burned in the regenerator leading to an increase in the catalyst bed temperature [5]. Increasing the e-cat activity reduced the level of afterburning. Unfortunately, the e-cat activity could not be kept constant even in the condition of dosing higher fresh catalyst dosage rate because of the severe thermal deactivation caused by the operation at high temperatures above 730 °C (Figure 3).

Increase the regenerator pressure to increase the burning rate in the dense bed. Increasing the regenerator pressure from 1.85 to 2.13 barg reduced the temperature in the gas and dilute phases and consequently the afterburning in the 150–230 day period. The data registered in the 278–580 day period were not conclusive since these fluctuations were caused by the feed/air flowrate modification (Figure 6d).

The increase of the regenerator pressure is one of the measures recommended to reduce the afterburning [4, 5, 7]. Yet, the FCCU system pressure is affected by many other unit constraints:

The pressure drop on the main column overhead condensers increased in time (due to heat exchangers tubes plugging), and this phenomenon affects the regenerator pressure by increasing it. After cleaning the respective condensers during unit turnaround, the pressure drop on this equipment is lower, and therefore the regenerator pressure decreased.

The explanation for the high regenerator pressure differences registered before and after TAR (Figure 6.d) is that the main column overhead

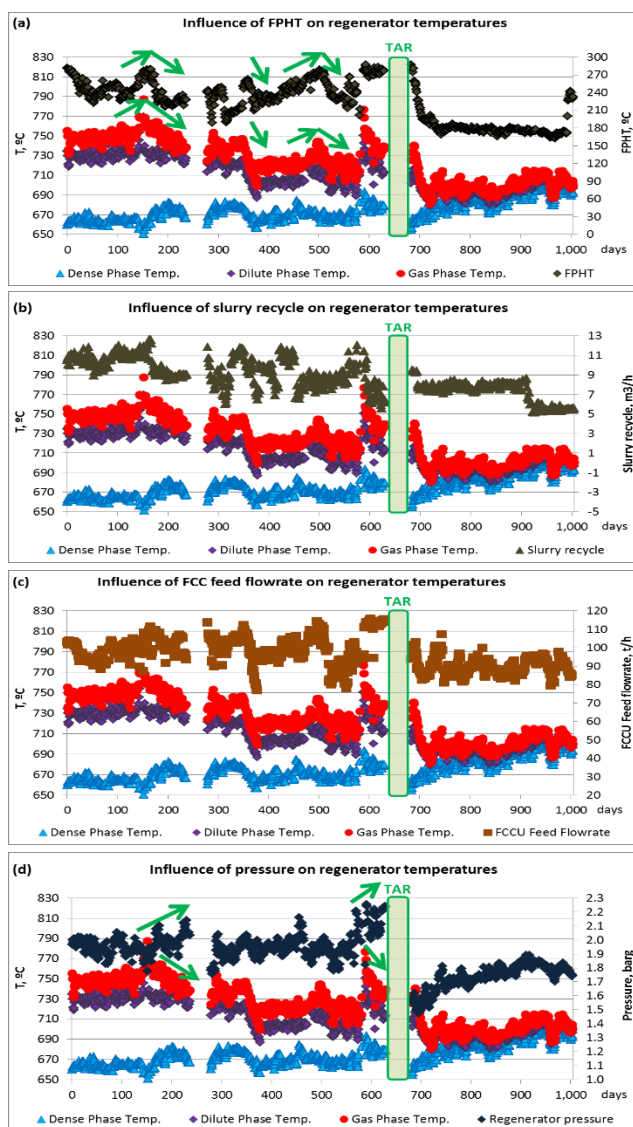


Figure 6. Influence of process parameters on regenerator temperature profile: a. Feed preheat temperature, b. Slurry recycle, c. FCC feed flow rate, d. Operating pressure.

shell & tube condensers were replaced with new, more efficient plate heat exchangers (which have reduced the pressure drops between reactor/regenerator and wet gas compressor suction).

Regenerator pressure is affected by the air flow rate operation, which depends on the FCCU feed flow rate. The FCC operator must adapt the air flow rate at the feed flow rate to ensure enough oxygen for burning the coke in the regenerator. Consequently, by increasing the air flow rate also, the regenerator pressure increased;

Higher pressure in the regenerator will increase the fines losses through cyclones.

The increase of the level of the catalyst bed provides enough gas residence time for CO burning.

As presented in other studies, a deeper bed reduces the distance from the top of the bed to the cyclone inlet, increasing the catalyst load to cyclones and causing increased catalyst losses from the regenerator [5]. Therefore, finding the optimum bed level was recommended to minimize the catalyst losses and improve the afterburning. In this study, the FCC unit was confronted with massive catalyst losses caused by cyclones failure. In these conditions, it was difficult even to maintain the constant bed level in the regenerator, and for increasing it, high catalyst dosages were needed. Monitoring the unit operation, it was concluded that by maintaining the height of bed level at 78 - 83% (Figure 7a - operation days no: 380-560), it was achieved the lowest afterburning (~ 53 °C) and lowest catalyst dosage rate needed to compensate for the e-cat losses. After the regenerator revamping (TAR), because of the efficiency of the new cyclones, the bed level increased steadily even if the catalyst addition rate was maintained at 0.52 kg/t.

Optimizing the catalyst stripping steam rate. If the stripper operation is not optimized, un-stripped hydrocarbon can enter the regenerator and burn in the dilute phase. Increasing the stripping steam flow rate with 0.8 t/h reduced the dilute phase temperatures on average by 29 °C (Figure 7.b.). One of the main industrial unit constraints regarding the stripping steam availability/distribution can be the mechanical damage of the steam nozzles or trays. Non-uniform distribution leads to steam bubbles agglomerating to larger bubbles, reducing stripping effectiveness [7]. Based on equipment inspection during TAR, it was concluded that the stripper tray orifices were plugged with coke during the unit operation. This can lead to steam maldistribution and, consequently, decrease stripper efficiency. Because of tray orifices plugging, it is expected for the stripper efficiency to be higher immediately after unit turnaround (during TAR is performed the stripper tray orifices unplugging) and to decrease in time to the next turnaround. Therefore, the effect achieved by modifying the steam rate can be different depending on the mechanical status of stripper trays.

Some FCC licensors are proposing more efficient technologies like stripper packing nowadays to improve the catalyst stripping performance and reduce steam consumption. Therefore, the stripper-packing technology was planned to be evaluated later by the refinery, the main factors for its implementation being the investment cost, the economic effect achieved by steam consumption reduction, and the effect on regenerator temperatures.

Increasing the reactor temperature. Increasing the conversion and coke yield is expected to improve the stripper performance at a fixed catalyst circulation rate as the hydrogen in the coke will decrease. Consequently, this measure will minimize the burning of light hydrocarbon products from the spent catalyst in the dilute phase. Also, higher coke production will increase the regenerator catalyst bed temperature. Usually, the FCC reaction temperature is optimized depending on the production refinery objectives (higher conversion, gasoline or diesel maximization, octane number, increasing propylene/isobutylene yields, etc.) and unit constraints (wet gas compressor capacity limit, exceeding the dry gas production over the refinery fuel gas consumption, coke burning, mechanical design consideration, reactor metallurgy design temperature, etc.). Because of the refinery objectives, the ROT (Riser Outlet Temperature) increased to 526 °C (before TAR) to optimize the gasoline yield and minimize dry gas production. Evaluating the results achieved during different operation modes (Figure 7c - Operation Mode I and II), it was concluded that operating with +4 °C higher ROT reduces the temperatures in the dilute and gas phases afterburning with around 33 °C (Table 1).

Optimizing the flue gas excess oxygen to assure complete burning of the coke. The air blower capacity is the main FCCU constraint that affects the oxygen availability needed for coke burning (Figure 7d). If there is such a situation, increasing the feed flow rate over the air blower capacity can lead to partial burning of coke to CO, and therefore, afterburning will increase. During FCCU operation, the air flow rate was controlled and adapted at the FCCU feed flow rate to have enough oxygen for coke burning and assure 1 to 5 vol.% excess oxygen in the flue gas. High afterburning up to 113 °C was recorded at maximum capacity of the air blower (72,800 Nm³/h), and an excess of O₂ in the flue gas was maintained between 2.3-3.4 vol.% (days no. 1-365). The reduction in air flow rate at 70,000 Nm³/h decreased the afterburning at 50 °C (days no. 370-570). These results were explained by air channeling that appears when the air flow rate increases, causing oxygen breakthrough on one side of the dense bed and reacting in the dilute phase with the CO escaping from another part of the reactor. Therefore, lower afterburning is achieved at lower flue gas excess oxygen between 1.2-2.5 vol.% (operation days no. 365 - 470) and not at higher values above 3 vol.% O₂ that involved the higher air flow rates.

Results achieved by optimizing the process parameters. Optimizing the FCC process decreased

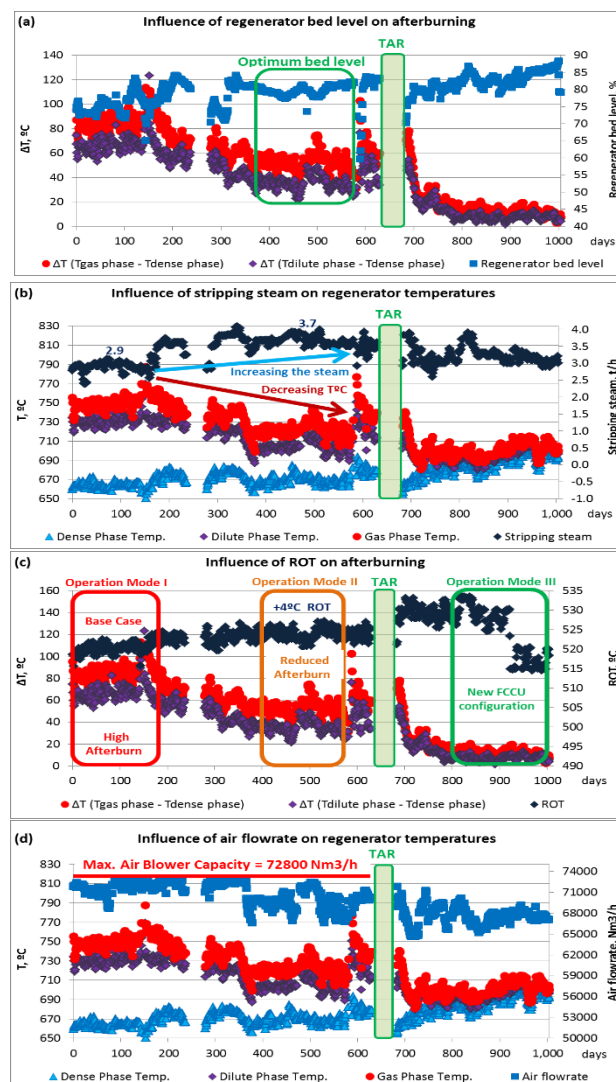


Figure 7. Influence of process parameters on regenerator temperatures: a. Regenerator bed level, b. Stripping steam, c. Riser temperature, d. Air flow rate.

the afterburning by 33 °C representing a reduction of 38% from the initial $\Delta T_{\text{gas-dense}}$ phase. For an FCCU confronted with significant constraints (Cyclones failure and non-symmetrical cyclone layout - Figure 5), it was found that afterburning was reduced by optimizing the following process parameters (Table 1):

Increasing the height of the regenerator catalyst bed level by 4%.

Increasing the catalyst stripping steam by 0.8 t/h.

Increasing the reactor temperature by 4 °C.

Increasing the e-cat activity by 4.2 wt.%.

Other parameters such as FPHT, slurry recycling, and excess O₂ in the regenerator did not significantly influence the afterburning. Regarding the air flowrate/O₂ requirement, a minimum of 1 vol.% ensured an excess of O₂ in the flue gas to burn the coke completely. Suppose the regenerator is confronted with maldistribution/channeling of air/cat-

alystat higher air flow rates between 3-5 vol.% because of channeling. In that case, the air will pass through the regenerator phases without being

available for coke burning.

FCCU revamping for addressing the afterburning. Analyzing the afterburning causes and

Table 1. Influence of FCCU process parameters on afterburning

No.	Process parameter	Unit	1	2	3
			Operation Mode I Base Case 1 - 180*	Operation Mode II FCCU Optimization 380 - 560**	Δ (2 - 1)
	Period - Days No.				
1.	Catalyst bed level	%	76	80	+4
2.	Stripping Steam	t/h	2.9	3.7	+0.8
3.	ROT	°C	520	524	+4
4.	e-cat activity	wt.%	61.7	65.9	+4.2
5.	Dense Phase	°C	665	669	+4.6
6.	Gas Phase	°C	751	722	-28
7.	Afterburning ($\Delta T_{\text{gas-dense phase}}$)	°C	86	53	-33
8.	Afterburn reduction ($\Delta T_{\text{gas-dense phase}}$) %			38	-38

* Daily average data recorded from the operation day no. 1 to 180 (Operation Mode I).; ** Daily average data recorded from the operation day no. 380 to 560 (Operation Mode II).

influence of process parameters on regenerator temperatures, it was considered that the best solution to address the afterburning is to replace the cyclones and plenum chamber and assure a symmetrical layout of the cyclones with a 90° orientation to cover the regenerator surface uniformly. This activity was performed during refinery turnaround and consisted of implementing a new set of cyclones according to the layout presented in Figure 8.

In the new regenerator configuration, a massive reduction of the afterburning was seen, demonstrating

the efficiency of new symmetrical layout cyclones (Figure 1 - afterburning after TAR). Assuring a uniform distribution and mixture of the air and catalyst has maximized the burning of the coke at CO₂ in the catalyst bed and reduced at minimum the amount of generated CO that can burn in the upper area of the regenerator. Also, the removal of air/catalyst channeling decreased temperature differences registered at each regenerator level (in the same phase), as shown in Figure 1 (regenerator temperatures/afterburning before and after TAR).

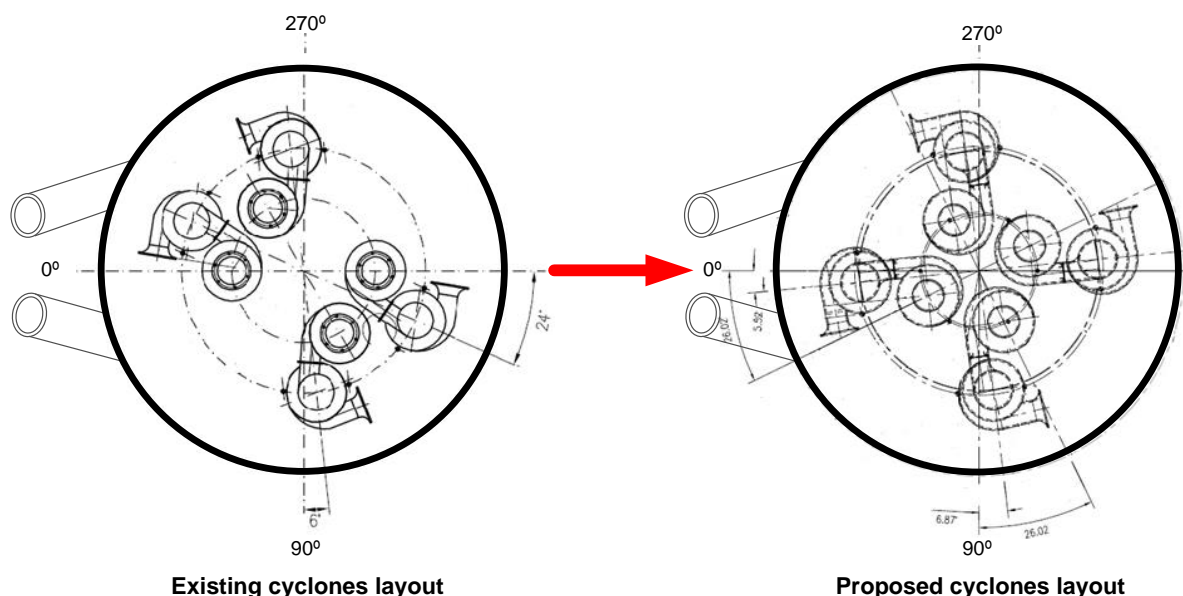


Figure 8. Replacing and assuring a symmetrical layout of the cyclones.

To evaluate the results, the average regenerator temperatures registered after TAR (Operation Mode III - operation days no. 800-1000) were compared with

the temperature profile registered during Operation Mode I and II (before TAR). As a result, the temperatures in the dense bed increased by 24 °C, in

the dilute phase decreased by 34 °C, and in the gas phase decreased by 50 °C. Therefore, the afterburning decreased by 74 °C, representing a reduction of 86% (Figure 9b).

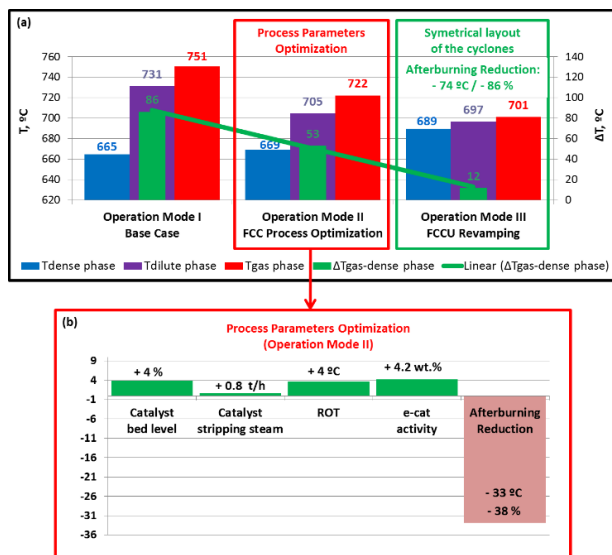


Figure 9. Afterburning reduction by FCC process optimization (a, b) and revamping (a).

In the new cyclone configuration, the FCCU operation is more stable since the afterburning is kept at a minimum and is not depending on the process parameters modification (Figures 1, 3, 4, 6, 7 - afterburning after TAR). Therefore, in these conditions, the technological process can be operated according to the economic targets of the refinery and not depending on unit constraints (Figure 7c - modification of ROT to maximize gasoline or diesel production did not influence the afterburning).

Afterburning reduction and the operation of the regenerator at lower temperatures below the internals design increased the reliability of the cyclones and plenum chamber and, therefore, their lifetime. As a result, there was no emergency FCCU shut-down reported after TAR.

From the catalytic perspective, implementing new and more performant cyclones and operating at lower regenerator temperatures/afterburning, it was positively influenced the equilibrium catalyst quality and FCCU conversion:

- Eliminated the risk of e-cat deactivation increased the e-cat activity from around 65 to 71.9 wt.% even if fresh catalyst addition rate was maintained constant at 0.52 kg/t (Figures 3).
- The new regenerator configuration assured a better burning of the coke on the catalyst, and consequently, CRC was reduced from an average of 0.18 wt.% to 0.03 wt.% (Figure 4).

Therefore, it improved the catalyst regeneration and increased the regenerated e-cat activity.

- Replacing the old and damaged cyclones with new ones reduced the e-cat fines losses and consequently increased the 0-40 μ fines into the FCCU e-cat inventory with APS reduction.

CONCLUSION

Operating the FCCU in afterburning conditions can increase the regenerator temperatures above the metallurgical design leading to mechanical failures of the cyclones and plenum chamber. Afterburning was decreased with 33 °C (38% reduction) by increasing the catalyst bed level height (+4%), catalyst stripping steam (+0.8 t/h), ROT (+4 °C), and e-cat activity (+4.2 wt.%). Other process parameters like FPHT, slurry recycling, and excess oxygen did not significantly influence afterburning because of maldistribution. The most efficient way to reduce the afterburning was to revamp the regenerator to assure a uniform layout of the cyclones. The new symmetrical cyclone arrangement decreased the afterburning by 74 °C representing an 86% reduction. Consequently, the regenerator temperatures decreased at around 701 °C, below the 800 °C internals design temperature, which is considered to increase the reliability and lifetime of the cyclones and plenum chamber. Eliminating the risk of catalyst thermal deactivation increased the e-cat activity from 61.7 wt.% to 71.9 wt.%. The uniform distribution/mixing of air and catalyst provided a better regeneration of spent e-cat, demonstrated by reducing CRC from 0.18 wt.% to 0.03 wt.%, and increasing the 0 - 40 μ fines retention in regenerator to 11.7 wt.%.

REFERENCES

- P. Bai, U.J. Etim, Z. Yan, S. Mintova, Z. Zhang, Z. Zhong, X. Gao, *Catal. Rev.* 61 (2018) 335 - 405.
- G.J. García, R.A. López, R.M. Yescas, *Fuel* 90 (2011) 3531 - 6541.
- M. Clough, J.C. Popea, L. Tan, X. Lin, V. Komvokis, S. S. Pan, B. Yilmaz, *Microporous Mesoporous Mater.* 254 (2017) 45 - 58.
- R. Sadeghbeigi, *Fluid Catalytic Cracking Handbook* (Third Edition), Elsevier Inc, Oxford (2012), 117 - 262.
- J.A. Sexton, in *Advances in Fluid Catalytic Cracking: testing, characterization and environmental regulations*, M.L. Occelli, CRC Press, Boca Raton (2010) 271 - 289.
- R. Fletcher, M. Evans, *Intercat* (Johnson Matthey), *Revamps PTQ* (2010) 3 - 15. https://cdn.digitalrefining.com/data/digital_magazines/file/1420275728.pdf [accessed 25 May 2021].
- J.R. Wilcox, in *Advances in Fluid Catalytic Cracking: testing, characterization and environmental regulations*, M.L. Occelli,

- CRC Press, Boca Raton (2010) 101 - 118.
- [8] A.W. Chester, in Fluid Catalytic Cracking VII - Materials, Methods and Process Innovations; Studies in Surface Science and Catalysis, Vol. 166, M.L. Occelli, Elsevier, Amsterdam (2007) 67 - 77.
- [9] G. Davison, Guide to Fluid Catalytic Cracking, Part Two, W.R. Grace & Co.-Conn, J.W. Boorman Co. Baltimore, Maryland (1996) 155-156.
- [10] G. Davison, Guide to Fluid Catalytic Cracking, Part Three, W.R. Grace & Co.-Conn, J.W. Boorman Co. Baltimore, Maryland (1999) 255-284.
- [11] J. W. Wilson, FCC Regenerator Afterburn Causes and Cures, Wilson P.E., Barns and Click, Inc., AFPM Annual Meeting (2003) AM-03-44.
- [12] R. Butterfield, T. Ventham, P. Diddams, M. Evans, Hydrocarbon Engineering 22 (2017) 55-60.
- [13] F. Rosser, M. Schnaith, P.W. Walker, Integrated View to Understanding the FCC NO_x Puzzle, AIChE Symposium, Austin, Texas (2004).
- [14] Z. Yang, Y. Zhang, T. Liu, O. Adefarati, Chemical Engineering Journal 421 (2021) 129694.
- [15] Z. Yang, Y. Zhang, O. Adefarati, J. Yue, Chemical Engineering Journal 412 (2021) 128634.
- [16] Y. Zhang, Baffles and Aids to Fluidization (Chapter 18), Essentials of Fluidization Technology, G. John, B. Xiaotao, E. Naoko (eds.). Wiley-VCH (2020) 431-455.
- [17] R. Fletcher, S. Clark, P. Blaser, Identifying the Root Cause of Afterburn in Fluidized Catalytic Crackers. AFPM Annual Meeting (2016) AM-16-15.
- [18] Y.M. Chen, Evolution of FCC - Past Present and Future and The Challenges of Operating a High Temperature CFB System, 10th International Conference on Circulating Fluidized Beds and Fluidization Technology - CFB-10, T. Knowlton, PSRI Eds., ECI Symposium Series (2013).

FLORIN ENACHE ^{1,2}
 DAN DĂNULESCU ¹
 ION BOLOCAN ²
 DIANA CURSARU ²

¹ Petrotel-Lukoil Refinery, 235
 Mihai Bravu Street, 100410, Ploiesti,
 Romania

² Department of Petroleum Refining
 Engineering and Environmental
 Protection, Petroleum-Gas
 University of Ploiesti, 39 Bucharest
 Boulevard, 100680, Ploiesti,
 Romania

NAUČNI RAD

SMANJENJE NAKNADNOG SAGOREVANJA U POSTROJENJU ZA FLUIDNI KATALITIČKI KREKING OPTIMIZACIJOM PROCESA I REKONSTRUKCIJOM REGENERATORA

Rad postrojenja za fluidni katalitički kreking u uslovima naknadnog sagorevanja može povećati temperature regeneratora iznad projektovanih, što dovodi do mehaničkih kvarova ciklona i plenumske komore. Ovaj rad predstavlja metodologiju primenjenu za istraživanje naknadnog sagorevanja u komercijalnom postrojenju za fluidni katalitički kreking i tehnička rešenja koja se mogu primeniti za smanjenje naknadnog sagorevanja. Dakle, procenom temperaturnog profila regeneratora, konstrukcije regeneratora, kao i mehaničkog statusa unutrašnjosti, zaključeno je da je glavni uzrok naknadnog sagorevanja neravnomerna distribucija i mešanje vazduha i katalizatora. Industrijski rezultati su pokazali da optimizacija nivoa sloja katalizatora, parni striping, reakcione temperature i aktivnosti ravnotežnog katalizatora smanjuju naknadno sagorevanje za 39%. Drugi parametri procesa, kao što su temperatura predgrevanja napojnog materijala, reciklaža suspenzije i višak kiseonika, nisu značajno uticali na naknadno sagorevanje zbog neispravne distribucije vazduha i katalizatora. Rekonstrukcijom regeneratora, kojom su cikloni simetričnospoređeni, smanjeno je naknadno sagorevanje za 86%, povećano zadržavanje finih čestica u postrojenju i poboljšana regeneracija istrošenog ravnotežnog katalizatora. Smanjenje radne temperature na oko 701°C otklonilo je rizik od termičke deaktivacije katalizatora, pa je stoga aktivnost ravnotežnog katalizatora povećana za 10,2 tež. %.

Ključne reči: postrojenje za fluidni katalitički kreking, regeneratorski, naknadno sagorevanje, ravnotežni katalizator, cikloni, rekonstrukcija.

SREEPRIYA SREEKUMAR ^{1,2}
APARNA KALLINGAL ¹
VINILA MUNDAKKAL
LAKSHMANAN ^{1,2}

¹ Department of Chemical Engineering, National Institute of Technology, NIT Campus P.O.673601 Calicut, India

² Department of Applied Electronics and Instrumentation, Adi Shankara Institute of Engineering and Technology, Kalady, India

SCIENTIFIC PAPER

UDC 544.6:661.833

pH CONTROL IN SODIUM CHLORATE CELL FOR ENERGY EFFICIENCY USING PSO-FOPID CONTROLLER

Article Highlights

- FOPID pH controller for energy efficiency in Sodium chlorate process
- Flexible, less time of computation, less parameter adjustment
- Can be utilized in the future for optimization of pH in sodium chlorate cell

Abstract

Industrial sodium chlorate production is a highly energy-intensive electrochemical process. If the pH of the chlorate cell is not controlled, the current efficiency drops from 99% to as low as 66.66%. Hence control of chlorate cell pH is very significant for energy-efficient sodium chlorate production. This study puts forward a fractional order PID controller for controlling the pH of the sodium chlorate cell. The tuning of FOPID controller variables is affected by employing particle swarm optimization. The highlight of the controller is that it is flexible, easy to deploy, and the time of computation is significantly low as few parameters are needed to be adjusted in PSO. The performance analysis of the suggested FOPID-PSO controller was studied and compared with the traditional PI controller and PID controller using time-domain provisions like settling time, rise time and peak overshoot and error indicators like integral square error (ISE), integral absolute error (IAE), and integral time absolute error (ITAE). FOPID controller employing PSO proved to perform well compared to conventional controllers with 0.5 s settling time and 0.1 s rise time. Thus, the FOPID-PSO controller has better setpoint tracking, which is essential for the process under consideration.

Keywords: fractional order PID controller, sodium chlorate process, particle swarm optimization, pH control.

Industrial manufacturing of sodium chlorate is one of the fastest-growing and highly energy-intensive processes, where power consumption accounts for over 70% of the production costs. The growth of the sodium chlorate industry is promising since it is globally used to manufacture chlorine-based bleaching agents and perchlorates (used as rocket oxidizers), besides its use in agricultural applications and milling applications. Hence, there have been constant efforts to improve sodium chlorate production

in terms of quantity and quality.

Industrial sodium chlorate production from hot acidulated brine involves an electrochemical process in an undivided electrochemical cell [1]. Hydrogen and chlorine are liberated at the cathode and anode, respectively. Hydrogen bubbles and chlorine dissolves in the bulk solution, giving hypochlorous acid. This weak acid disintegrates into hypochlorite ions, also known as active chlorine. The transformation of active chlorine to chlorate in the bulk involves intermediate reactions. The kinetics of this reaction depends on the pH and local concentration of active chlorine [1]. If pH is not controlled, secondary parallel reactions occur in the cell, leading to a significant loss in the current efficiency [2–5]. Hence, it is essential to control the pH of the cell bulk to improve the current efficiency and power consumption. Several approaches have been employed to improve cell efficiencies, such as using different cell

Correspondence: A. Kallingal, Department of Chemical Engineering, National Institute of Technology, NIT Campus P.O.673601 Calicut, India.
E-mail: aparnak@nitc.ac.in
Paper received: 11 September, 2020.
Paper revised: 22 April, 2021.
Paper accepted: 1 July, 2021.

<https://doi.org/10.2298/CICEQ200911031S>

designs, selecting anode, and cathodes, adding sodium dichromate, etc. [2,6-9]. So far, to our knowledge, no studies have been reported on improving cell efficiency by controlling the pH of the chlorate cell. This work utilizes a PSO-based fractional order PID controller to maintain the cell bulk pH, promote auto-oxidation reaction, and improve energy efficiency.

Fractional order calculus and fractional order control have a comprehensive prospectus in science and engineering due to well-developed and well-explained theory and the drastic development of computing facilities. Fractional calculus is an extended version of integer-order calculus. It deals with integral and differential operators having fractional order. Recently fractional calculus has been widely used as many real-world systems exhibit a memory effect best described using fractional-order dynamics. Many interests are shown in designing controllers for such fractional-order systems [10]. Various kinds of literature can be seen in the field of fractional control in the last decade by its suppleness to meet the needs of control applications. Many recent works of literature demonstrate that fractional-order controllers outperform their integer-order counterparts for many real-life engineering applications.

Among the real-world industrial controllers, 99% are PID (Proportional Integral Derivative) controllers. It owes its popularity to the simplicity of design, easy tuning procedures, and ease of use for the layman. Hence there has been continuous research on improving the robustness and performance of the PID controller. Fractional order PID controllers can be enhanced with non-integer integration and derivation parts. Podlubny [11] has described the fractional order PID controller as an extended version of a conventional PID controller from point to the plane. The proposed $P I^\lambda D^\mu$ controller, where λ and μ have non-integer values giving more flexibility in controller design as well as better performance of controller compared to conventional PID controller. Recently, Puchalski *et al.* [12] have proposed a fuzzy fractional order PID controller to control the average thermal power of a nuclear reactor. In this work, the performance indices, like ISE, IAE, ITAE of the FMR FOPID, are compared with FOPID and conventional PID controller for robustness and smooth control signal. Rajesh [13] developed a FOPID controller for a single conical tank, a classical nonlinear problem. It proves the advantage of FOPID over conventional controllers in terms of better setpoint tracking and a smoother control signal for a nonlinear system. Tong *et al.* [14] proposed a state transition algorithm to address the optimization challenges in the design of

the FOPID controller for the pH neutralization process. Recent literature shows a wide application of the fractional PID controller for various engineering fields [15-23]. All these prove undoubtedly that the FOPID controller is superior to its integer counterparts in terms of performance. Moreover, the flexibility to handle uncertainties and sudden changes in the control signal makes the FOPID concept a part of a more advanced control strategy [15,16,24-29].

The design and tuning procedures of the FOPID controller are complex compared to the conventional PID controller as two additional design parameters are involved. However, it is evident from recent literature that using an optimization algorithm is a perfect solution for the design problem [17,18,27,31-38]. Even though there have been many bioinspired algorithms, particle swarm optimization (PSO) algorithms are widely used because of their simplicity, flexibility for modification, and a smaller number of parameters for adjustment. PSO algorithm mimics the natural social behavior of a school of fish or swarm of birds or insects searching for food or location for migration. The individual learning of each team member is communicated with other members, and if anyone member finds food or location, then others in the team will follow the path quickly. This phenomenon is used for finding the optimum position for the particle. In this study, the design parameters of the FOPID controller are optimized by utilizing PSO. To tune the design variables of the FOPID controller, the performance indicator chosen is a weighted sum of integral square error (ISE), Integral absolute error (IAE), and Integral Time Absolute Error (ITAE). In addition, the time-domain variables, like settling time, rise time, and peak overshoot, are compared with those of conventional PI and PID controllers based on PSO to evaluate the performance of the proposed controller. The highlight of this proposed PSO-based FOPID controller is its flexibility and ease of implementation. This study can help implement online controllers for the industrial sodium chlorate process. Furthermore, it will lead to cost-effective and energy-efficient sodium chlorate technology development by improving cell efficiency and minimizing production costs.

The rest of this paper is framed in the following manner. In Section 2, the industrial sodium chlorate production process and the significance of pH for it are briefly explained. In Section 3, the Fractional PID controller is described. Section 4 elaborates on the PSO optimization. In Section 5, the tuning of the FOPID controller utilizing the PSO algorithm and the performances of PI, PID, and FOPID controllers are compared. Finally, in Section 6, the results are evaluated, and conclusions are drawn.

Industrial sodium chlorate manufacturing process

The industrial sodium chlorate process is an electrochemical process that involves high energy consumption. The global production rate of sodium chlorate is 3.6 million tons annually [39]. It is estimated that 5000-6000 kWh energy is required to produce a ton of sodium chlorate crystal [40]. This power consumption amounts to over 70% of the production costs. Hence, any means for improving efficiency will be beneficial from the economic and environmental points of view. The industrial process flow is given in figure 1. This paper focuses on controlling the process taking place in the electrochemical cell. As per the equation, sodium chlorate is produced by electrolyzing hot acidulated brine [39]. The overall reaction is given by equation (1) [39].

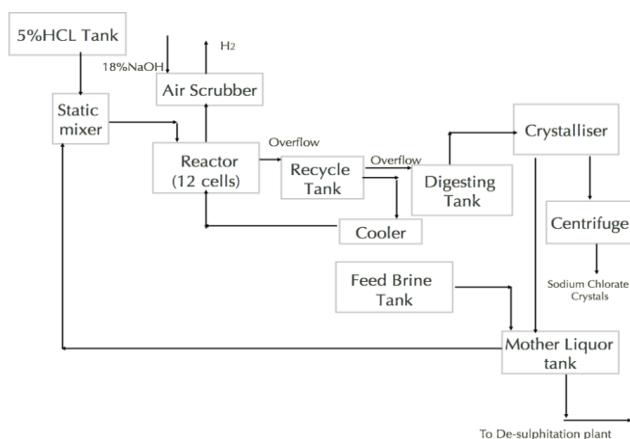
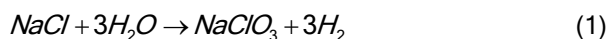
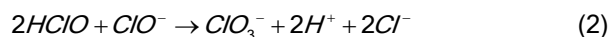


Figure 1. Block schematic of industrial sodium chlorate production plant.

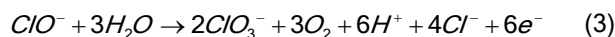
The quantity and quality of the final product depend on various conditions prevailing in the electrochemical cell, especially the pH of the electrolyte bulk. Various studies on these aspects are available in the literature [6,39,41].

The primary reaction inside the cell is the liberation of chloride and hydrogen ions. The reduction at cathode releases H_2 , and oxidation at anode release chlorine. The liberated hydrogen gas bubbles set up a circulation of the liquid electrolyte through the gap between the electrodes in the cell, leading to natural stirring action. As a result, chlorine gas formed dissolves in the bulk solution, giving hypochlorous acid, which partially disintegrates to form hypochlorite ions, otherwise called active chlorine. The kinetics of the transformation of active chlorine to chlorate in the bulk depends on the pH and local concentration of active chlorine [1]. If the pH of the electrolyte is congenial, i.e., pH value lies in the range 5.9 to 6,

chlorate formation takes place by auto-oxidation with maximum energy efficiency:



This reaction is not immediate, so if pH is not controlled, secondary reactions occur in the cell, leading to a significant loss in the current efficiency [2-5]. If the pH of the bulk is not in the required range, an undesirable parasitic reaction occurs, leading to anodic chlorate formation, and the cell efficiency can be as low as 66.66%. The reaction is given by equation (3) [39]:



Hence, control of the pH of the bulk is essential for energy efficiency and the quality of the product.

In this study, the control of the pH of bulk electrolyte is performed with the help of a FOPID controller tuned using particle swarm optimization for manipulating the NaOH flow rate.

The fundamentals of fractional-order proportional integral derivative controller (FOPID)

Fractional order PID controllers can be considered as improved PID controllers with non-integer integration and derivation parts. Fractional-order controllers were initially put forward by Igor Podlubny in 1997 and are denoted as $\text{P I}^\lambda \text{D}^\mu$, where λ and μ are non-integral orders. Figure 2 depicts the basis of the FOPID controller.

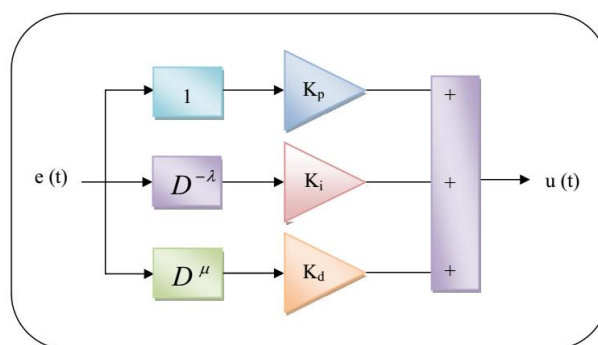


Figure 2. Block schematic of FOPID controller structure.

The fractional-order PID controller can be represented as:

$$G_{\text{FOPID}}(s) = \frac{u(s)}{e(s)} = K_c \left(1 + \frac{1}{T_i(s^\lambda)} + T_d(s^\mu) \right) \quad (4)$$

where λ and μ are real numbers, K_c is the gain, T_i is the integration constant and T_d is the differentiation constant. If $\lambda=0$ and $\mu=0$, it becomes a proportional (P) controller. If $\lambda=0$ and $\mu=1$, it becomes a PD (proportional

and derivative) controller. If $\lambda=1$ and $\mu=0$, the controller becomes the PI (proportional and integral) controller. If $\lambda=1$ and $\mu=1$, then it becomes PID (proportional integral and derivative) controller. The non-integer order gives two additional degrees of freedom to the controller and creates the chance to improve the performance of the conventional PID controllers.

The FOPID controller is a generalized version of the integer-order PID controller. The value of λ and μ expands the controller from a point to plane in λ and μ , thus providing more flexibility and accuracy in the PID controller design. The proper choice of the five parameters of the FOPID controller will offer better performance. Since more parameters are tuned, the associated optimization problem will also be problematic. In this paper, the optimization problem is tackled using the PSO algorithm.

Optimization using particle swarm algorithm (PSO)

Particle swarm optimization (PSO) was put forward by Kennedy and Eberhart [42]. PSO is a bio-inspired stochastic optimization algorithm that mimics the social behavior of a school of fish or a swarm of birds. The communication between the birds about the location of food or location for migration based on individual learning is utilized to find the optimum value in the search space. For example, if a flock of birds is seeking food in a territory, all the birds may not know the food location. Therefore, the best approach is to chase the bird closest to the food [43]. The potential solutions to the problem form the group or population in PSO. Each solution member is called a particle having a fitness value, assessed using the fitness function. Each particle has an associated position and velocity, which guides the progression of the particles. They move in the problem search space, track the present optimum particles to find the most appropriate solution, and then save it in the memory.

PSO has been proved helpful in optimizing various engineering applications, like power system problems, power converters, controller design, etc. [13,17,19,26,31,44,45]. It initializes the population of a random solution as in evolutionary computation methods and searches for the optimum solution by updating generations. However, unlike GA, PSO does not have evolution operators.

The popularity of PSO is due to its simplicity, ease of modification, and very few parameters for adjustment. As there are no crossover and mutation operators, PSO takes less computation time than a genetic algorithm and is easy to implement. In the present study, the PSO algorithm calculates the controller design parameters by minimizing the error

performance index. The FOPID controller parameters K_c , T_i , T_d , λ , μ are considered as particles, and the search space is a five-dimension space bounded by the limits of these parameters. PSO is boot up with a potential population of these particles. It is updated in each iteration based on fitness value. In each iteration of PSO, each particle is updated with the best fitness value the particle has acquired thus far, known as p_{best} , and the best fitness value obtained as yet by any particle in the population known as g_{best} . After storing p_{best} and g_{best} , the position and velocity of the particle are revised. The steps of PSO are detailed below.

Step 1:

The PSO initializes the population, a set of random solutions in the D dimension space bounded by the upper and lower limit. The location of the particle 'i' is characterized as:

$$X_i = (x_1, x_2, \dots, x_n) \quad (5)$$

where, X_i - locality of the particle.

The particle encompasses memory of the prior best position, depicted by the relation below:

$$P_i = (p_1, p_2, \dots, p_n) \quad (6)$$

where, P_i - the prior best position.

The velocity of the particle is presented as per the expression:

$$V_i = (v_1, v_2, \dots, v_n) \quad (7)$$

where, V_i - velocity of the particle.

Step 2: Utilizing the relative equation concerning the whole particle, compute fitness value

$$F_i = \min(J) \quad (8)$$

The best fitness value attained so far is chosen as the global best.

Step 3: If the fitness is superior to the earlier p_{best} , set the present values as the novel p_{best} . The new populations are approximated according to the PSO algorithm's two specifications.

$$v_i^{(n+1)} > v_m^{(n+1)}, \text{ then } v_i^{(n+1)} = v_m^{(n+1)} \quad (9)$$

Step 4: Step 3 and step 4 for the whole particles were performed, and select the best particle as the g_{best} .

The velocity and position of the particles in the population need to be updated. Each particle has data about the g_{best} and p_{best} and it tends to vary its location employing data such as the distance among the present position and p_{best} , the distance among the present position, and g_{best} . The updating of velocity and position of the particle is done as follows:

$$velocity_i = velocity^c + \alpha(p_{best} - pos^c) + \beta(g_{best} - pos^c) \quad (10)$$

$$V_i^{(n+1)} = V_i^{(i)} + I_1 \cdot r_1 \cdot (pb_i - p_i^{(i)}) + I_2 \cdot r_2 \cdot (gb_i - p_i^{(i)}) \quad (11)$$

$$x_i^{(i+1)} = x_i^{(i)} + V_i^{(i+1)} \quad (12)$$

Step 5: If the maximum iteration is not met, continue steps after the fitness function calculation.

Since the problem dimension is small, the number of maximum iterations is a good choice for stopping criteria, compared to other commonly used criteria, like the minimum value of cost function, the maximum number of function evaluation, maximum CPU time, etc. On the other hand, there is no improvement in fitness value after a certain fixed number of iterations, so metaheuristics need to be stopped after that many iterations. In Figure 3 flow chart of PSO is explained.

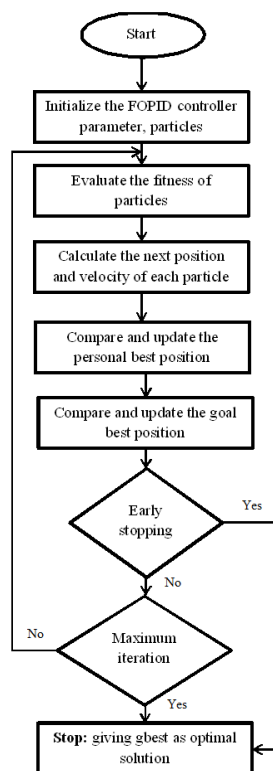


Figure 3. Flowchart of Proposed PSO algorithm.

Tuning of fopid controller for sodium chlorate cell using PSO algorithm

This paper proposes a FOPID controller to control pH in industrial sodium chlorate cells using the PSO algorithm. Figure 4 shows the proposed control strategy of the pH of chlorate cell bulk.

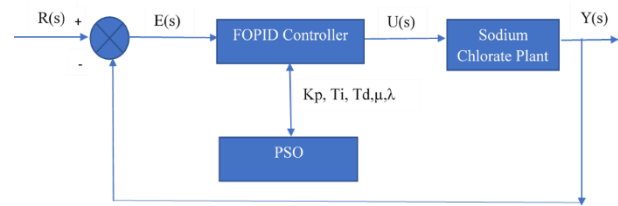


Figure 4. Schematic diagram of the suggested controller strategy.

PSO is utilized to find the optimal values of K_p , T_i , T_d , λ , and μ such that the controlled system exhibits the desired performance, evaluated using the performance specifications. These five parameters form a particle. The optimization using the PSO algorithm utilizes an objective function which is a weighted error performance indicator using the integral square error (ISE), the integral absolute error (IAE), and the integral time absolute error (ITAE). Even though the IAE and ISE indexes lead to a relatively minor overshoot, the settling time may be lengthy. This issue can be overcome by including the ITAE in the objective function. The weighting values are varied from 0 to 20, with a greater weighing for the ITAE. The following is the objective function for tuning of FOPID parameters:

$$J = w_1 ISE + w_2 IAE + w_3 ITAE \quad (13)$$

$$ISE = \int e(t)^2 dt \quad (14)$$

$$IAE = \int e(t) dt \quad (15)$$

$$ITAE = \int_0^T t |e(t)| dt \quad (16)$$

where $e(t)$ is the error between the setpoint and output of the plant. The effectiveness of the suggested controller is assessed using the time-domain specifications like settling time, rise time, and peak overshoot and compared with traditional PI and PID controller tuned using PSO. The sodium chlorate cell model described in [46] is used in this paper. The model of the cell takes HCl flow rate, NaOH flow rate, electrolyte temperature, DC load current, and the pH of the feed as input to give the pH of the bulk electrolyte.

Simulation results

In this segment, the simulation details of the suggested FOPID controller and performance comparison with PI and PID controller are included. The MATLAB 2019b is employed to implement and test the proposed controller. The pH of the bulk should be regulated to 5.9–6.3 to improve the current efficiency of the cell and reduce power consumption. The proposed FOPID controller can be used for manipulating the

NaOH flow rate to maintain the pH of the bulk. Figure 5 presents the system in Simulink.

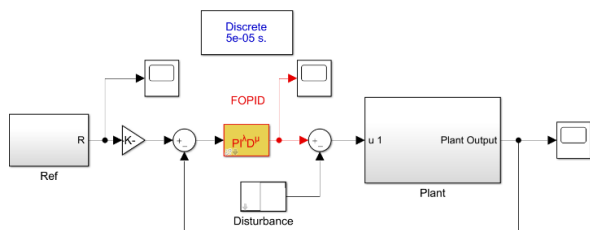


Figure 5. Simulink model of the proposed controller.

To optimally tune the FOPID controller employing the PSO algorithm, the FOPID variables bound are chosen, inspired from the practical requirements of the sodium chlorate plant, as $K_p \in [0, 60]$, $T_i \in [0, 15]$, $T_d \in [0, 40]$, $\lambda \in [0, 4]$, $\mu \in [0, 4]$. Table 1 lists the variables of the PSO algorithm.

Table 1. Variables of PSO Algorithm

Variables	Values used
Dimension	5
Population	100
Iterations	1000
c_1	1.5
c_2	2.0
Inertia weight	1

Figure 6 shows the pH value of cell bulk controlled using PI, PID, and FOPID-PSO controller. It is evident from the figure that the FOPID -PSO controller is capable of better regulation than the integral counterparts.

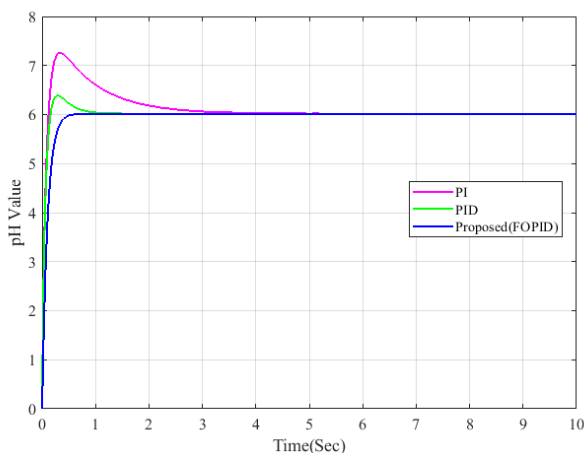


Figure 6. Performance comparison of different controller strategies for pH in sodium chlorate cell.

Table 2 reveals the values of time-domain performance indices and the error indicators of the system with PI, PID, and FOPID-PSO controllers, thus indicating that the FOPID-PSO controller gives superior performance compared to other control strategies. Figure 7 presents the bode diagram of the chlorate cell with the FOPID controller. The Bode plots are smooth, which is a pointer to the system's robustness. The comparison of the system's closed-loop performance for disturbance rejection is simulated using step changes in HCl flow rate. Figure. 8 shows that the setpoint tracking and settling ability of FOPID is better than other controllers. The figure also depicts the fact that the control signal is smoother in the case of FOPID. Table 3 gives the controller parameters obtained.

Table 2. Comparative analysis of the performance of different control strategies of pH of sodium chlorate cell bulk

Parameters	PI	PID	FOPID
IAE	0.8556	0.9076	0.8397
ISE	0.1755	0.1772	0.1743
ITAE	0.7591	0.9382	0.9027
Rise time (s)	0.05	0.03	0.01
Overshoot time (s)	0.45	0.8	-
Settling time (s)	4	1	0.5
J	1.0536	1.0644	1.01883

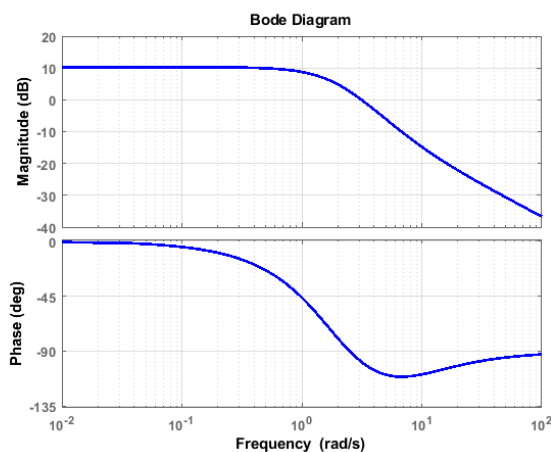


Figure 7. Bode diagram of chlorate cell model with FOPID controller.

The following conclusions are drawn, as it appears from the results obtained:

FOPID controller using PSO proved to have better control of the pH of chlorate cell than conventional controllers used in the plant concerning time-domain indicators, like peak overshoot, rise time, and settling

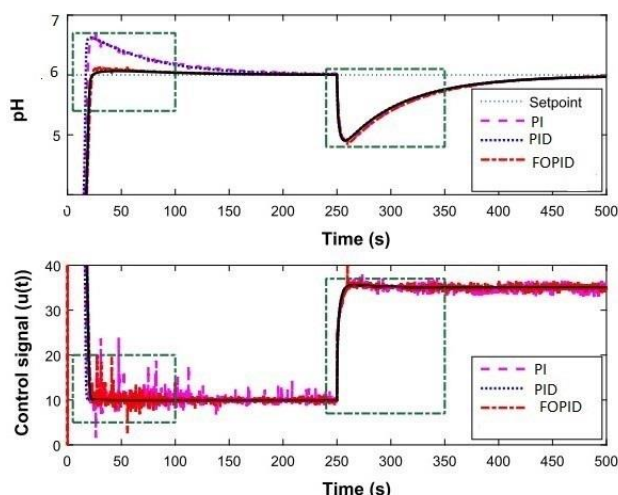


Figure 8. Comparison of controller performance for disturbance rejection.

Table 3. Controller parameters

Parameters	K_p	T_i	T_d	λ	μ
PI-PSO	1.3308	3.4222	0	1	0
PID-PSO	6.67134	7.50230	0.05440	1	1
FOPID-PSO	56.5	0.5	40	3.8336	1.1714

time, and error indicators, like ISE, IAE, and ITAE. For example, the PSO-based FOPID controller makes the plant settle in 0.5 s with a very low-rise time of 0.1 s. Also, the PSO-FOPID controller performance for disturbance rejection is better than PSO-PI and PSO-PID controllers.

The FOPID controller output is smooth to prevent the damage of delicate manipulating elements.

This work can facilitate achieving the maximum current efficiency of chlorate cells by favoring auto-oxidation and hence energy-efficient chlorate production. For future investigation, the proposed controller design can be used for inline control of cell pH, with online parameter updating

CONCLUSION

The pH of the sodium chlorate cell bulk is a key decisive factor for auto oxidation-based chlorate production in the cell, leading to maximum cell efficiency and thereby energy-efficient sodium chlorate production. Hence accurate pH control of sodium chlorate cell bulk is of utmost importance. In this study, a PSO-based FOPID controller for pH control in

sodium chlorate cells has been investigated. The performance of the proposed FOPID controller using PSO was validated by comparing the time domain indices like settling time, rise time and peak overshoot and error indices like integral square error (ISE), integral absolute error (IAE), and integral time absolute error (ITAE) with the integer-order PI controller and PID controller. The motivation behind the controller design was the significance of the pH of cell bulk in improving the efficiency of sodium chlorate production. The highlight of the controller is that it is flexible, simple to realize, and the time of computation is minimal as few parameters need to be adjusted in PSO.

REFERENCES

- [1] K. Viswanathan, J. Electrochem. Soc. 131 (1984) 1551.
- [2] B. Endrődi, S. Sandin, V. Smulders, N. Simic, M. Wildlock, G. Mul, B.T. Mei, A. Cornell, J. Clean. Prod. 182 (2018) 529-537.
- [3] G. Gordon, S. Tachlyashki, Environ. Sci. Technol. 25 (1991) 468-474.
- [4] M.M. Jaksic, J. Electrochem. Soc. 121 (1974) 70-79.
- [5] Y.J. Jung, K.W. Baek, B.S. Oh, J.W. Kang, Water Res. 44 (2010) 5345-5355.
- [6] L.R. Czarnetzki, N. Eindhoven University of Technology, Eindhoven, Doctoral T (1989) 154.
- [7] L.R. Czarnetzki, L.J.J. Janssen, J. Appl. Electrochem. 22 (1992) 315-324.
- [8] S. V. Evdokimov, Russ. J. Electrochem. 37 (2001) 786-791.
- [9] J. Wulff, A. Cornell, J. Appl. Electrochem. 37 (2007) 181-186.
- [10] A. Tepljakov, B.B. Alagoz, C. Yeroglu, E. Gonzalez, S.H. HosseinNia, E. Petlenkov, IFAC-PapersOnLine 51 (2018) 25-30.
- [11] I. Podlubny, IEEE Trans. Automat. Contr. 44 (2002) 208-214.
- [12] B. Puchalski, T.A. Rutkowski, K. Duzinkiewicz, ISA Trans. (2020).
- [13] R. Rajesh, SN Appl. Sci. 1 (2019) 1-14.
- [14] L.H. Tong, Y.G. Li, H.Q. Zhu, W.T. Li, IOP Conf. Ser. Earth Environ. Sci. 427 (2020) 12-26.
- [15] M. Yaghi, M.O. Efe, IEEE Trans. Ind. Electron. 67 (2020) 4806-4814.
- [16] E. Anbarasu, M.V. Pandian S, A.R. Basha, Microprocess. Microsyst. 74 (2020) 103030.
- [17] N.M.H. Norsahperi, K.A. Danapalasingam, ISA Trans. 102 (2020) 230-244.
- [18] A. Sikander, P. Thakur, R.C. Bansal, S. Rajasekar, Comput. Electr. Eng. 70 (2018) 261-274.
- [19] F.A. Hasan, L.J. Rashad, Int. J. Power Electron. Drive Syst. 10 (2019) 1724-1733.
- [20] S.K. Swain, D. Sain, S.K. Mishra, S. Ghosh, AEUE - Int. J. Electron. Commun. 78 (2017) 141-156.
- [21] P. Roy, B.K. Roy, ISA Trans. 63 (2016) 365-376.
- [22] I. Shivakoti, G. Kibria, P.M. Pradhan, B. Bahadur, A. Sharma, Mater. Manuf. Process. 00 (2018) 1-10.
- [23] R. Ranganayakulu, G. Uday Bhaskar Babu, A. Seshagiri Rao, D.S. Patle, Resour. Technol. 2 (2016) S136-S152.
- [24] M.-K. Salehtavazoei, Mohammad, IET Control Theory

- Appl. 8 (2014) 319-329.
- [25] T. Binazadeh, M.H. Shafiei, *Mechatronics* 23 (2013) 888-892.
- [26] Y. Tang, X. Zhang, D. Zhang, G. Zhao, X. Guan, *Neurocomputing* 111 (2013) 122-130.
- [27] M.P. Aghababa, *Soft Comput.* 20 (2016) 4055-4067.
- [28] R. Sharma, K.P.S. Rana, V. Kumar, *Expert Syst. Appl.* 41 (2014) 4274-4289.
- [29] H. Delavari, R. Ghaderi, A. Ranjbar, S. Momani, *Commun. Nonlinear Sci. Numer. Simul.* 15 (2010) 963-978.
- [30] H. Delavari, R. Ghaderi, A. Ranjbar, S. Momani, *Commun. Nonlinear Sci. Numer. Simul.* 15 (2010) 963-978.
- [31] R. Pradhan, S.K. Majhi, J.K. Pradhan, B.B. Pati, *Ain Shams Eng. J.* 11 (2019) 281-291.
- [32] K. Bingi, R. Ibrahim, M.N. Karsiti, S.M. Hassan, *Arab. J. Sci. Eng.* 43 (2018) 2687-2701.
- [33] A. Djari, T. Bouden, A. Boulkroune, *Int. Conf. Syst. Control* 1 (2013) 1-6.
- [34] M.C. Heredia-Moliner, J. Sánchez-Prieto, J. V. Briongos, M.C. Palancar, *J. Process Control* 24 (2014) 1023-1037.
- [35] S. Tufenkci, 2018 *Int. Conf. Artif. Intell. Data Process.* (2018) 1-6.
- [36] S.K. Prince, K.P. Panda, V.N. Kumar, G. Panda, 2018 *IEEMA Eng. Infin. Conf. ETechNXT 2018* (2018) 1-6.
- [37] M. Zamani, M. Karimi-ghartemani, N. Sadati, M. Parniani, *Control Eng. Pract.* 17 (2009) 1380-1387.
- [38] A. Kumar, V. Kumar, *AEU - Int. J. Electron. Commun.* 79 (2017) 219-233.
- [39] K. Viswanathan, B. V. Tilak, *J. Electrochem. Soc.* 131 (1984) 1551-1559.
- [40] R.K.B. Karlsson, A. Cornell, *Chem. Rev.* 116 (2016) 2982-3028.
- [41] L.C. Adam, G. Gordon, *Inorg. Chem.* 38 (1999) 1299-1304.
- [42] R. Eberhart, J. Kennedy, *Proc. Int. Symp. Micro Mach. Hum. Sci.* (1995) 39-43.
- [43] N. Nalini, G. Raghavendra Rao, *Inf. Sci. (Ny)*. 177 (2007) 2553-2569.
- [44] L.T. Le, H. Nguyen, J. Dou, J. Zhou, *Appl. Sci.* 9 (2019) 1-23.
- [45] I. Pan, S. Das, *ISA Trans.* 62 (2016) 19-29.
- [46] S. Sreekumar, A. Kallingal, V. Mundakkal Lakshmanan, *Chem. Eng. Commun.* 208 (2021) 256-270.

SREEPRIYA SREEKUMAR ^{1,2}
 APRNA KALLINGAL ¹
 VINILA MUNDAKKAL
 LAKSHMANAN ^{1,2}

¹ Department of Chemical
 Engineering, National Institute of
 Technology, NIT Campus
 P.O.673601 Calicut, India

² Department of Applied
 Electronics and Instrumentation,
 Adi Shankara Institute of
 Engineering and Technology,
 Kalady, India

NAUČNI RAD

KONTROLA pH U NATRIJUM-HLORATNOJ ĆELIJI POMOĆU PSO-FOPID REGULATORA RADI POBOLJŠANJA ENERGETSKE EFIKASNOSTI

Industrijska proizvodnja natrijum hlorata je visoko energetski intenzivan elektrohemijski proces. Ako se pH hloratne ćelije ne kontroliše, trenutna efikasnost pada sa 99% na čak 66,66%. Stoga je kontrola pH hloratne ćelije veoma značajna za energetski efikasnu proizvodnju natrijum hlorata. Ova studija predlaže frakcioni PID regulator (FOPID) za kontrolu pH ćelije natrijum hlorata. Optimizacija rojem čestica (PSO) utiče na podešavanje varijabli FOPID regulatora. Ovaj regulator je fleksibilan, jednostavan za primenu i sa malim vremenom izračunavanja, jer je potrebno podešavanje nekoliko parametara optimaizacijom rojem čestica. Analizirane su performanse predloženog PSO-FOPID regulatora u poređenju sa tradicionalnim PI i PID regulatorima koristeći mere u vremenskom domenu, kao što su vreme poravnanja, vreme porasta i prekoračenje maksimuma, i indikatori greške, kao što su integralna kvadratna greška (ISE), integralna apsolutna greška (IAE), i apsolutnu grešku integralnog vremena (ITAE). FOPID regulator koji koristi PSO radi dobro u poređenju sa konvencionalnim regulatorima sa vremenom podešavanja od 0,5 s i vremenom porasta od 0,1 s. Dakle, FOPID-PSO regulator ima bolje praćenje zadate vrednosti, što je od suštinskog značaja za proces koji se razmatra.

Ključne reči: frakcioni PID regulator, natrijum-hlorat, optimizacija rojem čestica, pH kontrola.

NAVEEN PRASAD B. S. 1,
SELVARAJU SIVAMANI¹
AZUCENA CUENTO¹
SENTHILKUMAR
PACHIYAPPAN²

¹ Chemical Engineering
Section, Engineering
Department, University College
of Technology and Applied
Sciences- Salalah, Salalah,
Oman

² Department of Chemical
Engineering, Sathyabama
Institute of Science &
Technology, Chennai, India

SCIENTIFIC PAPER

UDC 663.813:547.477:66

*The paper was presented as abstract at the International e-Conference on Bioengineering for Health & Environment (ICBHE-2020), July 16th & 17th, 2020 Proceedings International Platinum Open Access Journal Volume 2, Issue 1, 2020, 98.

CHEMICAL ROUTE FOR SYNTHESIS OF CITRIC ACID FROM ORANGE AND GRAPE JUICES *

Article Highlights

- Chemical route was attempted to synthesize citric acid from orange and grape juices
- Process parameters were optimized for maximum citric acid yield
- FTIR and XRD characterization was performed for purified citric acid crystals

Abstract

Citrus fruits contain sufficient citric acid, which is the main tricarboxylic acid. The properties of citric acid make it an important additive in various process industries. This experimental study aims to produce citric acid from orange and grape juices. The chemical route for the synthesis of citric acid from citrus juices involves three steps: (i) neutralization to adjust pH (9-11) with a 2.8 M NaOH solution, (ii) addition of CaCl₂ solution (40.3-41.1% w/v), and (iii) acidification with an H₂SO₄ solution (1.5-2.3 M) to produce citric acid. In this study, the fruits were peeled, crushed, filtered, neutralized, added CaCl₂ solution, and acidified to obtain citric acid. The experiments were carried out by varying the final pH of the solution and the concentrations of CaCl₂ and H₂SO₄ solutions, maintaining the total volume constant. A maximum citric acid yield of 91.1% and 79.8% were achieved from orange and grapefruits, respectively, at the optimum final pH of the solution and the concentrations of CaCl₂ and H₂SO₄ solutions at 10, 40.7% w/v, and 1.9 M, respectively. Finally, the purified citric acid crystals were characterized using FTIR and XRD. Thus, it could be concluded that orange fruit would be a promising source for citric acid production than grape.

Keywords: orange juice, grape juice, neutralization, calcium chloride, acidification, citric acid.

Citric acid (IUPAC: 2-hydroxy-1,2,3-propane tricarboxylic acid), a natural ingredient, is a common versatile metabolite (organic acid) of plants and animals used in the food sector (60%) and pharmaceuticals (10%) [1]. It was first crystallized from lemon juice. It finds its role in the metabolism of all aerobic organisms that Krebs did not announce in the late 1930s. The production of citric acid from lemon reached a peak of 17,500 tons between 1915 and 1916. In the 19th century, citric acid was extracted di-

rectly from the concentrated lemon juice, mainly in Sicily [2]. The worldwide production of this acid by fermentation is increasing rapidly. Today over 99% of global citric acid production is from green citrus fruits by South America, Mexico, and Greece. In 1934, Yuill and Bennett discovered the XRD pattern of the crystal structure of anhydrous citric acid obtained by cooling a hot concentrated solution of the monohydrate [3].

Citric acid is used due to its remarkable physicochemical properties and environmentally friendly nature. Citric acid was previously produced using three methods: extraction from citrus fruits, chemical synthesis, and fermentation. In the chemical route of synthesis, three methods are used to synthesize citric acid: (i) the addition of lime (CaO) to citrus juice, and the acidification with dilute sulfuric acid; (ii) the addition of limestone (CaCO₃) to citrus juice, and the acidification with dilute sulfuric acid; and (iii) the addition of caustic soda (NaOH), followed by calcium

Correspondence: B.S.N. Prasad, Chemical Engineering Section, Engineering Department, University College of Technology and Applied Sciences- Salalah, Salalah, Oman.
E-mail: bsnaveenprasad@gmail.com
Paper received: 11 August, 2020.
Paper revised: 23 June, 2021.
Paper accepted: 9 July, 2021.

<https://doi.org/10.2298/CICEQ200820025N>

chloride to citrus juice, and the final acidification with dilute sulfuric acid [4]. In the biochemical or fermentation route, fungi (particularly molds), such as *Aspergillus niger*, *A. awamori*, *A. aculeatus*, *A. wentii*, *A. carbonarius*, *A. factidus*, *Penicillium janthinelum*, *Saccharomycopsis lipolytica*, *Candida oleophila*, *C. tropicalis*, *C. parapsilosis*, *C. guilliermondii*, *C. citroformans*, *Corynebacterium sp.*, *Arthrobacter paraffinens*, *Bacillus licheniformis*, etc. were used to ferment glucose to citric acid through Kreb's cycle by solid-state or submerged fermentation [5]. Mainly *Aspergillus* species are used in studies because of their relatively high yield, ease of harvesting, and ability to use various raw materials [6].

The first industrial fermentation of citric acid was initially carried out as surface cultures. The introduction of submerged fermentation has been a significant improvement. Among the works examined before the commercial implementation of submerged fermentation was that of Perquin in 1938; it should be mentioned first for its skill and precision, comparable to Currie's work in the surface process [7]. In 2012, Ray *et al.* cleared that an enhanced efficient fermentation process and genetically modified organisms are required for higher yield and purity. Although many citric acid suppliers use molasses from genetically modified corn and genetically modified sugar beets, other manufacturers only produce citrate products formed from carbohydrates obtained from non-genetically modified crops and without the involvement of recombinant microorganisms, rDNA technology [8].

Seligra *et al.* (2016) investigated the cross-linked citric acid with starch using glycerin as a plasticizer by heating a mixture of starch, glycerin, water, and citric acid to 75-85 °C. The resulting citric acid films treated at 75 °C showed a significant decrease in moisture absorption and water vapor permeability. These two main parameters affect the barrier properties of packaging films. Crosslinking starch-glycerin films with citric acid also dramatically improves starch films' poor thermal degradation and mechanical properties [9]. Citric acid is an excellent and harmless disinfectant against various viruses, including the human norovirus. For example, citrate, added to norovirus-like particles, binds precisely to the binding pocket of histo-blood group antigens involved in binding to host ligands, thereby preventing the transmission of these viruses and preventing symptoms in people already infected with norovirus [10].

In the present study, citric acid was synthesized through a chemical route by adding caustic soda and calcium chloride and final acidification with dilute sulfuric acid. In the production process, three steps are involved: neutralization, reaction with calcium chloride,

and acidification. During neutralization, sodium hydroxide was added to citrus juice to neutralize the pH from <4 to 10. As a result, citric acid in fruits reacts with sodium hydroxide to form trisodium citrate and water (Figure 1(a)). During the addition of calcium chloride, sodium citrate reacts with calcium chloride to produce tricalcium dicitrate and sodium chloride (Figure 1(b)). During acidification, tricalcium dicitrate reacts with sulphuric acid to form citric acid and calcium sulfate (Figure 1(c)) [11].

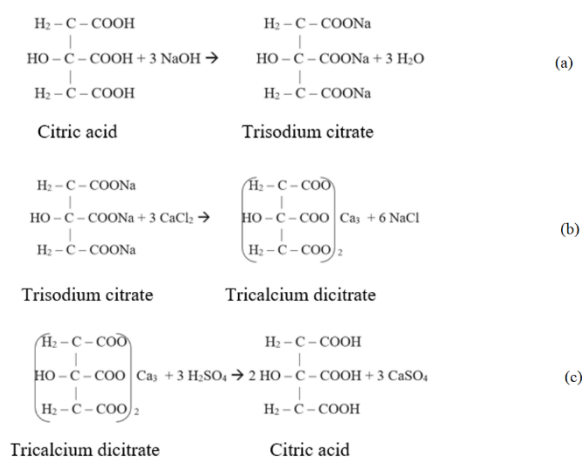


Figure 1. Chemical reactions involved in citric acid production from citrus fruit juices.

Even though the biochemical synthesis route is being used commercially to produce citric acid, the chemical route is used for production on a small scale in a few countries. Many papers are available on the biochemical route of citric acid synthesis compared to the chemical route [12,13]. Hence, the present study aims to evaluate the citric acid yield from citrus fruits' chemical route for the synthesis of citric acid from citrus (orange and grape) fruits. The objectives of the study are to study the effects of pH during neutralization, the concentration of CaCl_2 during the second step, and the concentration of sulfuric acid during acidification on the citric acid yield.

MATERIALS AND METHODS

Materials

Fresh citrus fruits (orange and grape) were purchased from the local commercial market, Salalah, Sultanate of Oman. They were washed thoroughly before use. The fruits were peeled, crushed, and filtered twice to remove seeds and other insoluble impurities. The extracted fruit juices were used for the synthesis of citric acid. Sodium hydroxide, calcium chloride, and sulfuric acid of analytical grade were used in the experiments without processing.

Methods

The fruit juices of 10 mL (V_a) were titrated with a 0.1 M NaOH solution using phenolphthalein as an indicator to calculate the mass of citric acid in the feed. The remaining total volume of juice (V_f) was measured. The pH of fresh juice was measured and found to be 3.3 for orange and 3.7 for grape. For neutralization, a 2.8 M NaOH solution (10% w/w) was added to fruit juices drop-by-drop, mixing properly to 10 pH. During neutralization, Na atoms in NaOH displace H atoms in carboxylic groups of citric acid based on pK_a value in steps. Sodium citrate produced is soluble in solution, and the remaining products except water are insoluble. Hence, the resultant mixture was filtered using filter paper to remove the insoluble part. The filtrate containing an aqueous sodium citrate solution and an aqueous sodium citrate solution was filtered thrice using filter paper again before proceeding to the second step.

In the second step, a known volume of CaCl_2 (calculated in section 2.3) of 40.7% w/v was added to the sodium citrate solution and heated in a boiling water bath for 30 min. A double displacement reaction takes place between sodium citrate and CaCl_2 . Calcium citrate is insoluble in water and precipitated at the bottom. So, the resultant mixture containing calcium citrate was filtered using vacuum filtration. The residue was washed with 100 mL of hot water in 4 steps to remove the impurities and byproducts. During the addition of hot water, the residue was stirred well. A neutral pH of 7 was ensured in the filtrate. If the pH of the filtrate is higher than 7, then more hot water should be added with stirring; if the pH value is less than 7, proceed to acidify. The resultant residue was dried to constant weight in a hot air oven.

Dried calcium citrate was acidified with a known volume of dilute H_2SO_4 (calculated in section 2.3) of 1.9 M and heated at 60 °C with simultaneous mixing with a glass rod. Calcium citrate and calcium sulfate are insoluble in water, whereas citric acid is soluble. So, when calcium citrate and sulfuric acid were mixed, calcium sulfate precipitated at the bottom, leaving behind the citric acid solution at the top. Again, the mixture was vacuum filtered. Finally, citric acid was crystallized from its aqueous solution by evaporative crystallization; the yield of citric acid crystals was estimated gravimetrically and characterized using XRD and FTIR.

Calculations involved in the experimental methods

Orange juice

Total volume of fresh orange juice (V_f)=330 mL. From literature [14], concentration of citric acid in fresh

orange juice (C_o)=9.1 g/L. Mass of citric acid in orange juice = $(330 \times 9.1)/1000 = 3$ g. According to stoichiometry, 192 g of citric acid produces 258 g of sodium citrate, 3 g of citric acid produces $258/192 \times 3 = 4$ g sodium citrate. 258 g of sodium citrate requires 333 g of CaCl_2 . 4 g of sodium citrate requires $333/258 \times 4 = 5.2$ g of CaCl_2 . Concentration of $\text{CaCl}_2 = 40.7\%$ (w/v) = 407 g/L. Volume of CaCl_2 solution required = $5.2/407 = 0.0128$ L = 12.8 ml. 498 g of calcium citrate requires 294 g of H_2SO_4 . 5.4 g of dried calcium citrate requires = $294/498 \times 5.4 = 3.2$ g of H_2SO_4 . Density of H_2SO_4 solution = 1.84 g/mL. Volume of 100% H_2SO_4 required = $3.2/1.84 = 1.7$ mL. Volume of commercially available 98% (18.4 M) H_2SO_4 required = $1.7/98 \times 100 = 1.8$ mL. Volume of 10.2% (1.9 M) H_2SO_4 required = $18.4/1.9 \times 1.8 = 17.4$ mL.

Grape juice

Total volume of fresh grape juice (V_f) = 330 mL. From literature [14], concentration of citric acid in fresh grape juice (C_o) = 0.2 g/L. Mass of citric acid in grape juice = $(330 \times 0.2)/1000 = 0.066$ g = 66 mg. According to stoichiometry, 192 g of citric acid produces 258 g of sodium citrate. 66 mg of citric acid produces $258/192 \times 66 = 89$ mg sodium citrate. 258 g of sodium citrate requires 333 g of CaCl_2 . 89 mg of sodium citrate requires $333/258 \times 89 = 114$ mg of CaCl_2 . Concentration of $\text{CaCl}_2 = 40.7\%$ (w/v) = 407 g/L. Volume of CaCl_2 solution required = $114/1000 \times 407 = 0.0003$ L = 0.3 mL. 498 g of calcium citrate requires 294 g of H_2SO_4 . 0.12 g of dried calcium citrate requires = $294/498 \times 0.12 = 0.07$ g of H_2SO_4 . Density of H_2SO_4 solution = 1.84 g/mL. Volume of 100% H_2SO_4 required = $0.07/1.84 = 0.04$ mL. Volume of commercially available 98% (18.4 M) H_2SO_4 required = $1.7/98 \times 100 = 0.04$ mL. Volume of 10.2% (1.9 M) H_2SO_4 required = $18.4/1.9 \times 0.04 = 0.38$ mL.

Calculations for citric acid yield

Orange juice

(Moles of NaOH in fresh orange juice) = (Molarity of NaOH solution) \times (Volume of NaOH solution (mL)). (Moles of NaOH in fresh orange juice) = $0.1/1000 \times 15.5 = 0.00155$ mol. According to stoichiometry, 1 mole of citric acid requires 3 mol of NaOH. 0.00155 mol of NaOH requires $1/3 \times 0.00155 = 0.00052$ mol of citric acid. Total volume of fresh grape juice (V_f) = 330 mL. Moles of citric acid for total volume of juice = $(330 \times 0.00052)/10 = 0.017$ mol. Mass of citric acid in feed = (Moles of citric acid) \times (Molecular weight of citric acid). Mass of citric acid in feed = $0.017 \times 192 = 3.3$ g. Mass of citric acid in product found by gravimetry = 3 g. Percentage yield of citric acid = (Mass of citric acid in product)/(Mass of citric acid in feed) $\times 100$. Percentage yield of citric acid = $3/3.3 \times 100 = 90.9\%$.

Grape juice

(Moles of NaOH in fresh grape juice) = (Molarity of NaOH solution) × (Volume of NaOH solution (mL)).
 (Moles of NaOH in fresh grape juice) = $0.1/1000 \times 5.2 = 0.00052$ mol. According to stoichiometry, 1 mole of citric acid requires 3 mol of NaOH. 0.00155 mol of NaOH requires $1/3 \times 0.00052 = 0.00017$ mol of citric acid. Total volume of fresh grape juice (V_f) = 330 mL. Moles of citric acid for total volume of juice = $(330 \times 0.00017)/10 = 0.0057$ mol. Mass of citric acid in feed = (Moles of citric acid) × (Molecular weight of citric acid). Mass of citric acid in feed = $0.0057 \times 192 = 1.1$ g. Mass of citric acid in product found by gravimetry = 0.88 g. Percentage yield of citric acid = (Mass of citric acid in product)/(Mass of citric acid in feed) × 100. Percentage yield of citric acid = $0.88/1.1 \times 100 = 79.67\%$.

Statistical analysis

Treatments were organized with three replicates in randomized block design. The data were analyzed for statistical significance using ANOVA with a p-value < 0.05.

RESULTS AND DISCUSSION

Effect of process parameters on citric acid yield

Figure 2 shows the effect of final solution pH during neutralization on citric acid yield from the orange fruit. The effect of pH on citric acid yield was studied by varying the values from 9 to 11 in the steps of 0.5 at constant CaCl_2 and H_2SO_4 concentrations of 40.7% (w/v) and 1.9 M, respectively. The variation in pH exhibited an inverted parabolic curve. As the pH increased from 9 to 10 and then further to 11, the citric acid yield increased from 60.1 to 90.0 and then decreased to 87.8%, respectively. Figure 2 illustrates that the variation in pH between 9 and 10 is significant, whereas the variation between 10 and 11 is minimal. This may be because the mass of NaOH used for neutralization was insufficient to achieve maximum citric acid yield when pH was increased from 9 to 10 [15]. Nevertheless, when the pH was increased from 10 to 11, the maximum citric acid yield was achieved at pH 10. Citric acid undergoes a decomposition reaction at a slower rate at pH 11.

For grapes, the effect of final solution pH during neutralization was studied on citric acid yield. As the pH increased from 9 to 10 and then further to 11, the citric acid yield increased from 44.1 to 79.5 and then decreased to 60.6%, respectively. The variation in pH between 9 and 11 is most significant. This showed that the variation in pH is an essential factor to maximize the citric acid yield from grapes.

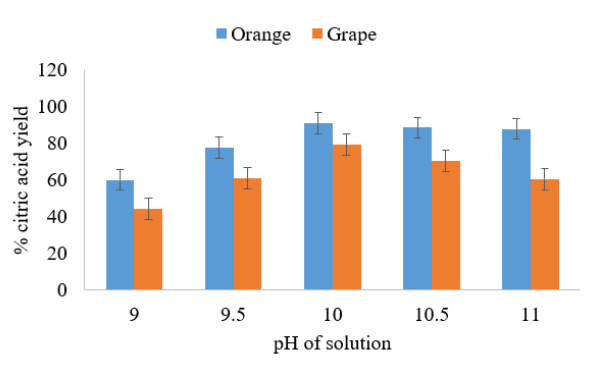


Figure 2. Effect of final pH of solution on citric acid yield during neutralization.

Figure 3 shows the effect of the concentration of CaCl_2 on citric acid yield. The effect of CaCl_2 concentration on citric acid yield was studied by varying the values from 40.3 to 41.1% (w/v) in the steps of 0.2% (w/v) at constant pH and H_2SO_4 concentration of 10 and 1.9 M, respectively. The variation in CaCl_2 concentration exhibited a flattened curve. As the CaCl_2 concentration increased from 40.3 to 40.7 and then further to 41.1% (w/v), the citric acid yield increased from 83.5 to 90.6 and then decreased to 88.2%, respectively. Figure 3 illustrates that the variation in concentration of CaCl_2 between 40.3 and 41.1 is minimal. For grapes, the effect of CaCl_2 was studied on citric acid yield. As the concentration of CaCl_2 increased from 40.3 to 40.7 and then further to 41.1% (w/v), the citric acid yield increased from 70.5 to 79.1 and then decreased to 77.8%, respectively. The variation in concentration of CaCl_2 between 40.3 and 41.1% (w/v) is minimal, like orange fruit. This showed that the variation in the CaCl_2 concentration does not significantly impact the citric acid yield from orange and grapefruits.

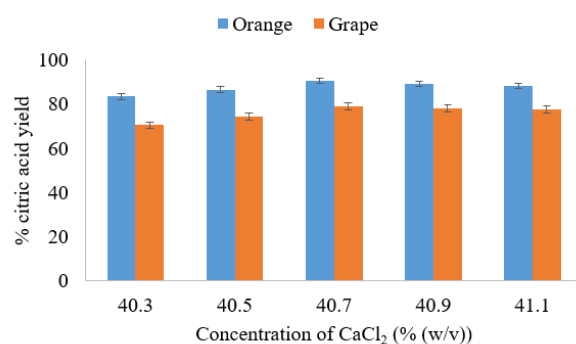


Figure 3. Effect of concentration of CaCl_2 solution on citric acid yield.

Figure 4 shows the effect of the concentration of H_2SO_4 on citric acid yield from orange during acidification. The impact of the concentration of H_2SO_4 on citric acid yield was studied by varying the values from 1.5 to 2.3 M in the steps of 0.2 M at constant pH and CaCl_2 concentration of 10 and 40.7% (w/v), respectively.

tively. The variation in concentration of H_2SO_4 exhibited a bell-shaped curve. As the concentration of H_2SO_4 increased from 1.5 to 1.9 and then further to 2.3 M, the citric acid yield increased from 72.5 to 91.1 and then decreased to 87.9%, respectively. Figure 4 illustrates that the variation in the concentration of H_2SO_4 between 1.5 and 1.9 M is significant, whereas the variation between 1.9 and 2.3 M is minimal.

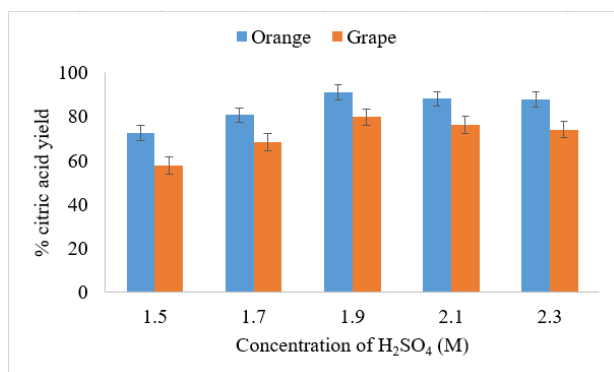


Figure 4. Effect of concentration of H_2SO_4 on citric acid yield during acidification.

For grapes, the effect of the concentration of H_2SO_4 during acidification was studied on citric acid yield. As the concentration of H_2SO_4 increased from 1.5 M to 1.9 M and then further to 2.3 M, the citric acid yield increased from 57.6% to 79.8% and then decreased to 74.2%, respectively. The variation in concentration of H_2SO_4 between 1.5 M and 1.9 M is most significant. This showed that the variation in concentration of H_2SO_4 between 1.5 M and 1.9 M is substantial, whereas the variation between 1.9 M and 2.3 M is minimal. The citric acid recovery from orange is better than grape because of its high citric acid content.

Characterization of citric acid crystals

FTIR

FTIR spectra of citric acid crystals revealed major peaks at 3300, 2600, 1730, and 1200 cm^{-1} depict stretching of -OH, C-H, C-C, and C=O, respectively. A peak at 3300 cm^{-1} represents the presence of moisture [16]. The peaks at 2600, 1730, and 1200 cm^{-1} represent the vibrational motions of the functional group stretching in the citric acid molecule [17]. However, the characteristic absorption band at 1274 cm^{-1} corresponds to the CH_2 stretching vibration in citric acid crystals (Figure 5).

XRD

XRD spectra of citric acid crystals revealed major peaks at 2θ values of 14°, 17°, 19°, 24°, 26°, and 29°, corresponding to the humps of pure citric acid (Figure 6). A peak at 24° indicates that the material starts gain-

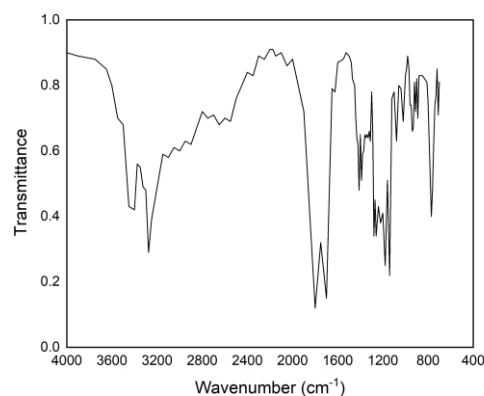


Figure 5. FTIR spectra of citric acid crystals.

ing short-range order or becomes a little bit more crystalline [18]. A peak at 26° corresponds to the reflections of the (002) lattice planes [19]. A peak at 29° is due to the presence of a carbon atom [20]. The diffraction pattern strongly affects heavier elements and contains more electrons. Since hydrogen is the lightest atom with only one electron, it is difficult to detect the presence of hydrogen atoms by XRD [21].

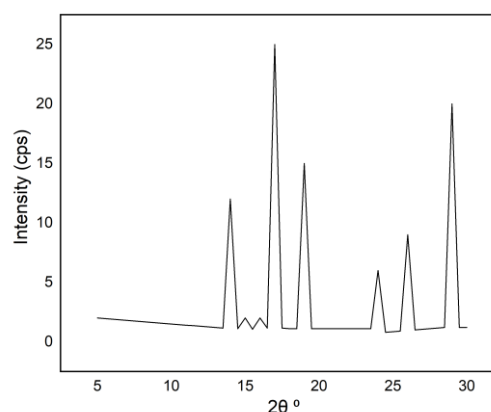


Figure 6. XRD spectra of citric acid crystals.

CONCLUSION

The present study aims to optimize the final pH of the solution (9 - 11), the concentration of CaCl_2 (40.3 - 41.1% (w/v)), and the concentration of H_2SO_4 (1.5 - 2.3 M) to maximize the citric acid yield. The citric acid yield increased when the final pH of the solution, the concentration of CaCl_2 , and the concentration of H_2SO_4 were 10, 40.7% (w/v), and 1.9 M, respectively, and decreased after that. FTIR and XRD spectra revealed the presence of functional groups and crystalline nature, respectively, corresponding to citric acid crystals. Thus, it could be concluded that orange fruit would be a promising source for producing citric acid.

Acknowledgment

We would acknowledge our heartfelt thanks to the Management of University College of Technology and Applied Sciences- Salalah, Sultanate of Oman, for the wonderful opportunity, continuing support and encouragement by providing necessary facilities for executing the research work.

REFERENCES

- [1] B. Max, J.M. Salgado, N. Rodríguez, S. Cortés, A. Converti, J.M. Domínguez, *Braz. J. Microbiol.* 41 (2010) 862-875.
- [2] K. Bekkar, R. Oumeddour, S. Nigri, R. Selaimia, *Emirates J. Food Agric.* 30 (2018) 621-630.
- [3] R.K. Thauer, *Eur. J. Biochem.* 176 (1998) 497-508.
- [4] R. Ciriminna, F. Meneguzzo, R. Delisi, M. Pagliaro, *Chem. Cent. J.* 11 (2017) 22.
- [5] V. Vasanthabharathi, N. Sajitha, S. Jayalakshmi, *Adv. Biol. Res.* 7 (2013) 89-94.
- [6] M. Ozdal, E. Kurbanoglu, *Waste Biomass Valori.* 10 (2019) 631-640.
- [7] P. Komáromy, P. Bakonyi, A. Kucska, G. Tóth, L. Gubicza, K. Bélafi-Bakó, N. Nemestóthy, *Fermentation* 5 (2019) 31.
- [8] M.R. Swain, R.C. Ray, J.K. Patra, *Citric Acid: Synthesis, Properties and Applications*, Edition, 1 (2011) 97-118.
- [9] P.G. Seligra, C.M. Jaramillo, L. Famá, S. Goyanes, *Data Brief* 7 (2016) 1331-1334.
- [10] A.D. Koromyslova, P.A. White, G.S. Hansman, *Virology* 485 (2015) 199-204.
- [11] S. Ghosh, S. Dasgupta, A. Sen, H. Sekhar Maiti, *J. Am. Ceram. Soc.* 88 (2005) 1349-1352.
- [12] A. Sudha, V. Sivakumar, V. Sangeetha, K.S. Priyenka Devi, *Chem. Ind. Chem. Eng. Q.* 23 (2017) 357-366.
- [13] B. Rivas, A. Torrado, P. Torre, A. Converti, J.M. Domínguez, *J. Agric. Food. Chem.* 56 (2008) 2380-2387.
- [14] K.L. Penniston, S.Y. Nakada, R.P. Holmes, D.G. Assimos, *J. Endourol.* 22 (2008) 567-570.
- [15] T. Roukas, L. Harvey, *Biotechnol. Lett.* 10 (1988) 289-294.
- [16] D. Xu, F. Lei, H. Chen, L. Yin, Y. Shi, J. Xie, *RSC Adv.* 9 (2019) 8290-8299.
- [17] L. Nalbandian, E. Patrikiadou, V. Zaspalis, A. Patrikidou, E. Hatzidakí, N. Papandreou, *Curr. Nanosci.* 12 (2016) 455-468.
- [18] X. Yao, K. Wang, S. Zhang, S. Liang, K. Li, C. Wang, T. Zhang, H. Li, J. Wang, L. Dong, Z. Yao, *Chemosphere* 258 (2020) 127320.
- [19] R. Jiang, J. Li, W. Cai, A. Xu, D. Cao, D. Chen, C. Shu, *J. Mater. Chem. A* 3 (2015) 19433-19438.
- [20] H. Groen, K. Roberts, *J. Phys. Chem. B* 105 (2001) 10723-10730.
- [21] A. Sinha, T. Mahata, B.P. Sharma, *J. Nucl. Mater.* 301 (2002) 165-169.

NAVEEN PRASAD B. S.¹,
SELVARAJU SIVAMANI¹
AZUCENA CUENTO¹
SENTHILKUMAR
PACHIYAPPAN²

¹ Chemical Engineering
Section, Engineering
Department, University College
of Technology and Applied
Sciences- Salalah, Salalah,
Oman

² Department of Chemical
Engineering, Sathyabama
Institute of Science &
Technology, Chennai, India

NAUČNI RAD

HEMIJSKA SINTEZA LIMUNSKJE KISELINE IZ SOKOVA POMORANDŽE I GREJFRUTA

Citrusno voće sadrži dovoljno limunske kiseline, koja je glavna trikarbonska kiselina. Svojstva limunske kiseline čine je važnim dodatkom u raznim procesnim industrijama. Ova eksperimentalna studija ima za cilj proizvodnju limunske kiseline iz sokova pomorandže i grejfruta. Hemijski sinteza limunske kiseline iz sokova citrusnog voća uključuje tri koraka: (i) neutralizaciju radi podešavanja pH (9-11) sa 2,8 M rastvorom NaOH, (ii) dodavanje rastvora CaCl₂ (40,3-41,1% v/v), i (iii) zakišeljavanje rastvorom H₂SO₄ (1,5-2,3 M). U ovoj studiji, da bi se dobila limunska kiselina, plodovi su oguljeni, usitnjeni, filtrirani, neutralizovani, tretirani rastvorom CaCl₂ i zakišljeni. Eksperimenti su izvedeni variranjem konačnog pH rastvora i koncentracija rastvora CaCl₂ i H₂SO₄, održavajući ukupnu zapreminu konstantnom. Maksimalni prinos limunske kiseline je 91,1% iz pomorandže i 79,8% iz grejfruta pri optimalnom konačnom pH rastvora od 10 i koncentracijama rastvora CaCl₂ i H₂SO₄ od 40.7% ml/v and 1,9 M, redom. Konačno, prečišćeni kristali limunske kiseline su okarakterisani korišćenjem FTIR i XRD analiza. Dakle, može se zaključiti da je pomorandža bolja sirovina izvor za proizvodnju limunske kiseline od grejfruta.

Ključne reči: sok od pomorandže, sok od grejfruta, neutralizacija, kalcijum hlorid, zakišeljavanje, limunska kiselina.

ABDALLAH ABDALLAH EL
HADJ^{1,2},
MAAMAR LAIDI²
SALAH HANINI²

¹ Faculty of Science, University
Saad Dahleb of Blida 1, Blida,
Algeria

² Laboratory of BioMaterial and
transfer Phenomena (LBMPT),
University of Medea, Medea,
Algeria

SCIENTIFIC PAPER

UDC 004.896:615:681

NEW METHOD BASED ON NEURO-FUZZY SYSTEM AND PSO ALGORITHM FOR ESTIMATING PHASE EQUILIBRIA PROPERTIES

Article Highlights

- Phase equilibria modeling is the key to the development and design of the separation process
- New method based on ANFIS and PSO algorithm for estimating the solubility of solids in $scCO_2$
- The ANFISi approach is used to estimate the critical properties from the solubility data
- A comparative study between the most used optimization algorithm where PSO gives the best results

Abstract

The subject of this work is to propose a new method based on the ANFIS system and PSO algorithm to conceive a model for estimating the solubility of solid drugs in supercritical CO_2 ($sc-CO_2$). The high nonlinear process was modeled by the neuro-fuzzy approach (NFS). The PSO algorithm was used for two purposes: replacing the standard backpropagation in training the NFS and optimizing the process. The validation strategy has been carried out using a linear regression analysis of the predicted versus experimental outputs. The ANFIS approach is compared to the ANN in terms of accuracy. Statistical analysis of the predictability of the optimized model trained with a PSO algorithm (ANFIS-PSO) shows a better agreement with the reference data than the ANN method. Furthermore, the comparison in terms of the AARD deviation (%) between the predicted results, the results predicted by the density-based models, and a set of equations of state demonstrates that the ANFIS-PSO model correlates far better with the solubility of the solid drugs in $scCO_2$. A control strategy was also developed for the first time in the field of phase equilibrium by using the neuro-fuzzy inverse approach (ANFISi) to estimate pure component properties from the solubility data without passing through the GCM methods.

Keywords: modeling, ANFIS, artificial neural networks, critical properties, particle swarm optimization.

Supercritical fluid technology is one of the most promising technologies to replace conventional techniques with plenty of advantages. Non-toxicity, low cost, availability, and the facility of separation are the major advantages of using this technology compared to the conventional one.

The knowledge with detail and accuracy of the equilibrium solubility is the key to the development and design of the separation process. With the various experimental data relative to the solubility of solid solutes in supercritical CO_2 ($scCO_2$) being published every year, the modeling of phase equilibria becomes of the primordial importance for the design and optimization issues, which leads to a gainful high selective process.

Artificial intelligence (AI) has been widely used in recent years in many fields of chemical engineering [1-3], renewable energy [4,5], and other areas [6-8] because of their good capacity of modeling and representing the different studied phenomena. Artificial

Correspondence: A.A:Hadj, Faculty of Science, University Saad Dahleb of Blida 1, Blida, Algeria.

E-mail: a_abdallahelhadj@yahoo.fr

Paper received: 4 November, 2020.

Paper revised: 22 April, 2021.

Paper accepted: 9 July, 2021.

<https://doi.org/10.2298/CICEQ201104024A>

neural network (ANN) among all techniques becomes very popular in modeling different engineering problems because of their ability to extract very complex relationships from serious nonlinear problems. However, some drawbacks can be accompanied by the use of ANN (the learning process is slow, and their optimized parameters are difficult to analyze where ANN is considered as a black-box tool [9]). To surpass these disadvantages, ANN can be combined with other intelligent techniques called "hybrid systems." In a previous work [10], a hybrid method based on the ANN and PSO algorithm was applied successfully to estimate the solubility of solid solutes in scCO₂. The ANN inverse method was used to predict the critical condition properties without using group contribution methods. In the same work, the advantage of considering the particle swarm optimization algorithm (PSO) compared to other optimization techniques (genetic algorithm and ant colony optimization (ACO)) and the importance of the supercritical technology compared to other dissolution techniques (ionic liquids and hydrotropes) were highlighted and well discussed.

In this paper, a new hybrid method based on the adaptive neuro-fuzzy inference system (ANFIS) in combination with a PSO algorithm is applied for the first time in the phase equilibrium area to evaluate the ability of this approach for estimating the solubility of solid drugs in scCO₂, which includes: four methoxybenzoic acid isomers (naphthalene, 2-methoxybenzoic acid, 3-methoxybenzoic acid, 4-methoxybenzoic acid) [11], cholesterol [12], five phenol derivatives (p-nitrophenol, m-nitrophenol, 2,4 dinitrophenol, 2,5 dinitrophenol, and picric acid) [13], eight pharmaceutical drugs (ibuprofen, 5-fluorouracil, azodicarbonamide, thymidine, 2-phenyl-4H-1,3-benzoxazin-one, naproxen, taxol, and acetaminophen) [14], and penicillin [15]. Also, a control strategy is adopted and tested for the first time by using the inverse of the ANFIS method for estimating the critical properties of pure solid components. It is to mention that the reason for considering the ANFIS approach will be discussed in the next section.

Neuro-fuzzy system

Hybrid methods are widely used in many fields because of their high ability to adapt to various real-world problems and the possibility of combining more techniques in the modeling and optimization process.

ANFIS is an artificial intelligence method (AI) that combines artificial neural network networks and fuzzy inference systems (FIS). This method was first introduced by Jang [16].

As it was mentioned in the introduction section,

ANN has two main problems:

The learning process is slow.

Analysis of their optimized parameters is complex.

To correct the second problem, the fuzzy logic, which is good in explaining their behavior because fuzzy rules can be used successfully (where ANN is weak), but their capacity to acquire the knowledge is complex (where ANN is strong). This can make a neuro-fuzzy system a high predictive approach that takes advantage of both ANN and fuzzy logic. Also, the PSO algorithm, known as a good optimization tool, can surpass the first problem and enhance the learning ability of the ANFIS model.

This work applies the ANFIS technique with PSO in training drugs to estimate solid drugs' solubility in scCO₂. The choice of these solids is justified by the availability of the experimental solubility data in the literature and their biological and pharmaceutical interest.

Adaptive neuro-fuzzy inference system (ANFIS)

The ANFIS is Jang's hybrid neuro-fuzzy system developed in 1993 [R10]. ANFIS combines the fuzzification technique of fuzzy logic with the learning capability of ANN to facilitate the hybrid learning procedure [17]. The ANFIS architecture consists of five layers: fuzzified layer, artifact layer, standardized layer, de-fuzzified layer, and output layer. Each layer consists of a number of nodes that perform different operations according to the internal node function [18]. Based on a simple structure that considers two inputs and one output, the ANFIS with Takagi-Sugeno type is represented following Fig. 1.

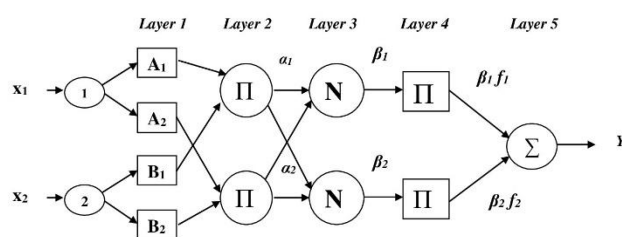


Figure 1. ANFIS architecture with two fuzzy rules.

A common two fuzzy if-then rules of the first-order Sugeno's type are as follows:

Rule 1: if $x_1 = A_1$ and $x_2 = B_1$ then $f_1(x_1, x_2) = a_{11}x_1 + a_{12}x_2 + b_1$

Rule 2: if $x_1 = A_2$ and $x_2 = B_2$ then $f_2(x_1, x_2) = a_{21}x_1 + a_{22}x_2 + b_2$

Layer 1: the primary purpose of the f layer is to map input variables into the fuzzy sets [18]. To represent the linguistic terms, the Gaussian member-

ship function is usually used [19]:

$$A_i(x) = \exp \left[-\frac{1}{2} \left(\frac{x - a_{i1}}{b_{i1}} \right)^2 \right] \quad (1)$$

$$B_i(x) = \exp \left[-\frac{1}{2} \left(\frac{x - a_{i2}}{b_{i2}} \right)^2 \right] \quad (2)$$

where, a_{i1} , b_{i1} , a_{i2} , and b_{i2} are the parameter set.

Layer 2: the output of each node in this layer is the product of all the incoming signals:

$$\alpha_1 = A_1(x_1) \times B_1(x_2) \quad (3)$$

$$\alpha_2 = A_2(x_1) \times B_2(x_2) \quad (4)$$

Layer 3: the label N in this layer indicates the normalization of the firing levels. The outputs of two neurons are the normalized firing level:

$$\beta_1 = \frac{\alpha_1}{\alpha_1 + \alpha_2} \quad (5)$$

$$\beta_2 = \frac{\alpha_2}{\alpha_1 + \alpha_2} \quad (6)$$

Layer 4: The output of this layer is the product of the normalized firing level and the individual rule output:

$$\beta_1 f_1 = \beta_1 (p_1 x_1 + q_1 x_2 + r_1) \quad (7)$$

$$\beta_2 f_2 = \beta_2 (p_2 x_1 + q_2 x_2 + r_2) \quad (8)$$

Layer 5: The single node in this layer computes the overall system output as the sum of all incoming signals:

$$Y = \beta_1 f_1 + \beta_2 f_2 \quad (9)$$

Solubility modeling using ANFIS-PSO

The modeling of the phase behavior of CO₂ (1)-solid drugs (2) binaries is performed using the ANFIS approach with the PSO algorithm for the training. The ANFIS was built as five inputs (the equilibrium temperature, T , the equilibrium pressure, P) and three pure component properties to differentiate between the solubility of different solid drugs (critical temperature, T_c , critical pressure, P_c , and the acentric factor, ω) and the solubility of the solid drugs in the SCF phase (y_2) as the output with five Gaussian membership functions for each input and five linear membership functions for the output. The first-order Sugeno fuzzy model was issued for generating the fuzzy rules. Figure 1 shows the ANFIS structure used in this study based on five lagged terms.

The experimental data used for developing the ANFIS-PSO model is divided into two sets: the first set is considered for training (it contains 66% of total data),

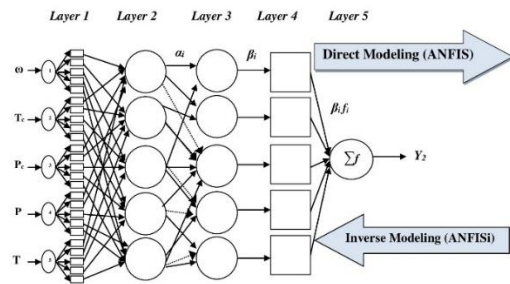


Figure 2. Direct and Inverse ANFIS structure for the prediction of the solubility of solid drugs.

Table 1. Critical properties of solid components used in this work

Components	Tc (K)	Pc (MPa)	ω	Ref.
Naphthalene	711.47 ^a	3.897 ^a	0.345	This work
2-Methoxybenzoic acid	808.95 ^a	3.90 ^a	0.764 ^c	This work
3-Methoxybenzoic acid	808.65 ^a	3.89 ^a	0.763 ^c	This work
4-Methoxybenzoic acid	808.35 ^a	3.92 ^a	0.762 ^c	This work
Cholesterol	1151.55 ^a	1.11 ^a	0.967 ^c	This work
Ibuprofen	749.7	2.33	0.819	[20]
5-Fluorouracil	807.42	6.22	0.64	This work
Azodicarbonamide	895.58	4.88	0.895	This work
Thymidine	924.21	3.64	0.886	This work
2-Phenyl-4H-1,3-benzoxazin-one	1009.69	3.64	0.746	This work
Naproxen	807	2.45	0.904	[20]
Taxol	1023.03	1.01	1.33	This work
Acetaminophen	817.72	4.43	1.11	This work
penicillin	902.78	2.355	1.325	[15]
m-nitrophenol	896.35	5.53	0.662	This work
p-nitrophenol	896.35	5.53	0.662	This work
2,4-dinitrophenol	914.1	4.91	0.827	This work
2,5-dinitrophenol	914.1	4.91	0.827	This work
Picricacid	998.08	4.8	0.982	This work

and the second set is used for the test and validation (it has 34% of total data). This distribution is the most efficient for good ANFIS-PSO training. Table 1 shows the pure component properties of the solid components considered in this work. It is to mention that these properties for Naproxen and Ibuprofen are taken from the literature [20].

For solid drugs, where no parameters are available in the literature, the Lee-Kesler correlation was applied by using the PE software [21] to determine the Pitzer's acentric factor of solutes. The critical temperature and critical pressure were estimated by the Nannoolal method [22] and the Gani group contribution method [23].

The calculation strategy is based on the variation of the training algorithms (considered a parameter to optimize with other parameters of the ANFIS model (the topology of the ANFIS model, membership function, the number of rules). The optimization of the ANFIS model parameters is performed by minimizing the objective function, which is an average absolute relative deviation (AARD %) defined as:

$$OF = AARD(\%) = \frac{100}{N} \sum_{i=1}^n \frac{|y^{calc} - y^{exp}|}{y^{exp}} \quad (10)$$

RESULTS AND DISCUSSION

The high nonlinearity is the characteristic of modeling the phase equilibrium. In this work, a comparative study was carried out between the new approach used in modeling solid solutes in $scCO_2$, i.e., the ANFIS trained with the PSO algorithm and the artificial neural network (ANN) trained with the PSO algorithm (trainps), the Levenberg-Marquardt algorithm (trainlm), and the basien radial algorithm (trainbr).

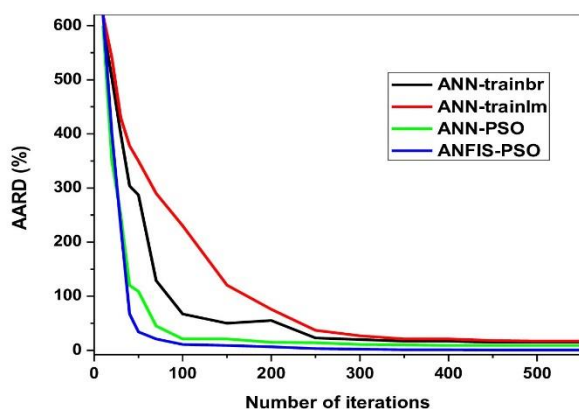


Figure 3. Comparison in terms of AARD % between training algorithms for training ANFIS and ANN models.

Figure 3 shows the superiority of the new approach in terms of the accuracy (lowest AARD) and the rapidity of the optimization process (lowest numbers of iterations) over the ANN model trained with the classical algorithms. Also, this study shows that the PSO training algorithm (trainps) can be used for optimizing the ANFIS model with more accuracy than the other selected training algorithms (train-GA, trainlm, and trainbr).

Based on the study mentioned above, the ANFIS-PSO model has proved its ability to estimate the solubility of solids in $scCO_2$ with more advantages than the ANN method. Table 2 gives a detailed comparison of the AARD% between the solubility calculated by the ANFIS-PSO model and those estimated by the different models reported in the literature to show the superiority of the new approach proposed for estimating solid solubility. The comparison shows that the ANFIS-PSO model predicts the solubility of solid components in $scCO_2$ with more accuracy than those obtained by the EOS and density-based models (global AARD% = 0.99).

Figure 4 gives the solubility curves as a function of pressure for Taxol in $scCO_2$. This graphical comparison allows concluding that the proposed model is suitable for modeling and representing the solid- $scCO_2$ binary equilibrium. Also, this figure shows a good agreement between the experimental and the predicted solubility.

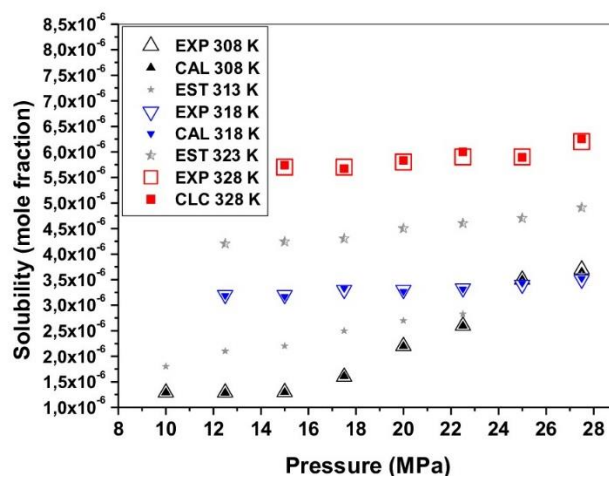


Figure 4. Experimental solubility of taxol in $scCO_2$ and that predicted by ANFIS-PSO model at various temperatures.

Determination of importance of each input variable

To evaluate the effect of each input variable on the output variable, the relative importance (I_j) was calculated using the Garson expression [24]. Figure 5 gives the relative importance of five inputs where the equilibrium temperature and pressure substantially af-

Table 2. Comparison of the AARD% of the predicted solubility of the solid drugs in $scCO_2$ obtained by ANFIS-PSO model and the literature results by some EOS and density-based models

SYSTEM	AARD%							
	ANFIS-PSO	Chrastil	VR-SAFT	Bartle	MT	PR	DVA	SRK
Naphthalene	1.25	NR	NR	NR	NR	13.4	NR	14.8
2-Methoxybenzoic acid	0.97	8.20	NR	NR	NR	NR	NR	NR
3-Methoxybenzoic acid	1.13	2.67	NR	NR	NR	NR	NR	NR
4-Methoxybenzoic acid	1.11	6.97	NR	NR	NR	NR	NR	NR
Cholesterol	1.05	4.37	10.40	6.3	3.44	NR	4.54	NR
Ibuprofen	1.23	6.72	8.80	8.9	3.99	NR	8.30	NR
5-Fluorouracil	0.54	6.50	NR	NR	NR	NR	NR	NR
Azodicarbonamide	1.22	10.21	NR	NR	NR	NR	NR	NR
Thymidine	0.98	11.45	NR	NR	NR	NR	NR	NR
2-Phenyl-4H-1,3-benzoxazin-one	1.00	5.50	NR	NR	NR	NR	NR	NR
Naproxen	0.40	3.50	NR	NR	NR	12.1	NR	11.5
Taxol	0.58	4.55	NR	NR	NR	NR	NR	NR
Acetaminophen	1.22	4.03	NR	NR	NR	NR	NR	NR
Penicillin	0.45	32.4	NR	22.9	NR	NR	32.4	NR
m-nitrophenol	1.40	9.42	NR	NR	NR	NR	NR	NR
p-nitrophenol	1.12	11.36	NR	NR	NR	NR	NR	NR
2,4-dinitrophenol	0.40	13.40	NR	NR	NR	NR	NR	NR
2,5-dinitrophenol	1.30	10.52	NR	NR	NR	NR	NR	NR
Picric acid	1.53	6.70	NR	NR	NR	NR	NR	NR
Total	0.99	8.80	9.60	12.7	3.71	12.75	15.08	13.15

^a NR= Not Reported.

fect the solid solubility value with importance equal to 31% and 28%, respectively

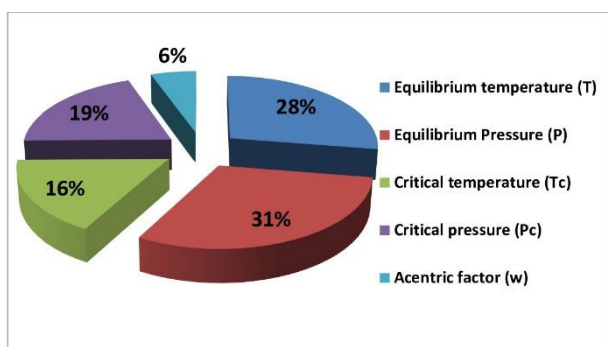


Figure 5. Relative importance (%) of input variables on the value of the calculated solubility (y_2).

Optimal performance by mean of ANFISi

According to the ANFIS model, it is possible to simulate the system performance when the input parameters are well known, and the model parameters

are well optimized. The mathematical formula that connects the selected input variables to the output (solid solubility) in the optimized ANFIS-PSO model is given as follow:

$$y_2 = \sum_{i=1}^k y_i(x)(a_i x_i + b_i) \quad (11)$$

with:

$$y_i(x) = \frac{\prod_{j=1}^p \exp\left(-\frac{(x_j - c_{ij})^2}{2\delta_{ij}^2}\right)}{\sum_{i=1}^k \prod_{j=1}^p \exp\left(-\frac{(x_j - c_{ij})^2}{2\delta_{ij}^2}\right)} \quad (12)$$

where, $p = 1.. .5$, and $j = 1.. .5$.

The INFISi approach is a method that can be used for estimating the input parameters from the output. Some of those parameters (critical properties) are not available in the literature, or there are no predictive methods to calculate them with acceptable accuracy. At

this step, the optimized ANFIS model provides the nonlinear equation:

$$Fun(x) = y_2 - \frac{\sum_{i=1}^k \prod_{j=1}^p \exp\left(-\frac{(x_j - c_{ij})^2}{2\delta_{ij}^2}\right)}{\sum_{i=1}^k \prod_{j=1}^p \exp\left(-\frac{(x_j - c_{ij})^2}{2\delta_{ij}^2}\right)} (a_i x_i + b_i) \quad (13)$$

This equation has to be minimized at zero to get the optimal input parameters where the optimization of equation (13) is classified as a constrained multivariable nonlinear optimization problem.

A set of the parameters are available for the inputs estimation process. When we introduce the value of the optimized ANFIS model, equilibrium temperature, and pressure, the other unknown parameters (critical temperature, critical pressure, and acentric factor) will be estimated using the optimization process.

Following the same strategy applied in section (4), the ability of major optimization algorithms was tested in estimating the ANFISi model, where a comparative study was carried out among a set of optimization algorithms.

The evaluation in terms of the AARD shows that the most efficient algorithm for the input parameters estimation is the PSO algorithm (Figure 6).

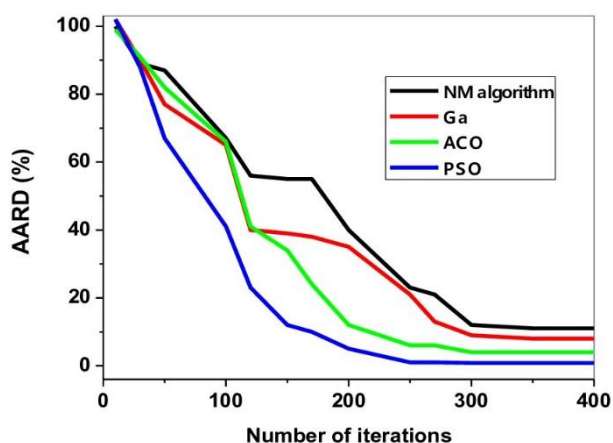


Figure 6. Comparison in terms of AARD % between optimization algorithms (ACO, PSO, Ga and Nelder-Mead) for estimating input parameters using ANFISi.

The comparison between the experimental and calculated values of the input parameters using ANFISi is performed in terms of AARD_x:

$$AARD_x (\%) = \frac{100}{n} \sum_{i=1}^n \frac{(x_i^{calc} - x_i^{exp})}{x_i^{exp}} \quad (14)$$

Estimation of critical properties by the interpolating method

The ANFISi approach developed has reproduced the critical properties from the experimental data with good precision (the AARD (%) calculated are 0.85, 0.75, and 0.60 for the critical temperature, critical pressure, and acentric factor, respectively).

In this part, an extrapolating test is carried out to predict the acentric factor, critical temperature, and pressure from the experimental solubility data of the solid components found in the literature, which were not used in the development of the ANFIS model. Because this work has a point to evaluate the promising heuristic techniques' ability to represent the phase equilibria reliability, the ANFISi was compared to the ANNi method developed previously in terms of the average relative deviation (AARD%) for estimating the properties of the pure components. Figure 7 shows that the ANFISi can estimate both critical temperature and pressure far away than the ANNi.

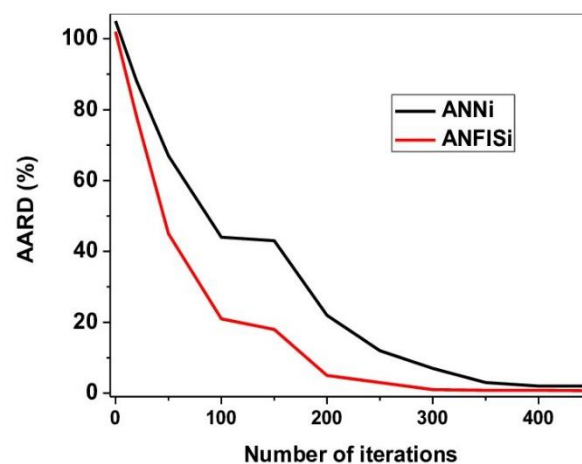


Figure 7. Comparison in terms of AARD between ANNi and ANFISi methods for estimation critical pressure of solid solutes.

Using the PSO algorithm for the multivariable optimization process, the estimated values of the properties mentioned above for other classes of solids are shown in Table 3. This contains a comparison between the estimated properties with the new method and those calculated with the classical GCM method found in the literature [25-38]. Table 3 shows that the critical properties and the acentric factor calculated with the inverse ANFIS approach have the same orders of magnitude, which suggests a good extrapolating ability of the ANFISi. In addition, this approach is more advantageous than the group contribution methods, which needed the ebullition temperature and the structure of molecules for calculating such properties. The complicated process used with these methods may

add a factor of inaccuracy for the calculated critical properties [39].

Table 4 gives the AARD (%) values evaluated between the experimental data and the solubility calculated by

the PR, SRK, and Pazuki equations of state using critical properties estimated in this work using the ANFISi and those calculated with the same equations of state reported in the literature.

Table 3. Comparison between critical properties estimated by ANFISi approach and those found in literature

Component	Critical properties						Ref.
	This work			Literature			
	T_c	p_c	w	T_c	p_c	w	
Amiodarone hydrochloride	989.6	10.50	0.41	1040.4	11.75	0.430	[25]
Curcumin	432.5	22.20	1.35	419.9	22.50	1.551	[26]
Anthraquinone	977.3	31.76	1.03	987.05	31.28	1.015	[27]
1,4 bisethylamino (Anthraquinone)	955.2	22.40	1.11	945.34	21.03	1.142	[27]
1-Amino4-hydroxyanthraquinone	933.2	33.20	0.93	921.01	30.68	0.982	[27]
1-Hydroxy 4-nitro anthraquinone	919.7	28.5	1.01	913.95	27.74	1.046	[27]
1-Amino anthraquinone	901.2	30.33	0.85	928.10	31.42	0.853	[28]
1-nitro anthraquinone	933.3	28.40	0.90	916.60	28.10	0.921	[28]
Photochomicdye	785.1	24.20	0.89	-	-	-	[29]
Ibuprofen	763.5	22.90	0.89	749.70	23.30	0.819	[30]
Ferulic acid	846.5	36.78	1.10	854.60	36.40	1.194	[31]
Pyridin 4-amine	887.2	23.50	0.95	-	-	-	[32]
Fluvaxamine maleate	747.3	55.20	0.41	-	-	-	[33]
Flavanone	867.8	32.57	0.74	879.90	32.80	0.728	[34]
Tangeritin	1034.2	26.89	0.98	1139.1	26.66	1.107	[34]
Nobiletin	1178.4	25.94	1.09	1256	26.60	1.228	[34]
6-Hydroxyflavanone	998.5	33.50	0.88	1062.5	35.40	0.914	[34]
7-Hydroxyflavanone	1000.1	37.59	0.98	1074.2	37.81	0.952	[34]
Protocatechuic	861.3	54.50	0.89	869.29	55.33	0.984	[35]
Crysin	954.7	30.20	0.98	966.90	31.15	1.175	[35]
Sinapic acid	904.5	27.80	0.91	927.62	28.06	0.973	[35]
Menadione	624.4	45.88	0.69	639.58	46.53	0.623	[36]
Dichlone	744.2	65.04	0.67	731.96	64.10	0.639	[36]
Aprepitant	888.9	21.50	0.90	895.60	20.18	0.810	[37]
A-Tocopherol	888.5	45.30	0.525	-	-	-	[37]
dM2B	989.9	23.45	0.88	1144.11	24.46	1.015	[38]
dM3P	995.4	21.9	1.10	1161.46	22.29	1.051	[38]

Table 4. AARD evaluated between experimental solubility and that calculated with different models

Component	AARD (%) ^a			AARD (%) ^b		
	PR-EOS	SRK-EOS	Paz-EOS	PR-EOS	SRK-EOS	Paz-EOS
Amidarone	4.20	4.35	3.46	6.03	NR	8.88

Table 4. AARD evaluated between experimental solubility and that calculated with different models (Continued)

Component	AARD (%) ^a			AARD (%) ^b		
	PR-EOS	SRK-EOS	Paz-EOS	PR-EOS	SRK-EOS	Paz-EOS
Curcumin	7.33	7.87	5.34	50.5	NR	NR
Anthraquinone	5.25	5.97	3.67	7.60	8.40	NR
1,4 bisethylelim	3.44	4.42	5.60	13.10	NR	NR
Photochomicdye	6.50	7.39	5.33	12.30	13.1	NR
Ibuprofen	7.29	6.50	3.30	9.70	9.95	NR
Ferulic acid	8.11	7.14	6.47	50.9	NR	NR
Pyridin 4-amine	5.55	4.67	4.95	NR	NR	NR
Fluvaxamine maleate	5.30	5.02	6.11	63.43	NR	NR
Flavanone	0.99	1.33	1.56	1.90	NR	NR
Tangeritin	1.32	5.44	4.65	1.77	9.50	NR
Nobiletin	1.20	1.01	3.45	0.98	NR	NR
6-Hydroxyflavanone	2.11	1.32	1.22	1.72	NR	NR
7-Hydroxyflavanone	3.77	2.25	3.34	1.14	NR	NR
Protocatechuic	5.70	5.93	2.12	5.60	NR	NR
Crysin	2.00	1.87	2.22	2.30	NR	NR
Sinapic acid	6.80	4.41	3.78	18.50	NR	NR
Menadione	4.33	3.89	5.42	8.27	NR	NR
Dichlone	4.20	4.43	6.43	9.03	NR	NR
Aprepitant	5.43	6.16	6.66	9.08	9.23	NR
A-Tocopherol	5.55	4.78	5.09	NR	NR	NR
1-Amino4-hydroxyanthraquinone	6.73	7.88	5.44	13.60	NR	NR
1-Hydroxy4-nitro anthraquinone	9.88	8.55	5.54	8.20	NR	NR
1-Amino anthraquinone	3.45	4.44	6.12	10.50	NR	NR
1-nitro anthraquinone	3.23	3.87	4.44	13.10	NR	NR
dM2B	5.21	4.98	3.77	9.85	NR	NR
dM3P	3.85	3.44	2.43	7.33	NR	NR

^a AARD (%) evaluated between experimental data and solubility calculated by PR, SRK and Pazuki equations of state using critical properties estimated in this work (ANFISi). ^b AARD (%) evaluated between experimental data and solubility calculated by PR, SRK and Pazuki equations of state reported in the literature. NR= Not Reported.

CONCLUSION

In this work, a new method that combines ANN and FIS has been used for developing a model to predict the solubility of solids in scCO₂. The estimation results show that the ANFIS-PSO model can predict the solid solubility far better than the ANN-PSO model and the classical models with the AARD value equal to 0.99 %. Also, the comparative study shows that the PSO algorithm was more advantageous in training, test, validation, and optimization problems. Therefore, the new approach shows the high predictive and interpolating abilities at temperatures where no

experimental data was found in the literature.

The second valuable contribution was developing an efficient method for reproducing the input parameters by an inverse FIS. The ANFISi was used first to reproduce the critical properties of the solids used for developing the ANFIS-PSO model to test the validity of this approach and then estimate the critical parameters for another set of solid drugs (extrapolation test). The results show that the ANFISi method can be a promising technique and a good alternative to the GCM method in estimating the critical properties of solid drugs. Also, ANFISi has facilitated the perfor-

mance of estimating the solubility of the solid using the EOS equations compared to the experimental data.

List of symbols

AARD	Average absolute relative deviation
ACO	Ant colony optimization
AI	Artificial intelligence
ANN	Artificial neural network
ANNi	Inverse artificial neural network
ANFIS	Adaptive neuro-fuzzy inference system
ANFISi	
a_{ij}, b_{ij}	Gaussian membership function parameters
br	Bazian regularization
DVA	Del Var Aguilera equation of state
FIS	Fuzzy interference system
I	Relative importance
GA	Genetic algorithm
GCM	Group contribution method
Im	Levenberg-Marquardt
NM	Nelder-Mead optimization algorithm
T	Equilibrium temperature (K)
T_c	Critical temperature (K)
P	Pressure (MPa)
P_c	Critical pressure (MPa)
PE	Phase equilibria
PR	Peng-Robinson
PSO	Particle swarm optimization
SRK	Soave-Redlich-Kwong
VR-SAFT	Variable ranged statistical associating fluid theory
α	Firing strength
β	Normalized firing level
ω	Acentric factor
y_2	Solubility of solid drugs
Superscripts	
calc	Calculated property
exp	Experimental property
o	Output
Subscripts	
2	Solute (solid)
c	critical property

REFERENCES

- [1] J.C. Rojas-Thomas, M. Mora, S. Santos, *Neural Comput. Appl.* 31 (2019) 2311-2327.
- [2] S.K. Ashan, M.A. Behnajady, N. Ziaieifar, *Neural Comput. Appl.* 29 (2018) 969-979.
- [3] M. Khayet, C. Cojocar, *Desalination* 308 (2013) 102-110.
- [4] B. Gülçin, G. Sezin, *Energy* 123 (2017) 149-163.
- [5] M. Laidi, S. Hanini, Rezrazi A, M.R. Yaiche, A. Abdallah el Hadj, F. Chellali, *Theor. Appl. Climatol.* 128 (2017) 439-451.
- [6] A. Abdallah El Hadj, C. Si-Moussa, S. Hanini, M. Laidi, *Chem. Ind. Chem. Eng. Q.* 19 (2013) 449-460.
- [7] M. Velibor, *Chem. Ind. Chem. Eng. Q.* 26 (2020) 309-319.
- [8] Y. Jewajinda, P. Chongstitvatana, *Neural Comput. Appl.* 22 (2013) 1609-1626.
- [9] R. Fuller, H.J. Zimmermann, in *Proceedings of 2nd International Workshop on Current Issues in Fuzzy Technologies*, University of Trento, Trento, May 28-30 (1993) 45-54.
- [10] A. Abdallah El Hadj, M. Laidi, C. Simoussa, S. Hanini, *Neural Comput Appl.* 28 (2017) 87-99.
- [11] J.W. Chen, F.N. Tsai, *Fluid Phase. Equilib.* 107 (1995) 189-200.
- [12] F.E. Wubolts, O.S.L. Bruinsma, G.M. Van Rosmalen, *J. Supercrit. Fluids* 32 (2004) 79-87.
- [13] M. Shamsipur, F. Reza, Y. Yamini, A.R. Ghiasvand, *J. Supercrit. Fluids* 23 (2002) 225-231.
- [14] S. David, L.A. Estévez, J.C. Pulido, J.E. Garcia, M. Carmen, *J. Chem. Eng. Data* 50 (2005) 1234-1241.
- [15] M.D. Gordillo, M.A. Blanco, A. Molero, E. Martinez de la Ossa, *J. Supercrit. Fluids* 15 (1999) 183-190.
- [16] J.S.R. Jang, *IEEE Trans. Syst. Man. Cybern.* 23 (1993) 665-685.
- [17] A.R. Fallahpour, A.R. Moghassem, *J. Eng. Fibers Fabr.* 8 (2013) 6-18.
- [18] R. Kamali, A.R. Binesh, *Microfluid. Nanofluid.* 14 (2013) 575-581.
- [19] R. Babuska, *Neuro-Fuzzy Methods for Modeling*, In *Recent Advances in Intelligent Paradigms and Applications*, A. Abraham, L.C. Jain, J. Kacprzyk, Springer-Verlag, Heidelberg (2002), pp 161-186.
- [20] P. Coimbra, C.M. Duarte, H.C. de Sousa, *Fluid Phase Equilib.* 239 (2006) 188-199.
- [21] O. Pfohl, S. Petkov, G. Brunner, *High-pressure fluid-phase equilibria containing supercritical fluids*, In *8th International Conference on properties and Phase Equilibria for Product and Process Design*, Noordwijkerhout, Netherlands, April 26-May (1998).
- [22] Y. Nannoolal, J. Rarey, D. Ramjugernath, *Fluid Phase Equilib.* 269 (2008) 117-133.
- [23] J. Marrero, R. Gani, *Fluid Phase Equilib.* (183-184) (2001) 183-208.
- [24] G.D. Garson, *Interpreting Neural Network Connections weights*, *AI Expert: Miller Freeman, Inc. San Francisco* (1991), p. 46.
- [25] G. Sodeifian, S.A. Sajadian, F. Razmimanesh, *Fluid Phase Equilib.* 25 (2017) 149-159.
- [26] P.C. Larissa, M.C. Acosta, C. Turner, *J. Supercrit. Fluids*

- 130 (2017) 381-388.
- [27] K. Tamura, R.S. Alwi, Dyes Pigm. 113 (2015) 351-356.
- [28] R.S. Alwi, T. Tanaka, K. Tamura, J. Chem. Thermodyn. 74 (2014) 119-125.
- [29] P. Coimbra, M.H. Gil, C.M.M. Duarte, B.M Heron, H.C. de Sousa, Fluid Phase Equilib. 238 (2005) 120-128.
- [30] A. Mehdi, M. Mehrdad, Z. Fatemeh, Chin. J. Chem. Eng. 22 (2014) 549-558.
- [31] G.R. Bitencourt, F.A. Cabral, A. Meirelles, J. Chem. Thermodyn. 103 (2016) 285-291.
- [32] C. Chun-Ta, L. Chen-An, T. Muoi, Y.P. Chen, J. CO₂ Util. 18 (2017) 173-180.
- [33] Y. Khayyat, S.M. Kashkoui, F. Esmailzadeh, Fluid Phase Equilib. 399 (2015) 98-104.
- [34] M. Ota, M. Sato, Y. Sato, L.S.J. Richard, H. Inomata, J. Supercrit. Fluids 128 (2017) 166-172.
- [35] J.P. Paulaa, I.M.O. Sousab, M. Foglioc, F. Cabral, J. Supercrit. Fluids 112 (2016) 89-94.
- [36] A.G. Reveco-Chilla, A.L. Cabrera, J.C. de la Fuente, F.C. Zacconi, J.M. del Valle, L.M. Valenzuela, Fluid Phase Equilib. 42 (2016) 84-92.
- [37] G. Sodeifian, S. Sajadian, N.S. Ardestani, J. Supercrit. Fluids 128 (2017) 102-111.
- [38] F.C. Zacconi, O.N. Nuñez, A.L. Cabrera, L.M. Valenzuela, J.M. del Valle, J.C. de la Fuente, J. Chem. Thermodyn. 103 (2016) 325-332.
- [39] E. Potrich, F.A.P. Voll, V.F. Cabral, L. Cardozo Filho, Chem. Ind. Chem. Eng. Q. 25 (2019) 153–162.

ABDALLAH ABDALLAH EL
HADJ ^{1,2},
MAAMAR LAIDI ²
SALAH HANINI ²

¹ Faculty of Science, University
Saad Dahleb of Blida 1, Blida,
Algeria

² Laboratory of BioMaterial and
transfer Phenomena (LBMP),
University of Medea, Medea,
Algeria

NAUČNI RAD

NOVA METODA ZASNOVANA NA NEURO-FAZI SISTEMU I PSO ALGORITMU ZA PROCENU KARAKTERISTIKA FAZNE RAVNOTEŽE

Predmet ovog rada je predlaganje nove metode zasnovane na ANFIS sistemu i PSO algoritmu za osmišljavanje modela za procenu rastvorljivosti čvrstih lekova u natkritičnom CO₂. Visoki nelinearni proces je modelovan neuro-fazi pristupom (NFS). PSO algoritam je korišćen u dve svrhe: za zamenu standardne propagacije unazad u obuci NFS-a i optimizacija procesa. Strategija validacije je sprovedena korišćenjem analize linearne regresije i upoređenjem predviđenih sa eksperimentalnim podacima. ANFIS pristup je upoređivan sa ANN u smislu tačnosti. Statistička analiza predvidljivosti optimizovanog modela obučenog PSO algoritmom (ANFIS-PSO) pokazuje bolje slaganje sa referentnim podacima od ANN metode. Štaviše, poređenje u smislu AARD devijacije (%) između predviđenih rezultata, rezultata predviđenih modelima zasnovanim na gustini i skupa jednačina stanja pokazuje da ANFIS-PSO model daleko bolje korelira rastvorljivost čvrstih lekova u natkritičnom CO₂. Takođe, po prvi put je razvijena kontrolna strategija u oblasti fazne ravnoteže korišćenjem neuro-fazi inverznog pristupa (ANFISi) za procenu svojstava čistih komponenti iz podataka o rastvorljivosti bez prolaska kroz GCM metode.

Ključne reči: modelovanje, ANFIS, veštačke neuronske mreže, kritična svojstva, optimizacija rojem čestica.

FADIME BEĞÜM TEPE ¹
TOLGA KAĞAN TEPE ¹
AYTEN EKİNCİ ²

¹ Department of Food
Technology, Şebinkarahisar
Vocational School of Technical
Science, Giresun University,
Giresun, Turkey

² Department of Food
Technology, Denizli Vocational
School of Technical Science,
Pamukkale University, Denizli,
Turkey

SCIENTIFIC PAPER

UDC 66.057:547.475.2:634.6

IMPACT OF AIR TEMPERATURE ON DRYING CHARACTERISTICS AND SOME BIOACTIVE PROPERTIES OF KIWI FRUIT SLICES

Article Highlights

- The drying rate of kiwifruits was highly influenced by drying temperature
- The parabolic model was determined to best predict the experimental moisture ratio
- Effective diffusion coefficient showed an increment with the increasing drying temperature
- AAC, TPC, and AC of fresh kiwifruits were determined higher than dried fruits
- L and b values of kiwifruits decreased during the drying process, unlike increased values

Abstract

Drying kinetics, ascorbic acid content (AAC), total phenolic content (TPC), and antioxidant capacity (AC) of kiwifruits at different temperatures (60 °C, 70 °C, and 80 °C) were investigated. The drying rate and effective moisture diffusivity of kiwifruits were the highest at 80 °C. Additionally, the Parabolic model best predicts the experimental moisture ratio at 60 °C and 70 °C, while the Page model described the drying curve at 80 °C. On the other hand, the AAC, TPC, and AC of kiwifruits were significantly influenced by temperature. Degradation of AAC increased with the increment in temperature, while TPC and AC were higher at the higher temperature. The range of the AAC, TPC, and AC of fresh and dried fruits were 165.59±12.58-462.81±11.53 mg/100 g DW, 747.66±16.09-1846.87±15.52 mg/100 g GAE DW, and 0.283±0.15-1.903±0.15 mmol TE/100 g DW, respectively. The highest AAC, TPC, and AC losses were calculated as 64.22%, 59.43%, and 85.13%, respectively.

Keywords: ascorbic acid, antioxidant capacity, drying kinetics, kiwifruit.

The reduction of degenerative diseases, cardiovascular diseases, and cancer has been partially related to fruit and vegetable consumption. Several studies have shown that this relation results from antioxidant compounds, reducing oxidative stress caused by free radicals [1-3]. The antioxidant compounds have free radical scavenging ability by inhibiting initiation and preventing chain propagation, suppressing the free radical formation that makes bonds with metal ions, reducing hydrogen peroxide, and quenching superoxide and singlet oxygen. Thus,

antioxidant compounds preserve the human body from oxidative stress. Antioxidants naturally found in fruits and vegetables, such as ascorbic acid and phenolic compounds [1-5]. Ascorbic acid, one of the most important food components in fruits and vegetables, is a strong antioxidant, but it is quite a thermo-sensitive compound [5, 6]. Generally, the assumption of well retained ascorbic acid in foods indicates higher retention of other nutritional compounds at the end of the process. Thus, ascorbic acid is frequently analyzed as an indicator to demonstrate the effect of the process [6].

Additionally, ascorbic acid prevents N-nitroso compounds derived from nitrates or nitrites and is responsible for cancer [5]. On the other hand, phenolic compounds, which are secondary metabolites of plants, are strong antioxidants [7]. Therefore, the phenolic compounds play an important role in human health with the anti-inflammatory and anti-oxidative effects that

Correspondence: T.K.Tepe, Department of Food Technology, Şebinkarahisar Vocational School of Technical Science, Giresun University, Giresun, Turkey.

E-mail: tolga.kagan.tepe@gmail.com

Paper received: 26 January, 2021.

Paper revised: 12 June, 2021.

Paper accepted: 16 July, 2021.

<https://doi.org/10.2298/CICEQ210126026T>

boost the immune system and prevent cancers and cardiovascular diseases [8, 9].

Kiwifruits originated in China have been recently cultivated in the Black Sea region of Turkey. Due to its health-promoting effect by high ascorbic acid and phenolic compounds, kiwifruit is considered a high nutritional fruit [10, 11]. Kiwifruits show antioxidant activity and have anti-inflammatory effects and prevention effects on cancer, hypolipidemia in vivo experiments, cure nephrotoxicity, and chemically-induced toxicity [12-16]. Due to these properties, kiwifruits, called 'healthy fruit,' are a promising fruit species with high commercial potential and increasing production worldwide [8,9]. On the other hand, following the fully ripening, kiwifruits have a very short shelf life because of being perishable [10,11,17]. Some preservation methods can be suggested to prevent short shelf life, such as drying.

Dehydration, one of the oldest preservation methods of foods, is an effective method to preserve fruits after harvest and reduce food quality losses [18-20]. Dehydration, also called drying, aims to reduce moisture content and water activity, to prevent deterioration based on microbiological spoilage, to stop or slow down enzymatic activity and chemical reaction, to extend shelf life and make lower costs of transportation and storage as well as new ways of consumption [19, 21-27]. On the other hand, the drying process for a long time may cause some quality losses such as degradation of vitamins, phenolic compounds, unfavorable flavor, and color changes, or losses of essential amino acids [27,28].

Hot-air drying is the most common drying technique due to its simplicity and easiness to control [29, 30]. However, hot-air drying has several issues such as long drying time and high energy consumption at a lower temperature, loss of product quality at higher temperatures, and reduction in rehydration ability [30, 31]. Some authors reported a reduction in the nutritional value of kiwifruits by hot-air drying. It was stated that the content of ascorbic acid and phenolic compounds of kiwifruits was considerably reduced by hot-air drying [6]. Likewise, Akar and Mazı [32] reported that total lower phenolic content of kiwifruits was remarkably found in hot-air dried kiwifruits compared to fresh samples. In another study, vitamin C, total phenolic content, and antioxidant activity of fresh kiwifruits significantly decreased during hot-air drying. Besides, a higher drying temperature causes a higher reduction ratio [5].

Most of the current literature focused on drying kinetics of kiwifruits with different methods. However, a few of them mention the degradation of nutritional

components of kiwifruits during drying. In summary, degradation of these important compounds that provide 'being regarded as healthy fruit' needs further data besides drying kinetics. In the study, hot-air drying was selected as it is the most preferred drying method. In this context, the study aimed to determine the drying characteristics of kiwifruit slices at different air temperatures and the impact on the ascorbic acid content (AAC), total phenolic content (TPC), and antioxidant capacity (AC) of fresh and dried kiwifruit slices.

MATERIALS AND METHODS

Materials

Sample preparation

Fresh kiwifruits (*Actinidia deliciosa* cv. Hayward) were provided from a local market in Denizli, a province in Turkey. Fresh kiwifruits were washed, removed from foreign materials, and cut into 5 ± 0.5 mm slices. Determination of initial moisture content of samples was carried out in a drying oven at 105 °C till any sample weight changed. The initial moisture content of kiwifruits was $84.02\pm 0.4\%$.

Methods

Drying experiment

A cabinet dryer (Yücebas, Makine Ltd. Inc., Izmir, Turkey.) was used for drying experiments. Before drying, the cabinet dryer was turned on for approximately 30 min for stability. The samples (50 g) were weighed on a drying tray and placed in the cabinet dryer for each drying experiment. Drying processes were performed at 60 °C, 70 °C, and 80 °C. Besides, the air velocity and relative humidity were 2 m s^{-1} and 20%, respectively. Samples were taken out and weighed at intervals with a digital weight measure with 0.01 g precision during the drying process. The drying experiments were continued until the moisture content of samples achieved 7% on a wet basis (WB). All the drying experiments were performed in duplicate.

Thin-layer drying modeling of drying data

Thin-layer drying modeling of drying is a necessary procedure to design the best drying conditions. In the current study, thin-layer drying models, the most used mathematical equations in the drying process, were used. These equations provide important information about drying temperature and time [33].

Eq. (1) was used for calculation of moisture ratio (MR) of kiwifruit slices:

$$MR = \frac{M_t - M_e}{M_i - M_e} \quad (1)$$

where M_i , M_t , and M_e are the initial moisture content, moisture content at any time, and equilibrium moisture content of samples, respectively. When compared to M_t and M_0 , M_e was equal to zero and negligible according to the previous reports [34,35]. All moisture contents were indicated on dry matter (g g^{-1} dry matter).

Eq. (2) was used for the determination of drying rate (DR):

$$DR = \frac{M_{t+\Delta t} - M_t}{\Delta t} \quad (2)$$

where $M_{t+\Delta t}$ represents moisture content at time difference Δt is the difference of time between two measuring points.

The determination coefficient (R^2), root mean square error (RMSE), and reduced chi-square (χ^2) were the statistical parameters that explain the relation between predicted and experimental data of kiwifruit slices dried at various air temperatures. The RMSE expresses the deviation between the predicted and experimental values. The lower values of χ^2 and RMSE and a higher value of R^2 are required to determine the best equation predicting experimental data. The R^2 (Eq. 3), RMSE (Eq. 4), and Chi-Square (χ^2) (Eq. 5) values were calculated as follows:

$$R^2 = 1 - \frac{\sum (MR_{\text{exp}} - MR_{\text{pre}})^2}{\sum (MR_{\text{exp}} - MR_{\text{exp,avr}})^2} \quad (3)$$

$$RMSE = \left[\frac{1}{N} \sum_{i=0}^N (MR_{\text{pre},i} - MR_{\text{exp},i})^2 \right]^{1/2} \quad (4)$$

$$\chi^2 = \frac{\sum_{i=0}^N (MR_{\text{pre},i} - MR_{\text{exp},i})^2}{N - n} \quad (5)$$

$MR_{\text{pre},i}$ is the predicted MR of mathematical models, $MR_{\text{exp},i}$ is the experimental MR, $MR_{\text{exp,avr}}$ is the average of the experimental MR, N is the number of observation data, and n is the constants of the thin-layer drying models. [33,36,37]. The process modeling of kiwifruit slices drying was determined using MATLAB software (R2015a, version 8.5) non-linear curve fitting toolbox with the trust-region algorithm.

Determination of effective moisture diffusivity and activation energy in hot-air drying

Fick's second law was used to determine effective moisture diffusivity as suggested in the papers on drying foods [24, 33, 38]. Crank [39] proposed Fick's second law for infinite slab objects

with constant moisture diffusivity as Eq. (6):

$$MR = \frac{8}{\pi^2} \sum_{n=1}^{\infty} \frac{1}{(2n+1)^2} \exp\left(- (2n+1)^2 \pi^2 \frac{D_{\text{eff}} t}{4L^2}\right) \quad (6)$$

Effective moisture diffusivity (D_{eff}) was calculated with Eq. (6) as kiwifruit slices were assumed as infinite slab material. In Eq. (6), D_{eff} represents the effective moisture diffusivity ($\text{m}^2 \text{s}^{-1}$ or $\text{m}^2 \text{min}^{-1}$), and L is the half-thickness of the initial size of the sample before drying (m). For simplicity, Eq. (6) can be further simplified to only the first term of the series. Thus, Eq. (6) is written in a logarithmic form as follows [24,33]:

$$\ln(MR) = \ln\left(\frac{8}{\pi^2}\right) - \left(\frac{\pi^2}{4L^2} D_{\text{eff}} t\right) \quad (7)$$

The plot of $\ln(MR)$ versus time (Eq. 7) is a straight line with a slope as follows [33, 35]:

$$\text{Slope} = \frac{\pi^2}{4L^2} D_{\text{eff}} \quad (8)$$

Activation energy is calculated by the Arrhenius equation in the hot-air drying process as given by Eq. (9) [33]:

$$D_{\text{eff}} = D_0 \exp\left(-\frac{E_a}{RT}\right) \quad (9)$$

where R is the universal gas constant ($8.314 \text{ J mol}^{-1}\text{K}^{-1}$ or $1.987 \text{ cal mol}^{-1}\text{K}^{-1}$), T represents absolute temperature, E_a is the activation energy (kJ mol^{-1} or kcal mol^{-1}) and D_0 is the pre-exponential constant ($\text{m}^2 \text{s}^{-1}$) [33, 34]. After regulation of Eq. (9), a new equation is derived by transforming Eq. (9):

$$\ln D_{\text{eff}} = \ln D_0 - \frac{E_a}{RT} \quad (10)$$

Natural logarithm of effective moisture diffusivity versus $1/T$ gives a straight line with a slope representing activation energy:

$$\text{Slope} = \frac{E_a}{R} \quad (11)$$

Analysis of AAC

Extraction of AAC was performed according to Dönmez [40]. Each sample (5 g) was weighed and homogenized with distilled water with a ratio of 1:9 (w/v) using a laboratory-type blender. The homogenized samples were centrifugated at 4500 rpm for 10 min (Nüve NF800R), the supernatants were taken and filtrated through a $0.45 \mu\text{m}$ filter before the injection into the HPLC. Each AAC analysis was performed in duplicate.

A microsyringe was used to inject $20 \mu\text{l}$ of the last filtrate into the HPLC column. Mobil phase consisted of

0.01N H₂SO₄, which is HPLC purity. A HPLC device (SHIMADZU), column oven at 25 °C (SHIMADZU CTO-20A), Column Coregel 87H3 (7.8x300 mm), pump (SHIMADZU LC-20AD), degasser (SHIMADZU DGU-20A3), photo diode array (PDA) detector (SPD-M20A) at 254 nm were used for analysis. The mobile phase was isocratic with a 1 ml min⁻¹ flow rate.

AAC was calculated using an equation obtained from a calibration curve consisting of different concentrations of stock solutions (50, 100, 250, 500, 750, and 1000 ppm) with a high R² (0.9999). Results were expressed mg/100g in dry weight (DW).

Analyzes of TPC and AC

Analyzes of TPC and AC were performed with methanolic extraction suggested by Otağ [41]. 5 g kiwifruit samples were homogenized with 45 ml of 90% methanol through a laboratory-type blender. After centrifugation at 4500 rpm for 10 min, the supernatants were collected and filtrated using filter paper.

The method of Singleton and Rossi [42] was used to analyze TPC with a slight modification. Firstly, 300 µl of extract and 1500 µl of Folin-Ciocalteu solution (%10 v/v) were mixed and kept in the dark for 3 min. After 3 min, 1200 µl of aqueous Na₂CO₃ was added to the mixture. Then, the mixture was incubated at room temperature in a dark place for 2 h. At the end of the 2 h, the absorbance of samples was measured at 760 nm using a spectrophotometer (T80, PG Ins. UK.). Each analysis was carried out in duplicate. TPC was calculated by an equation obtained from a calibration curve consisting of different concentrations of stock solutions (25, 50, 75, 100, and 250 mg/L) with a high R² (0.9997). The results were expressed as mg/100g gallic acid equivalent (GAE) in DW.

The antioxidant capacity analysis was performed according to Thaipong *et al.* [43] with a slight modification. 150 µL of extracts and 2850 µL of DPPH methanolic solution, whose absorbance is 1.1 at 515 nm, were mixed, and the mixture was incubated at room temperature in a dark place for 60 min. Following 60 min, the absorbance of samples was measured at 515 nm. Each sample was analyzed in duplicate, and AC was calculated using an equation obtained from a calibration curve consisting of different concentrations of stock solutions (10, 20, 30, 40, and 50 mg/L) with the high R² (0.9988). Results were expressed as mmol Trolox equivalent (mmol TE)/100g in DW.

Determination of color parameters

The reflectance color value of the kiwifruit slice was measured using a Hunter Lab Color Miniscan XE (45/0-L, USA). The samples were placed on a white background, and the measurement was performed at

four different edge spots on the surface by covering a transparent glass. The measurements were repeated five times. ΔE indicates total color differences of the samples. High ΔE values represent the high color change compared to initial color values, meaning that the process causes high color loss in the samples. ΔE was calculated as follows [44]:

$$\Delta E = \sqrt{(L_0 - L)^2 + (a_0 - a)^2 + (b_0 - b)^2} \quad (12)$$

Statistical analysis

All statistical analysis was carried out using SPSS software (ver. 22 SPSS Inc., Chicago, IL, USA). One-way analysis of variance (ANOVA) and then Duncan post hoc test was used for comparing the means at the significance level $p < 0.05$.

RESULTS AND DISCUSSION

Influence of temperature on drying time

Fig. 1 shows the variation of *MR* and *DR* of kiwifruits depending on time. It is a fact that drying temperature plays a significant role in drying time. A higher evaporation rate was observed at higher temperatures. In this context, *DR* increased with the increment in drying temperature as expected, and consequently, drying time decreased. The times required to reduce 7% (*WB*) water content were 330 min, 240 min, and 210 min for 60 °C, 70 °C, and 80 °C, respectively. A falling rate period was observed for drying kiwifruits, not clearly constant rate as has been already observed [10,11,45].

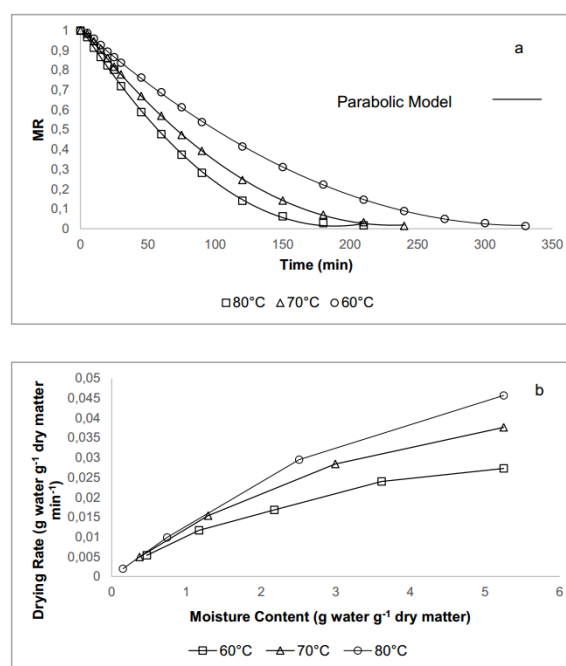


Figure 1. The variations of *MR* (a) and *DR* (b) of kiwifruits during the drying process at different temperature.

Mathematical modeling of convective drying curves

As shown in Fig. 1, the *MR* of kiwifruits at different temperatures fitted the mathematical models listed in Table 1. The statistical criteria were used to assess goodness to fit (Table 2). The R^2 -values of the selected mathematical models were higher than the acceptable value of 0.90, as reported by Demiray *et al.* [33]. The lowest *RMSE*- and χ^2 -values and the highest R^2 -values for the drying curves at 60 °C and 70 °C were obtained from the Parabolic model, while the Page model was found to be suitable for the drying curve at 80 °C. The experimental and predicted *MR*-values obtained from the parabolic and Page models are compared in Fig. 2.

Table 1. Mathematical models of thin-layer drying curves

Model name	Model	Ref.
Logaritmik	$a \exp(-kt) + c$	[33]
Lewis	$\exp(-kt)$	[33]
Henderson and Pabis	$a \exp(-kt)$	[33]
Page	$\exp(-kt^n)$	[33]
Parabolic	$a + bt + ct^2$	[35]
Wang and Sing	$1 + at + bt^2$	[58]

Activation energy and effective moisture diffusivity

The values of effective moisture diffusivity and activation energy of kiwifruits are shown in Table 3. The effective moisture diffusivity of kiwifruits ranged

Table 2. Model constants and statistical parameters of thin-layer drying curves

Model	Temperature, °C	Model Constants		χ^2	RMSE	R^2	
Lewis	60	k= 0.007714		0.002462495	0.04830	0.9828	
	70	k= 0.010610		0.002830165	0.05151	0.9799	
	80	k= 0.013110		0.002689296	0.05010	0.9809	
Page	60	k= 0.001964	n= 1.285	0.000250131	0.01496	0.9984	
	70	k= 0.002699	n= 1.310	0.000160754	0.01186	0.9990	
	80	k= 0.003701	n= 1.302	0.000186690	0.01272	0.9989	
Henderson and Pabis	60	k= 0.008316	a= 1.056	0.001765952	0.03975	0.9890	
	70	k= 0.011630	a= 1.066	0.001846903	0.04020	0.9886	
	80	k= 0.014300	a= 1.063	0.001922622	0.04082	0.9883	
Logaritmik	60	k= 0.008549	a= 1.044	c= 0.0136	0.002185487	0.04290	0.9872
	70	k= 0.011970	a= 1.054	c= 0.0147	0.002335352	0.04356	0.9886
	80	k= 0.014800	a= 1.049	c= 0.0173	0.002509920	0.04481	0.9858
Wang and Singh	60	a= -0.005866	b= 0.00008698		0.000083915	0.00867	0.9995
	70	a= -0.008218	b= 0.00001706		0.000262311	0.01515	0.9984
	80	a= -0.010220	b= 0.00002643		0.000292806	0.01593	0.9982
Parabolic	60	a= 1.013	b= -0.006050	c= 0.000009186	0.000027098	0.00478	0.9999
	70	a= 1.023	b= -0.008671	c= 0.000018710	0.000086925	0.00840	0.9995
	80	a= 1.018	b= -0.010630	c= 0.000028130	0.000202566	0.01273	0.9989

from 3.01×10^{-8} to 4.99×10^{-8} $\text{m}^2 \text{min}^{-1}$. The effective moisture diffusivity of kiwifruits dried at 80 °C was the highest compared to those at other temperatures. It can be claimed that the effective moisture diffusivity increased with the increase in the drying air temperature. Thus, the moisture content of the samples could be more easily evaporated, and accordingly, *DR* increased. The effective moisture diffusivity is directly proportional to *DR* [33]. In the current study, effective moisture diffusivity of kiwifruits at 60 °C was found as 4.23×10^{-8} $\text{m}^2 \text{min}^{-1}$. At the same time, Chin *et al.* [45] and Kaya *et al.* [10] have notified that effective moisture diffusivities of kiwifruits at 60 °C and 65 °C were 1.57×10^{-8} $\text{m}^2 \text{min}^{-1}$ and 5.81×10^{-10} $\text{m}^2 \text{s}^{-1}$. This difference could result from relative humidity, air velocity, and slice thickness.

The activation energy was calculated as a function of absolute temperature and given in Fig. 3. A slope obtained from the natural logarithm of effective moisture diffusivity versus T^{-1} was used to calculate activation energy. The activation energy was found to be 24.71 kJ mol^{-1} and 5.9 kcal mol^{-1} . Chin *et al.* [45] and Kaya *et al.* [10] have notified 37.70 kJ mol^{-1} and 27.707 kJ mol^{-1} activation energy for the 6 mm and 7 mm kiwifruit slices, respectively.

Effect of drying process on AAC, TPC, and AC

The effects of the temperature on AAC, TPC, and AC are shown in Table 4. The drying temperature con-

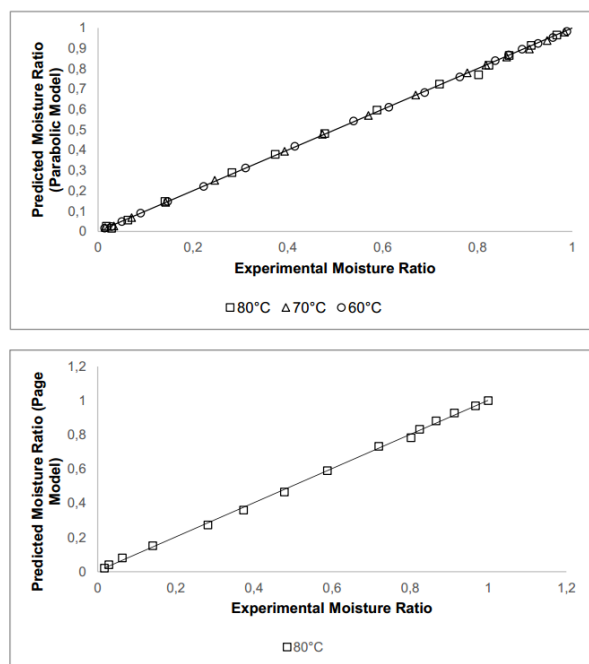


Figure 2. Comparison of the experimental and predicted MR values for the drying curves at 60 °C, 70 °C, and 80 °C (parabolic and Page model).

Table 3. Effective moisture diffusivity and activation energy of convective dried kiwifruits

Temperature °C	D_{eff} ($m^2 \text{ min}^{-1}$)	E_a (kJ mol^{-1})	E_a (kcal mol^{-1})
60	3.01×10^{-8}		
70	4.23×10^{-8}	24.71	5.9
80	4.99×10^{-8}		

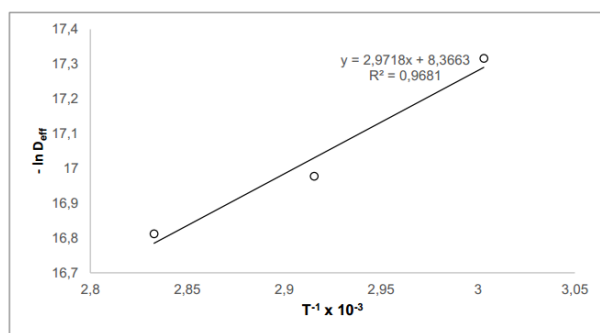


Figure 3. The Arrhenius-type relationship between the effective moisture diffusivity and absolute temperature.

siderably influenced the degradation of AAC and TPC. AAC and TPC were $462.81 \pm 11.53 \text{ mg } 100 \text{ g}^{-1}$ and $1846.87 \pm 15.52 \text{ mg GAE } 100 \text{ g}^{-1}$ in fresh kiwifruits. Correia *et al.* [5] reported higher values ($535 \text{ mg } 100 \text{ g}^{-1}$ AAC and $3376 \text{ mg } 100 \text{ g}^{-1}$ TPC). but on the contrary,

Leontowicz *et al.* [46] found a lower value of TPC ($5.41\text{--}5.47 \text{ mg GAE } 100 \text{ g}^{-1}$) than the present results. The highest AAC and TPC loss was 64.22% and 59.43% at 80 °C and 60 °C, respectively. AAC was highly affected by increasing drying temperature. This result was in good agreement with the previous reports [5,6,10,11,45,47,48]. The loss of AAC in kiwifruits was 57.27%, 59.90%, and 64.22% at 60 °C, 70 °C, and 80 °C, respectively. Correia *et al.* [5] have reported the loss AAC in kiwifruits of 76%, 79%, and 82% at the end of the drying process carried out at 60 °C, 70 °C, and 80 °C, respectively, which are larger than the loss found in the present study. Higher AAC degradation at higher temperatures can be associated with its thermo-sensitivity character and easy degradable structure. It was notified that higher temperatures cause an increase in the rate of ascorbic acid oxidation (non-enzymatic or enzymatic) [11, 49]. TPC was also reduced by drying. Similarly, Akar and Barutçu Mazi [32] indicated lower phenolic compounds in hot-air dried kiwifruits when compared to fresh samples. However, the loss of TPC decreased with increasing drying temperature. Likewise, López *et al.* [4] have notified a higher TPC at higher drying temperatures of blueberries, although the TPC decreased with drying temperature. Izli *et al.* [50] have reported similar results for kiwifruits. It could be explained by the formation of phenolic compounds at higher temperatures because of the availability of precursors of phenolic molecules by the non-enzymatic interconversion between phenolic molecules [47]. The loss of TPC in kiwifruits was 59.43%, 54.72%, and 53.61% at 60 °C, 70 °C, and 80 °C, respectively. Correia *et al.* [5] have reported a decrease of 80%, 88%, and 93% in the TPC at kiwifruits dried at 60 °C, 70 °C, and 80 °C, respectively. A mean difference was found between the AAC and TPC of fresh and dried kiwifruits ($p < 0.05$). The AC of fresh kiwifruits was $1.903 \pm 0.15 \text{ mmol TE } 100 \text{ g}^{-1}$ (DW). This value is lower than the value ($6160 \text{ } \mu\text{mol TE } 100 \text{ g}^{-1}$) notified by Correia *et al.* [5]. Drying temperature significantly affected the AC of kiwifruits ($p < 0.05$), and the highest AC loss was in the samples dried at 60 °C. The exposure of the compounds with antioxidant activity to high temperatures causes degradation and decrement in the AC. However, the temperature is not the only factor affecting the degradation of the antioxidative compounds. Drying time is also an important factor, and the longer time, the higher degradation [5]. Similar to TPC, the loss of AC decreased with the increment in drying temperature. Long drying time may decrease antioxidant capacity [51]. Similar findings were reported by Horuz *et al.* [44]. On the contrary, Correia *et al.* [5] have notified that AC loss increased based on the increment in drying temperature. Decreasing AC has been proportionally

associated with the loss of AAC of the TPC [52,53]. Additionally, the correlation coefficients (r) between AAC and AC were 0.964, 0.934, and 0.964 at 60 °C, 70 °C, and 80 °C, respectively, while correlation

coefficients between TPC-AC were calculated as 0.977, 0.958 and 0.974 at 60 °C, 70 °C, and 80 °C, respectively. According to these results, TPC contributed most to AC than AAC at each temperature.

Table 4. AAC, TPC and AC of fresh and dried kiwifruits

Temperature	Time	AAC	Loss Percentage	TPC	Loss Percentage	AC	Loss Percentage
°C	h	mg 100 g ⁻¹ DW	%	mg 100 g ⁻¹ DW	%	mmol TE 100 g ⁻¹ DW	%
60	0	462.81±11.53 ^a	0	1846.87±15.52 ^a	0	1.903±0.15 ^a	0
	5.5	197.74±11.58 ^b	57.27	747.66±16.09 ^b	59.43	0.283±0.15 ^b	85.13
70	0	462.81±11.53 ^a	0	1846.97±15.52 ^a	0	1.903±0.15 ^a	0
	4	185.59±10.40 ^{b,c}	59.90	837.35±17.01 ^c	54.72	0.480±0.01 ^c	74.78
80	0	462.81±11.53 ^a	0	1846.97±15.52 ^a	0	1.903±0.15 ^a	0
	3.5	165.59±12.58 ^c	64.22	857.47±16.50 ^c	53.61	0.475±0.005 ^c	75.03

*Different letters in the same column indicate significant differences with a confidence of 95%.

Color values of fresh and dried kiwifruit slices

The color values of fresh and dried kiwifruits are presented in Table 5. The L , a , and b values of fresh kiwifruits were 43.68±0.96, -3.73±0.06, and 16.64±0.45, respectively. The L value was significantly reduced by drying ($p<0.05$). The highest reduction in the L value was obtained from kiwifruits dried at 80 °C, meaning that the darkest dried kiwifruits were obtained at 80 °C. On the other hand, the a value remarkably increased during the drying, and the temperature greatly affected it ($p<0.05$). The b value of the fresh samples was higher than that of the dried kiwifruit slice samples ($p<0.05$). During drying, the redness of kiwifruits increased while the yellowness decreased. The degradation of some pigments, the oxidation of phenolic compounds, and the non-enzymatic browning directly affect the color of the dried fruit. Chlorophylls a and b are the major color pigments of kiwifruits [32]. The chemical structure of chlorophyll changes with heat treatment that causes magnesium replacement [54]. Accordingly, pheophytin and pheophorbide, darker pigments than chlorophylls, are derived [55]. A lower L value indicates higher darkness. Decrement in L values of the dried kiwifruits may be possibly explained by these alterations of chlorophyll's chemical structure because of the drying process and other factors affecting the color. Higher temperature leads to darker pigments formation, and thus, the L value of dried kiwifruits showed more decrement at higher temperatures. On the other hand, kiwifruits contain xanthophylls and β -carotene as chlorophylls [32]. Chlorophylls mask the yellow color of the carotenoids as the major color pigment and provide fresh green color [56]. Even though an increment in the b value is expected with removing the mask because of the

change in chlorophylls, the b value decreased. This can be associated with the possible carotenoid degradation in kiwifruits. Akar and Barutçu Mazi [32] reported that the degradation of chlorophylls affects the a value of the foods. As the retention of the chlorophylls increased, the a value of kiwifruits decreased [32]. In the present study, increment in the a value may be proved with this statement. Likewise, Doymaz [57] notified a decrease in the L and b values of the infrared dried kiwifruits at the end of drying, and the a value increased compared to fresh kiwifruits. Moreover, the highest ΔE value was observed at 80 °C, meaning that the highest color change of kiwifruits occurred.

Table 5. Color values of fresh and dried kiwifruits

	L	a	b	ΔE
Fresh	43.68±0.96 ^a	-3.73±0.06 ^a	16.64±0.45 ^a	0
60 °C	35.45±0.27 ^b	1.99±0.01 ^b	15.18±0.10 ^b	10.13
70 °C	34.17±0.12 ^b	2.02±0.03 ^b	14.66±0.08 ^b	11.29
80 °C	32.51±0.36 ^c	2.55±0.03 ^c	13.61±0.13 ^c	13.17

* Different letters in the same column indicate significant differences with a confidence of 95%.

CONCLUSION

Turkey's most common cultivated kiwifruits (*Actinidia delicosa* cv. Hayward) were investigated at different drying temperatures. The DR of kiwifruit slices was highly influenced by drying temperature. The longest drying time was 330 min at 60 °C, and the shortest was 210 min at 80 °C. The drying curves at 60 °C and 70 °C were suitably described with the Parabolic model, while the Page model gave a better fit for the drying curve at 80 °C. The effective moisture

diffusivity showed an increment with the increase in drying temperature. The highest effective moisture diffusivity was at 80 °C. The AAC, TPC, and AC were higher for fresh than dried kiwifruits. The highest reduction of AAC was observed at 80 °C because of the more rapid enzymatic and non-enzymatic degradation. On the contrary, the highest loss of TPC and AC occurred at 60 °C. The *L* and *b* values of kiwifruits decreased during the drying process, unlike the *a* value that increased. Higher temperature caused a higher color degradation. For preventing color degradation, lower drying temperatures should be preferred.

As a result, although higher temperatures provide a short drying time, a higher loss of AAC and color degradation were observed. In addition, relatively high retention of TPC and AC was determined at higher temperatures. In summary, while drying at 60 °C causes the highest loss of TPC and AC, the highest loss of AAC and color degradation drying at 80 °C. In light of these data, drying at 70 °C should be suggested for moderate nutritional loss and color degradation. On the other hand, hot-air drying was selected due to mostly being preferred for industrial production, easier to use, relatively cheaper. However, some promising methods should be evaluated. Therefore, kiwifruits should be dehydrated with other drying methods such as vacuum, microwave, combinations of vacuum-microwave, microwave-hot air in further studies as suggestions. Thus, the most suitable conditions and methods may be optimized by observing the loss of nutritional compounds and color properties during the process.

REFERENCES

- [1] L. Fu, B. T. Xu, X. R. Xu, R. Y. Gan, Y. Zhang, E. Q. Xia, H. B. Li, *Food Chem.* 129 (2) (2011) 345-350.
- [2] N. D. Mrad, N. Boudhrioua, N. Kechaou, F. Courtois, C. Bonazzi, *Food Bioprod. Process.* 90 (3) (2012) 433-441.
- [3] L. Méndez-Lagunas, J. Rodríguez-Ramírez, M. Cruz-Gracida, S. Sandoval-Torres, G. Barriada-Bernal, *Food Chem.* 230 (2017) 174-181.
- [4] J. López, E. Uribe, A. Vega-Gálvez, M. Miranda, J. Vergara, E. Gonzalez, K. Di Scala, *Food Bioprocess Technol.* 3 (5) (2010) 772-777.
- [5] P. Correia, R. P. Guiné, A. C. Correia, F. Gonçalves, M. Brito, J. Ribeiro, *Agric. Eng. Int.: CIGR Journal.* 19 (3) (2017) 203-212.
- [6] J. Wang, H-W. Xiao, J-H. Y, J. Wang, V. Raghavan, *Food Bioprocess Technol.* 12 (2019) 865-876.
- [7] Y. Shen, H. Xia, Z. Lei, D. Liang, *Advances in Engineering Research.* 63 (2018) 1819-1822.
- [8] AN. Kim, HJ. Kim, J. Chun, H.J. Heo, W.L. Kerr, SG. Choi, *LWT-Food Sci. Technol.* 89 (2018) 535-541.
- [9] J. Wang, S.K. Vanga, V. Raghavan, *LWT-Food Sci. Technol.* 107 (2019).
- [10] A. Kaya, O. Aydın, S. Kolaylı, *Food Bioprod. Process.* 88 (2-3) (2010) 165-173.
- [11] T. Orikasa, S. Koide, S. Okamoto, T. Imaizumi, Y. Muramatsu, J. I. Takeda, T. Shiina, A. Tagawa, *J. Food Eng.* 125 (2014) 51-58.
- [12] C. S. Gammon, R. Kruger, C. A. Conlon, P. R. von Hurst, B. Jones, W. Stonehouse, *Nutr., Metab. Cardiovasc. Dis.* 24 (1) (2014) 91-99.
- [13] N. Motohashi, Y. Shirataki, M. Kawase, S. Tani, H. Sakagami, K. Satoh, T. Kurihara, H. Nakashima, I. Musci, A. Varga, J. Molnár, *J. Ethnopharmacol.* 81 (3) (2002) 357-364.
- [14] W. H. Chang, J. F. Liu, *Int. J. Food Sci. Nutr.* 60 (8) (2009) 709-716.
- [15] Y. I. Mahmoud, *Biomed. Pharmacother.* 94 (2017) 206-218.
- [16] W. Kang, H. Yang, H. J. Hong, C. H. Han, Y. J. Lee, *Korean J. Vet. Res.* 52 (4) (2012) 270-280.
- [17] M. Maskan, *J. Food Eng.* 48 (2) (2001) 177-182.
- [18] R. Thuwapanichayanan, S. Prachayawarakorn, J. Kunwisawa, S. Soponronnarit, *LWT-Food Sci. Technol.* 44 (6) (2011) 1502-1510.
- [19] P. K. Wankhade, R. S. Sapkal, V. S. Sapkal, *Procedia Eng.* 51 (2013) 371-374.
- [20] R. L. Monteiro, B. A. Carciofi, J. B. Laurindo, *J. Food Eng.* 178 (2016) 1-11.
- [21] P. Fellows, *Food Processing Technology Principles and Practice*, second ed. Boca Raton, Florida (2000).
- [22] C. Ratti, *J. Food Eng.* 49(4) (2001) 311-319.
- [23] A. R. Celma, F. Cuadros, F. López-Rodríguez, *Food Bioprod. Process.* 90 (2) (2012) 224-234.
- [24] H. Darvishi, A. R. Asl, A. Asghari, M. Azadbakht, G. Najafi, J. Khodaei, *J. Saudi Soc. Agric. Sci.* 13 (2) (2014) 130-138.
- [25] H. Yoğurtçu, *Firat Üniv. Eng. Sci. J.* 26 (1) (2014) 27-33.
- [26] A. Fijalkowska, M. Nowacka, A. Wiktor, M. Sledz, D. Witrowa-Rajchert, *J. Food Process Eng.* 39 (3) (2016) 256-265.
- [27] C. Ricce, M. L. Rojas, A. C. Miano, R. Siche, P. E. D. Augusto, *Food Res. Int.* 89 (2016) 701-708.
- [28] X. D. Chen, A. S. Mujumdar, X. D. Chen, A. S. Mujumdar (Eds.) *Drying technologies in food processing*. Blackwell, Oxford (2008).
- [29] E. Seyedabadi, M. Khojastehpour, M.H Abbaspour-Fard, *Int. J. Food Prop.* 20 (2017) 36-49.
- [30] H. Jarahzadeh, S.T. Dinani, *Food Sci. Biotechnol.* 28 (2) (2019) 365-376.
- [31] Y. Kumar, V.S. Sharanagat, L. Singh, P.K. Nema, *J. Food Process. Preserv.* 44 (9) (2020) e14639.
- [32] G. Akar, I. Barutçu Mazi, *J. Food Process. Eng.* 42 (3) (2019) e13011.
- [33] E. Demiray, A. Seker, Y. Tulek, *Heat Mass Transf.* 535 (2017) 1817-1827.
- [34] M. Zarein, S. H. Samadi, B. Ghobadian, *J. Saudi Soc. Agric. Sci.* 141 (2015) 41-47.
- [35] J. Bi, A. Yang, X. Liu, X. Wu, Q. Chen, Q. Wang, X. Wang, *LWT-Food Sci. Technol.* 602 (2015) 1136-1142.

- [36] M. Śledź, M. Nowacka, A. Wiktor, D. Witrowa-Rajchert, *Food Bioprod. Process.* 91 (4), (2013) 421-428.
- [37] M. Zhang, J. Tang, A. S. Mujumdar, S. Wang, *Trends Food Sci. Technol.* 17 (10) (2006) 524-534.
- [38] A. O. Omolola, A. I. Jideani, P. F. Kapila, *Int. J. Agric. Biol. Eng.* 76 (2014) 107-113.
- [39] Crank, *Mathematics of Diffusion*, Clarendon Press, Oxford (1975).
- [40] A. Dönmez Drying Kinetics of Resveratrol and Water-Soluble Vitamins of Some Grape Varieties Grown in Denizli Region, MSc. Thesis, Pamukkale University, Institute of Science, Denizli, (2015) Turkey.
- [41] M. R. Otağ, Determination of Some Properties and Resveratrol Content of Some Grape Varieties Grown in Denizli Çal Region During Different Ripening Period and After Drying Process, PhD Thesis, Pamukkale University, Institute of Science, Denizli, (2015) Turkey.
- [42] V. L. Singleton, J. A. Rossi, *Am. J. Enol. Vitic.* 16 (3) (1965) 144-158.
- [43] K. Thaipong, U. Boonprakob, K. Crosby, L. Cisneros-Zevallos, D. H. Byrne, *J. Food Compos. Anal.* 19 (6-7) (2006) 669-675.
- [44] E. Horuz, H. Bozkurt, H. Karataş, M. Maskan, *Food Chem.* 230 (2017) 295-305.
- [45] S. K. Chin, E. S. Siew, W. L. Soon, *Int. Food Res. J.* 22 (6) (2015) 2188-2195.
- [46] H. Leontowicz, M. Leontowicz, P. Latocha, I. Jesion, Y. S. Park, E. Katrich, D. Barasch, A. Nemirovski, S. Gorinstein, *Food Chem.* 196 (2016) 281-291.
- [47] A. Vega-Gálvez, K. Di Scala, K. Rodríguez, R. Lemus-Mondaca, M. Miranda, J. López, M. Perez-Won, *Food Chem.* 117 (4) (2009) 647-653.
- [48] S. M. Oliveira, I. N. Ramos, T. R. Brandão, C. L. Silva, *J. Food Process. Preserv.* 39 (6) (2015) 2485-2496.
- [49] P. H. S. Santos, M. A. Silva, *Drying Technol.* 26 (12) (2008) 1421-1437.
- [50] N. Izli, G. Izli, O. Taskin, *J. Food Meas. Charact.* 11 (1) (2017) 64-74.
- [51] M. C. Garau, S. Simal, C. Rossello, A. Femenia, *Food Chem.* 104 (3) (2007) 1014-1024.
- [52] N. S. Kerkhofs, C. E. Lister, G. P. Savage, *Plant Foods Hum. Nutr.* 60 (3) (2005) 17-121.
- [53] R. K. Toor, G. P. Savage, *Food Chem.* 94 (1) (2006) 90-97.
- [54] V. Sant'Anna, P.D. Gurak, L.D.F. Marczak, I.C. Tessaro, *Dyes Pigm.* 98 (3) (2013) 601-608.
- [55] J. Wang, HW. Xiao, XM. Fang, A.S. Mujumdar, S.K. Vidyarthi, L. Xie, *Drying Technol.* (2020) 1-14.
- [56] T.K. McGhie, A.D. Ainge, *J. Agric. Food Chem.* 50 (2002) 117-121.
- [57] İ. Doymaz, *Int. J. Green Energy.* 15 (11) (2018) 622-628.
- [58] İ. Doymaz, *J. Food Process. Preserv.* 35 (2011) 280-289.

FADIME BEĞÜM TEPE¹
TOLGA KAĞAN TEPE¹
AYTEN EKİNCİ²

¹ Department of Food Technology, Şebinkarahisar Vocational School of Technical Science, Giresun University, Giresun, Turkey

² Department of Food Technology, Denizli Vocational School of Technical Science, Pamukkale University, Denizli, Turkey

NAUČNI RAD

UTICAJ TEMPERATURE VAZDUHA NA KARAKTERISTIKE SUŠENJA I NEKA BIOAKTIVNA SVOJSTVA KRIŠKI VOĆA KIVI

Istraživana je kinetika sušenja, sadržaj askorbinske kiseline (AAC), ukupni sadržaj fenola (TPC) i antioksidativni kapacitet (AC) plodova kivija na različitim temperaturama (60 °C, 70 °C i 80 °C). Brzina sušenja i efektivna difuzivnost vlage kivija bila je najveća na 80 °C. Parabolni model najbolje predviđa promenu sadržaja vlage na 60 °C i 70 °C, dok Pejdžov model bolje opisuje krivu sušenja na 80 °C. Sa druge strane, na AAC, TPC i AC kivija značajno je uticala temperatura. Degradacija AAC se povećavala sa povećanjem temperature, dok su TPC i AC bili viši na višoj temperaturi. Raspon AAC, TPC i AC svežeg i sušenog voća iznosio je 165,59±12,58-462,81±11,53 mg/100 g (računo na suhu masu), 747,66±16,09-1846,87±15,52 mg GAE/100 g i 0,283±0.15-1,903±0.15 mmol TE/100 g, redom. Najveći gubici AAC, TPC i AC iznose 64,22%, 59,43% i 85,13%, redom.

Ključne reči: askorbinska kiselina, antioksidativni kapacitet, kinetika sušenja, kivi.

PETAR D. JANJATOVIĆ ¹
OLIVERA A. ERIĆ CEKIĆ ^{2,3}
DRAGAN M. RAJNOVIĆ ¹
SEBASTIAN S. BALOŠ ¹
VENCISLAV K. GRABULOV ⁴
LEPOSAVA P. ŠIDJANIN ¹

¹ Department of Production
Engineering, Faculty of
Technical Science, University of
Novi Sad, Novi Sad, Serbia

² Innovation Center of Mechanical
Engineering Faculty, University of
Belgrade, Belgrade, Serbia

³ Faculty of Mechanical and Civil
Engineering, University of
Kragujevac, Kraljevo, Serbia

⁴ Institute for testing of
materials-IMS, Belgrade, Serbia

SCIENTIFIC PAPER

UDC 669.13:621.74:620

MICROSTRUCTURE AND FRACTURE MODE OF UNALLOYED DUAL-PHASE AUSTEMPERED DUCTILE IRON

Article Highlights

- Dual-phase ADI provides a range of properties due to free ferrite and ausferrite constituents
- With the increase in austenitization temperature, a higher amount of ausferrite is formed
- Specimens with the highest values of ausferrite have a dominant quasi-cleavage type of fracture
- Quasi-cleavage fracture around last-to-freeze zones is related to the presence of ausferrite
- Ausferrite influences the rise in strength and the drop in ductility

Abstract

Dual-phase ADI material microstructure consists of different amounts and morphologies of ausferrite and free ferrite, obtained by subjecting ductile iron to specific heat treatment. Its strength is lower compared to comparable ADI materials but exhibits a higher ductility, the major disadvantage of ADI. In the current study, an unalloyed ductile iron was intercritical austenitized in two-phase regions ($\alpha+\gamma$) at four temperatures from 840 to 780 °C for 2 h and austempered at 400 °C for 1 h to obtain dual-phase ADI with different percentages of free ferrite and ausferrite. Light and scanning electron microscopy was performed for the metallographic and fracture studies, respectively. Microscopy results were correlated to tensile testing results. The results indicated that, as the amount of ausferrite present in the matrix increases, higher values of strength and lower ductility are obtained. The fracture surfaces of dual-phase ADI microstructures with 22.8% of ausferrite in their matrix have regions of quasi-cleavage fracture around last-to-freeze zones, related to the presence of ausferrite in those areas. The specimens with the highest values of ausferrite of 86.8% among the dual-phase microstructure have a dominant quasi-cleavage type of fracture.

Keywords: dual matrix structure, austempered ductile iron, microstructure, surface of fracture.

Austempered ductile iron (ADI) is an isothermally modified ductile cast iron with a unique ausferritic microstructure consisting of ausferritic ferrite and carbon enriched retained austenite, and it is free of carbides. This microstructure, combined with spherical graphite, provides relatively high tensile properties, similar to heat-treated steels, with a lower density and

significantly lower fabricating costs. These properties make the ADI materials very attractive today, particularly for manufacturing parts in automotive, agricultural, railroad, mining, and other heavy industry sectors. Particular attention has been paid to tensile properties, wear, cavitation, and even ballistic properties of ADI materials [1-3]. In recent years, a new type of ductile cast iron material, called “dual-phase austempered ductile iron” (dual-phase ADI), has become an active field of research and development [4]. The microstructure of the dual-phase ADI matrix consists of different amounts and morphologies of ausferrite (common ADI microstructure) and free (proeutectoid or allotriomorphic) ferrite, which is obtained by subjecting ductile iron to specific heat treat-

Correspondence: O.A. Erić Cekić, Faculty of Mechanical and Civil Engineering, University of Kragujevac, Kraljevo, Serbia.
E-mail: olivera66eric@gmail.com
Paper received: 22 December, 2020.
Paper revised: 27 April, 2021.
Paper accepted: 23 July, 2021.

<https://doi.org/10.2298/CICEQ201222027J>

ments.

This dual-phase microstructure is obtained by intercritical annealing (partial austenitization) in the (α + γ +graphite) region, whereby colonies of free ferrite are introduced. Partial austenitization is finally followed by austempering in the conventional temperature range 250–400 °C up to several hours. As a result, depending on the temperature of austenitization, the matrix of the dual-phase ADI contains different amounts of free ferrite (FF) and ausferrite (AF). Compared to the conventional ductile irons, the ADI with dual-phase microstructure obtained has a higher ratio of strength to ductility [5]. The selections of different intercritical temperatures make it possible to get different combinations of free ferrite to ausferrite percentages.

Mechanical properties of the dual-phase ADI depend on the volume amount of free ferrite and the amount and morphology of ausferrite, which, in turn, is a function of the intercritical austenitizing temperature selected and an austempering treatment, as aforesaid [6-9]. Additionally, the dual-phase ADI could provide a wide range of mechanical properties as a function of the relative proportion of free ferrite and ausferrite microconstituents, thereby replacing standard ductile iron and austempered ductile iron in different applications [10]. Aranzabal *et al.* [11] studied the new mixed (ferritic-ausferritic) ductile iron for automotive suspension parts. It was found that the yield stress and tensile strength values of dual-phase ADI, together with its hardness, are similar to those of fully pearlitic ductile irons. In contrast, ductility remains at the same level as in ferritic ductile irons.

Recently, it has been shown by Wade and Ueda [12] and Verdu *et al.* [13] that the mechanical properties (yield stress, tensile strength, and hardness) of dual-phase ADI austempered at 375 °C increases as the ausferrite volume fraction in the microstructure of free ferrite and graphite nodules increase. Works carried out by Kilicli and Erdogan [9,10] were focused on the dual-phase ADI mechanical properties, particularly for those austempered at 365 °C and a wide variety of ferrite-ausferrite combinations. An interesting result was for the 45% ausferrite and 65% ferrite microstructure that yielded the most convenient strength-toughness ratio.

The fracture surfaces of the dual-phase ADI with different amounts of ferrite-ausferrite were also evaluated by several authors [14,15]. Nevertheless, there is no complete understanding of the sequence and occurrence of damage mechanisms, the influence of the morphology and ausferrite volume fraction on crack propagation, and damage evolution. In most

publications [15-20], the study of the fracture surface, obtained by tensile tests of ADI with dual matrix structure with different amounts of ferrite-ausferrite, has been relatively brief. In general, studies of the dual-phase ADI have focused on studying the role of different microconstituents during fatigue and tensile testing using in-situ analysis [19-22]. In the literature, very little information is currently available about the influence of the different amounts of the free ferrite and the ausferrite volume fractions and their distribution on the morphology of the fracture surfaces of dual-phase ADI [5-9].

This study aims to evaluate the fracture surfaces obtained using tensile tests from different samples of dual-phase ADI. The main objective of this work is to study the tensile fracture behavior of dual-phase ADI and ductile cast iron with a microstructure consisting of spherical graphite in a predominantly ferrite matrix with 10% pearlite and correlate the observed fracture mode and the tensile properties obtained.

MATERIALS AND METHODS

Materials

The material used in this study was industrially produced ductile iron keel blocks obtained in a commercial electro-induction foundry furnace. The melt was poured from about 1420 °C into a standard 25.4 mm Y block sand mold (ASTM A-395), ensuring sound castings. The chemical composition was determined on white cast samples using optical emission spectroscopy on ARL-2460. Tensile specimens with 6 mm diameter and 30 mm gauge length were machined from Y blocks.

The methodology employed to establish the heat treatment used to obtain "dual-phase" austempered ductile iron microstructures was determined according to the procedure described in previous papers by the authors [7-8]. An austempering temperature of 400 °C was selected to obtain a higher ductility of the ausferrite and thus higher ductility of dual-phase austempered ductile iron [2-6].

Heat treatment (HTA) of tensile specimens consisted of austenitization within the intercritical interval at 780, 800, 820, and 840 °C for 2 h, followed by austempering at 400 °C for 1 h in all cases. The obtained samples have been designated HTA-1, HTA-2, HTA-3, and HTA-4.

Methods

Metallurgical evaluation

Standard metallographic preparation techniques

(mechanical grinding and polishing, followed by etching in Nital) were applied before light microscopy (LM) examinations on an Orthoplan microscope (Leitz, Germany). The relationship between the amount (% in volume) of free ferrite (FF), ausferrite (AF), and graphite (Gr) in dual-phase ADI microstructures was quantified by image analysis software JMicroVision. The reported values average at least five analyzed fields of view on each sample.

Hardness measurement

The Vickers hardness HV10 (ISO 6507) was determined with a test load of 98.07 N (10 kg) and a dwell time of 15 s. The testing machine was an HPO 250 (WPM, Germany).

Tensile test

The specimens' tensile tests were performed on a WPM ZDM 5/91 (WPM, Germany) tensile testing machine equipped with an S-type measuring tension force sensor and linear variable differential transformer LVDT inductive sensor (HBM Germany). A Spider 8 (HBM, Germany) acquisition device connected the sensors to a PC. The tensile tests were done according to ISO 6892. The 0.2% proof stress (PS), the ultimate tensile stress (UTS), and elongation at failure (A) were measured.

The fractured surfaces of tensile-tested specimens were examined by a scanning electron microscope JEOL JSM 6460LV (JEOL, Japan) operated at 25 kV.

RESULTS AND DISCUSSION

Chemical composition and microstructures

The chemical composition of the as-cast ductile iron melt is shown in Table 1.

Table 1. The chemical composition of as-cast ductile iron

C	Si	Mn	Ni	Cr	Mg	P	S	Fe
3.5	2.5	0.35	0.05	0.06	0.031	0.018	0.015	balance

The microstructure of samples in as cast condition reflected that the original matrix was over 90% ferritic, with a nodularity of over 90%, an average nodule size of 20 μm , and an average nodule distribution of about 150 per mm^2 , according to the ASTM A247 standard. Figure 1 illustrates the overall microstructure appearance obtained for all specimens austenitized at different temperatures within the intercritical interval (austenitizing temperatures employed were 780 °C, 800 °C, 820 °C, and 840 °C) and austempered in the salt bath at 400 °C during 1 h. The different intercritical austenitization temperatures

allowed the microstructure to attain various amounts of ausferrite (AF) and free ferrite (FF). As shown in Figure 1, the amount of FF and AF directly depends on the austenitizing temperature. At lower austenitization temperatures (Figure 1a), there is a lower percentage of the AF, which is increased as the austenitization temperature increases (Figure 1d), and vice versa in the case of the FF. The relative amount of free ferrite (FF) decreases with the increase of austenitization temperature from 65.2 to 2%, while the amount of ausferrite (AF) increases from 22.8 to 86.8% (see Table 2). The dual-phase ADI microstructure achieved after austenitizing closer to the upper critical temperature (Figure 1d) consists almost entirely of ausferrite.

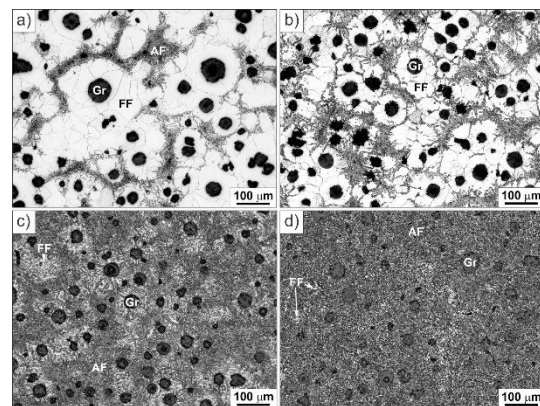


Figure 1. The amount of phases in samples austenitized at different austenitization temperatures T_v : a) $T_v = 780$ °C; 65.2%FF+22.8%AF+12%Gr, b) $T_v = 800$ °C; 42.8%FF+42.4%AF+14.8%Gr, c) $T_v = 820$ °C; 8%FF+80%AF+12%Gr, d) $T_v = 840$ °C; 2%FF+86.8%AF+11.2%Gr; FF (free ferrite), AF (ausferrite), Gr (graphite nodule).

Observation under higher magnification reveals different morphologies of microstructures present in the dual-phase ADI samples, Figure 2. The phases are easily distinguishable, as the free ferrite (FF) has a flat white surface, and retained austenite (RA) is more oblique with a more pronounced boundary (bevel edge). Also, RA has a more grayish appearance compared to FF. The ausferritic ferrite (AAF) plates in retained austenite (RA) could be recognized by gray to dark shade tinting.

The size of ausferritic ferrite plates changes with austenitization temperature, primarily due to the amount and size of prior austenite grains produced at different austenitization temperatures. At lower austenitization temperatures (780 °C), the prior-austenite grains are smaller, confined by the larger amount of free ferrite. Thus, the formed ausferrite ferrite plates during subsequent austempering are shorter and more randomly oriented (Figure 2a). With the increase of austenitization temperature (800 and 820 °C), the amount of ausferrite increases due to the formation of

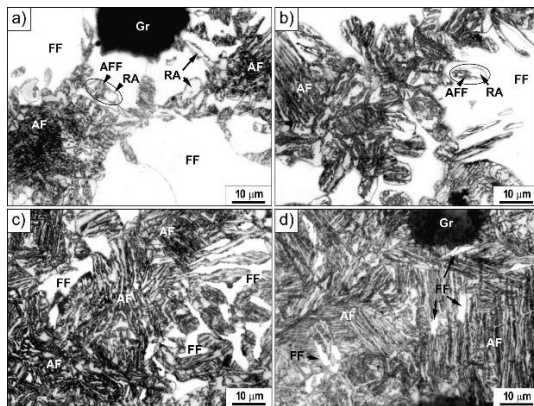


Figure 2. Microstructure of samples austenitised at different austenitisation temperatures T_γ : a) $T_\gamma = 780$ °C; b) $T_\gamma = 800$ °C; c) $T_\gamma = 820$ °C d) $T_\gamma = 840$ °C; FF (free ferrite), AF (ausferrite), Gr (graphite nodule), RA (retained austenite), AFF (ausferritic ferrite).

a higher amount of austenite of larger grain size (Figure 2b and c). In this case, ausferritic ferrite plates grow more easily, resulting in more elongated AFF plates and thus a more acicular appearance of ausferrite (AF). At austenitization temperatures of 840 °C, the microstructure is dominantly austenitic, which upon quenching to austempering temperature, freely can transform to ausferrite (Figure 2d). Produced ausferrite has long ausferritic ferrite plates, similar to acicular microstructure, which might be observed in conventional ADI material.

The width of ausferritic ferrite plates does not change significantly with increasing austenitization temperature. Although, more different sizes (larger spread) could be noticed at lower temperatures due to smaller prior-austenite grain size and faster austempering transformation.

Mechanical properties

The results of mechanical properties, depending on the amount of microconstituents in the samples used in this study, are given in Table 2.

It can be seen that the amount of ausferrite increases in dual-phase- ADI, ultimate tensile strength (UTS), proof strength (PS), and hardness (HV10) increases also. An increase in the amount of ausferrite in the matrix promotes higher values of the UTS and PS up to a peak value of 917 MPa and 720 MPa, respectively. This corresponds to the sample composed of 80% ausferrite and 8% free ferrite. The value of elongation (A) has an opposite trend. The lowest elongation values are correlated with the maximum values of ausferrite.

Fracture mode

The fracture surfaces of tensile test specimens were analyzed by SEM. The failure regions in the as-cast, mostly ferritic specimen, exhibit a uniform distribution of graphite nodules (Figure 3). Furthermore, there is a high degree of deformation around the graphite nodules. In addition, the ferritic space between nodules undergoes a substantial plastic deformation exhibiting dimples (Figure 3b). The fracture surface contains a relatively larger cavity size than the graphite nodule size (Figure 3b). Formation of the cavity may be attributed to decohesion at the graphite and surrounding ferrite matrix. The dimple pattern around the graphite nodules shows the deformation of the surrounding ferrite matrix during the final period of straining up to fracture. Voids characterize a typical fracture mode of ductile iron in its microstructure and a result of nodular cavities and possible the last-to-freeze (LTF) zones generated during solidification [23,24]. The appearance of last-to-freeze (LTF) regions are deliberated weak areas within the metallic matrix, and typical casting defects such as inclusions, porosity, and microshrinkage are present in these regions [23,24].

The SEM micro-fractographs of the dual-phase ADI samples, containing 22.8%, 42.4%, 80%, and 86.8% of ausferrite in the microstructure, are shown in Figure 4. The appearance of the dimpled fracture zone

Table 2. The mechanical properties and microconstituents percentages of as-cast ductile cast iron and dual-phase ADI alloys

Material	Proof strength	Ultimate tensile strength	Elongation	Ausferrite	Free Ferrite	Hardness
	PS [MPa]	UTS [MPa]	A [%]	vol. fraction	vol. fraction	HV10
As-cast ductile iron	318	456	19.1	/	/	150
HTA-1:(780 °C-2h/400 °C-1h)	340	478	16.0	22.8	65.2	164
HTA-2:(800 °C-2h/400 °C-1h)	395	557	12.8	42.4	42.8	202
HTA-3:(820 °C-2h/400 °C-1h)	620	825	11.7	80.0	8.0	296
HTA-4:(840 °C-2h/400 °C-1h)	709	915	11.0	86.8	2.0	292

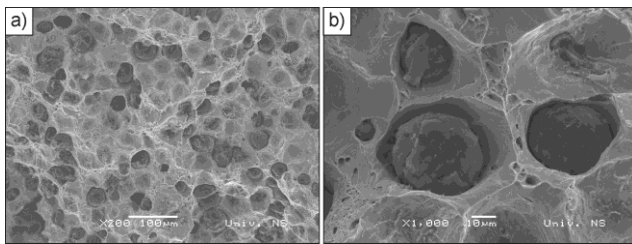


Figure 3. SEM fracture surface of as-cast ductile iron after failure in tension test: a) dimpled fracture surface, b) graphite nodules that undergone decohesion from the metal matrix.

in all specimens reveals a ductile (DF), quasi-cleavage (QCF), and brittle fracture (BF). A somewhat higher number of dimples with a cleavage facet was observed in the specimen with 42.4% ausferrite, Figure 4b. Ferrite volume fraction or ausferrite may play an essential role in determining fracture mode since ferrite fails in a more ductile mode and its contribution to the fracture resistance increases with increasing ferrite volume fraction. The quasi-cleavage pattern of fracture of the specimen with a higher ausferrite or low ferrite volume fraction, the majority of the fracture surface shows a quasi-cleavage pattern of fracture, reflecting the low ductility and fracture energy of this material. These findings are in agreement with the previously published results [14,15,18].

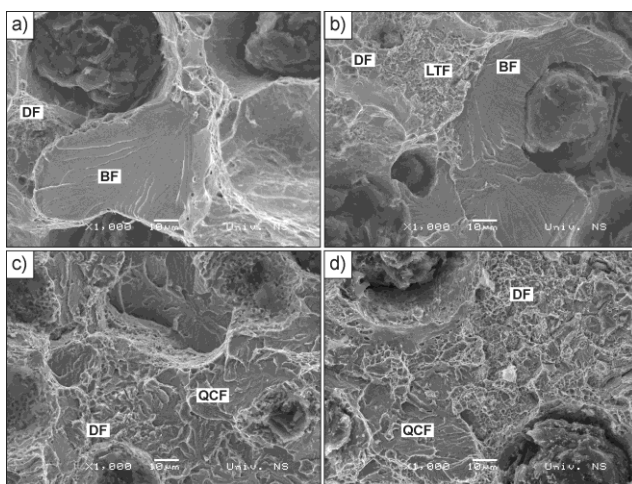


Figure 4. The fracture surfaces for specimens austenitised at: a) $T_r = 780\text{ }^\circ\text{C}$ (22.8% AF), b) $T_r = 800\text{ }^\circ\text{C}$ (42.4% AF), c) $T_r = 820\text{ }^\circ\text{C}$ (80% AF), d) $T_r = 840\text{ }^\circ\text{C}$ (86.8% AF); DF (ductile fracture), BF (brittle fracture), QCF (quasi-cleavage fracture), LTF (last to freeze zone).

In Figure 4c, the fracture surface of the specimen containing 80% ausferrite in the matrix is shown. A higher amount of ausferrite in the matrix produced a flat fracture surface, closely related to quasi-cleavage fracture mechanics [15,25,26].

The micrographs of specimens with highest values of ausferrite of 86.8% among the dual-phase

structure, the dominant form of the fracture surface was a quasi-cleavage type, Figure 4d.

The increased amount of ausferrite in the matrix (as shown in Figures 4a-d) increases the tendency to exhibit quasi-cleavage fracture. It is important to note the increase of ausferrite volume fraction in the matrix produced a reduced brittle fracture zone while that of the ductile fracture pattern and quasi-cleavage increased. The brittle fracture is observed in the specimens with 22.8% ausferrite (Figure 4a) near the graphite nodules. In comparison, the fully quasi-cleavage fracture is present for the high amounts of ausferrite in the specimen (HTA-4) with 86.8% of ausferrite (Figure 4d).

It is well documented [14,15] that in the dual-phase microstructure, the high strength ausferrite may restrict the deformation of low strength ferrite under tensile loading. The ductility decreases with increasing continuity of the ausferrite structure along eutectic cell boundaries. This may be explained considering that the high strength ausferrite may restrict the deformation of low strength ferrite under tensile loading at the moment of fracture. In this case, the low-strength ferrite in the rest of the matrix will be plastically deformed until the moment when the ausferrite breaks. It is reasonable to accept that at that moment, the higher strength of the ausferrite suffered by the ausferrite is suddenly transferred on the matrix of free ferrite, and a rapid fracture with a brittle appearance occurs.

As expected, the fracture in the case of a larger amount of free ferrite has a more brittle appearance (although the fracture strength is lower, and the ductility of the whole sample is higher). In comparison, we have standardly observed ductile and quasi-cleavage fracture in the case of a larger amount of ausferrite.

CONCLUSION

Based on test results and their analysis, the following conclusions can be summarized as:

The fracture mode of the specimen having predominantly ferritic matrix is ductile as characterized by microvoid coalescence and dimple rupture phenomena. The change of fracture mechanism could be correlated to a change in elongation and the relative proportion of free ferrite and ausferrite constituents in dual-phase ADI microstructure. The fracture surfaces of dual-phase ADI microstructures with 22.8% of ausferrite in their matrix have regions of quasi-cleavage fracture around last-to-freeze zones, related to the presence of ausferrite in those areas. The decrease in nodular cavities deformation and a higher amount of quasi-cleavage zones is a consequence of the increase

of volume fractions of ausferrite in dual-phase ADI microstructure. The specimens with the highest values of ausferrite of 86.8% among the dual-phase microstructure have a dominant quasi-cleavage type of fracture. Ausferrite represents a crucial phase in the metal matrix that influences the rise in strength and the drop in ductility. It can be regarded as one of the decisive influencing factors on the applicability of ADI, including dual-phase ADI.

Acknowledgment

This paper has been supported by the Ministry of Education, Science and Technological Development of the Republic of Serbia through project no. 451-03-68/2020-14/200156: “Innovative scientific and artistic research from the Faculty of Technical Sciences, Novi Sad, Serbia, activity domain” and project no. 451-03-68/2020-14/200213, Innovation Centre of Mechanical Engineering Faculty, University of Belgrade, Belgrade, Serbia.

The support has also been received from the Materials testing laboratory, Department of Production Engineering, Faculty of Technical Sciences Novi Sad Serbia, within the framework of the project entitled “Innovative materials and joining technologies.”

REFERENCES

- [1] W. Bingxu, Q. Feng, C. Gary, Barber, P. Yuming, C. Weiwei, W. Rui, *J. Mater. Res. Technol.* 9 (5) (2020) 9838-9855.
- [2] P. Janjatovic, O. Eric Cekic, L. Sidjanin, S. Balos, M. Dramicanin, J. Grbovic Novakovic, D. Rajnovic, *Met.* 11 (2021) 1-16.
- [3] S. Balos, I. Radisavljevic, D. Rajnovic, P. Janjatovic, M. Dramicanin, O. Eric- Cekic, L. Sidjanin, *Def. Sci. J.* 69 (2019), 571-576.
- [4] A. Basso, J. Sikora, *Int. J. Metalcast.* 6 (2012) 1-14.
- [5] R. Steiner, in *ASM Handbook Vol. 1*, by ASTM International, Ohio, USA, 33 (1990), p. 1005.
- [6] C. Verdu, J. Adrien, A. Reynaud, *Int. J. Cast Met. Res.* 18 (2005) 346-354.
- [7] A. Basso, R. Martinez, J. Sikora, *Mater. Sci. Technol.* 23 (2007) 1321-1326.
- [8] A. Basso, R. Martinez, J. Sikora, *Mater. Sci. Technol.* 25 (2008) 1271-1278.
- [9] V. Kilicli, M. Erdogan, *Mater. Sci. Technol.* 22 (2006) 919-928.
- [10] V. Kilicli, M. Erdogan, *Int. J. Cast. Met.* 20 (2007) 202-214.
- [11] J. Aranzabal, G. Serramoglia, D. Rousiere, *Int. J. Cast Met. Res.* 16 (2002) 185-190.
- [12] N. Wade, Y. Ueda, *Trans. ISII*, 21 (1981) 117-126.
- [13] C. Verdu, J. Adrien, A. Reynaud, *Int. J. Cast. Met. Res.* 18 (2005) 346-354.
- [14] A. Basso, J. Sikora, R. Martínez, *Fatigue Fract. Eng. Mater. Struct.* 36 (7) (2013) 650-659.
- [15] V. Kilicli, M. Erdogan, *J. Mater. Eng. Perform.* 19 (2010) 142-149.
- [16] F. Iacoviello, V. Di Cocco, M. Cavallini, *Fatigue Fract. Eng. Mater. Struct.* 39 (2016) 999-1011.
- [17] F. Iacoviello, V. Di Cocco, A. Rossi, M. Cavallini, *Fratt. Integrita Strutt.* 7 (25) (2013) 102-108.
- [18] L. D'Agostino, V. Di Cocco, O. Fernandez, D. F. Iacoviello, *Process. Struct. Integr.* 3 (2017) 201-207.
- [19] D.O. Fernandez, R.E Boeri, *Fatigue Fract. Eng. Mater. Struct.* 42 (2019) 2220-2231.
- [20] R.C. Voigt, L.M. Elderly, H.S. Chiou, *AFS Trans.* 94 (1986) 645-656.
- [21] T. Kobayashi, S. Yamada, *Metall. Mat. Trans. A* 27 (1996) 1961-1971.
- [22] A. Basso, M. Caldera, M. Chapetti, J. Sikora, *ISIJ, Int.* 50 (2010) 302-306.
- [23] R. Voigt, L. Eldoky, *AFS Trans.* 94 (1986) 645-656.
- [24] R. Martínez, R. Boeri, J. Sikora, *Jornadas SAM Asociación Argentina de Materiales - IV Latin-American Colloquium on Fracture and Fatigue, Neuquen, Argentina (2000) p.615.*
- [25] L. Masud, R. Martinez, S. Simison, R. Boeri, *J. Mater. Sci.* 38 (2003) 2971-2977.
- [26] R. Martinez, *Eng. Fract. Mech.* 77 (2010) 2749-2762.

PETAR D. JANJATOVIĆ ¹
OLIVERA A. ERIĆ CEKIĆ ^{2,3}
DRAGAN M. RAJNOVIĆ ¹
SEBASTIAN S. BALOŠ ¹
VENCISLAV K. GRABULOV ⁴
LEPOSAVA P. ŠIDJANIN ¹

¹ Departman za proizvodno
mašinstvo, Fakultet tehničkih
nauka, Univerzitet u Novom
Sadu, Novi Sad, Srbija

² Inovacioni centar mašinskog
fakulteta u Beogradu, Univerzitet
u Beogradu, Beograd, Srbija

³ Fakultet za mašinstvo i
građevinarstvo u Kraljevu,
Univerzitet u Kragujevcu,
Kraljevo, Srbija

⁴ Institut za ispitivanje
materijala IMS, Beograd, Srbija

MIKROSTRUKTURA I MORFOLOGIJA LOMA NELEGIRANOG DVOFAZNOG AUSTEMPEROVANOG NODULARNOG LIVA

Mikrostruktura dvofaznog austemperovanog nodularnog liva proizvedena je specifičnom termičkom obradom nodularnog liva i sastoji se od različitih količina i morfologije ausferita i slobodnog ferita. Zahvaljujući takvoj mikrostrukturi dvofazni austemperovani nodularni liv ima nižu vrednost čvrstoće u poređenju sa konvencionalnim ADI materijalima, ali veću duktilnost. U ovoj studiji, nelegirani nodularni liv je bio austenitizovan u međukritičnom dvofaznom području ($\alpha+\gamma$) na četiri temperature od 780 do 840 °C tokom 2 sata i zatim austemperovan na 400 °C tokom 1 sata da bi se dobio dvofazni ADI sa različitim procentima slobodnog ferita i ausferita. Metalografska analiza i analiza morfologije loma izvršena su pomoću svetlosnog i skenirajućeg elektronskog mikroskopa, respektivno. Rezultati mikroskopije su upoređeni sa rezultatima ispitivanja zatezanjem. Rezultati ukazuju da se sa povećanjem količine ausferita prisutnog u osnovi postižu veće vrednosti čvrstoće, ali i manja duktilnost. Površina loma dvofaznih ADI materijala sa 22,8% ausferita u osnovi sastoji se iz područja loma nastalog mehanizmom kvazi-cepanja oko zona koje su poslednje očvrsle, što se može povezati sa prisustvom ausferita u tim oblastima. Uzorci sa najvećom vrednošću ausferita od 86,8% u dvofaznoj mikrostrukturi imaju dominantan lom nastao mehanizmom kvazi-cepanja.

Ključne reči: dvofazna struktura, austemperovani nodularni liv, mikrostruktura, prelom.

NAUČNI RAD